University of Stavanger

Faculty of Science and Technology

MASTER'S THESIS

Study program/Specialization: MSc Petroleum Geosciences Engineering	Spring semester 2019 Open
Author: Lamine-Yanis Saadallah	*Yanis Saadallah*
Faculty supervisor: Dr. Arild Buland	
Title of thesis: Joint Bayesian AVO and RMO inversion.	
Credits (ECTS): 30	
Keywords: Amplitude variation with offset Residual move-out Inversion Bayes theorem Numerical methods	Pages: 105 Stavanger, June 15, 2019

Joint Bayesian AVO and RMO inversion

By

Lamine-Yanis Saadallah

MSc Thesis

Presented to the Faculty of Science and Technology

University of Stavanger

2019

Acknowledgements

Abstract

Seismic amplitude variation with offset (AVO) has proved to be a useful technique in oil exploration. However, the sensitivity of AVO to residual move-out (RMO) is considered a severe limitation. Small misalignments between corresponding reflections have a severe impact on the gradient, which may cause the user to acquire the wrong conclusion. To make AVO analysis more robust, Semblance, Cross correlation and Swans residual velocity indicator (RVI) have earlier been proposed as methods to correct for RMO. These existing methods are reviewed. In addition, a new joint Bayesian AVO and RMO inversion is developed to find the RMO and elastic parameters. The methods are all tested on one seismic section where the intercept and gradient follow a co-linear relationship, and another one containing an AVO class 2p anomaly deviating from a co-linear relationship between the intercept and gradient.

Semblance has traditionally been used during processing of the data and calculates the normalized stacking amplitude along different trajectories. However, the method lacks the sensitivity needed to properly condition the data for AVO and mishandles the anomaly. Cross correlation is a simple technique to quantify the similarity between the near and far traces relative to each other in time, but is distorted by heavy noise and the differences between the traces due to the anomaly. Swans RVI provides the necessary sensitivity to the small velocity errors Semblance lacks, but is heavily reliant on a co-linear relationship between the intercept and gradient. The newly developed joint Bayesian AVO and RMO inversion provides the necessary sensitivity, in addition to handling the AVO anomaly properly.

Contents

Chapter 1

Introduction

Seismic amplitude variation with offset (AVO) examines the reflection coefficient as a function of incident angle. The uses of AVO since its introduction are widely spread. Ostrander (1984) and Fatti et al. (1994) showed the AVO responses usefulness in predicting and mapping hydrocarbons. Avseth et al. (2000) used it to distinguish lithology and map porosity in clastics, while Landrø (2001) derived formulas to calculate approximate pressure and saturation related changes from time-lapse seismic data. However, most AVO techniques require a certain set of assumptions met. Attenuation and geometrical spreading must be properly accounted for, in order for the amplitudes to represent the reflection coefficients. In addition, pre-stack migration must relocate the scaled amplitudes to their correct position. Spratt (1987) showed that small errors in the normal move-out has a severe impact on the gradient and Spagnolini (1994) discussed the sensitivity of the relationship between velocity and AVO. In other words, AVO requires thorough processing and preconditioning of the data to be useful.

Ever since it was established that even the smallest velocity-errors has a great impact on the AVO response, several methods have been proposed to correct for it. Neidell & Taner (1971) introduced Semblance and Cross correlation, two measures of coherence. Swan (2001) derived an explicit expression directly linking velocity-error to the harm it causes AVO for brine-filled sediments. Later these methods have been widely used to ensure proper alignment of corresponding reflections in order to increase the reliability of AVO.

This thesis will review these methods, and their respective strengths and weaknesses in correcting seismic with and without AVO anomalies. As the errors in the normal move-out correction are directly linked to velocity, RMO has often been linked to errors in the velocity model. Semblance and the method introduced in Swan (2001) are both directly linked to velocity. In addition, the user is recommended to avoid known AVO anomalies in the data. In this study the source of the RMO is neglected, as the purpose is not to improve the velocity model, only the AVO response. In addition, a new joint Bayesian AVO and RMO inversion is developed to also handle

anomalies, and compared to the others. All the methods implemented in this study follow a static approach, meaning the entire trace is moved either up or down in time to ensure proper alignment.

Throughout this work it is assumed all processing artifacts are properly removed, except residual move-out (RMO).

Chapter 2

Theory

AVO analysis and inversion requires thorough pre-conditioning of the data to be useful, and most of it is performed during the processing of the data. Some main elements in processing include multiple removal, correction for attenuation and geometrical spreading, and pre-stack migration. The mentioned operations, and more, are all important but they come with uncertainty and complications. Additional post-processing conditioning is often required prior to seismic analysis. We assume proper scaling of amplitudes, multiple removal, and correction for noise attenuation and geometrical spreading is done prior. The only uncertainty considered in this thesis will be the reflection position, specifically due to RMO.

2.1   Processing

Seismic processing has in recent years greatly improved, and several complicated methods have been developed to increase the quality of the seismic image for exploration purposes. This section will focus on the two main operations directly linked to RMO.

2.1.1   Travel time curve

Figure 2.1 shows a simple example of a isotropic homogenous one-layer model. The goal is to calculate the travel time along the path SAR. Using Pythagoras theorem we can derive the equation for hyperbolic travel-time curves, given by:

$$t^2(x) = t_0^2 + \frac{x^2}{v^2}, \tag{2.1}$$

where x is the offset, v is the velocity and t_0 is the zero-offset two-way travel time. As the earth consists of several layers, the different velocities within these layers must
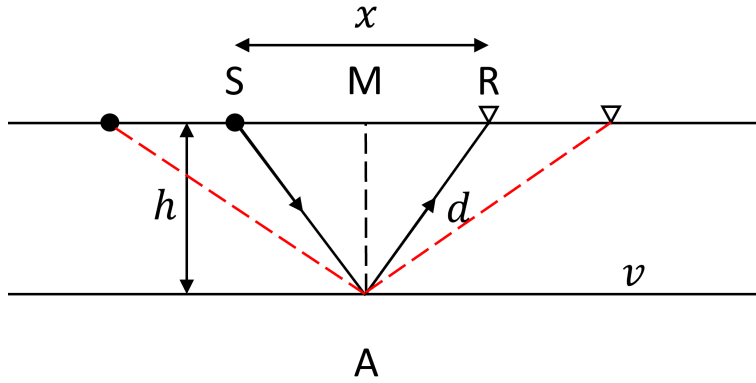
Figure 2.1: *Visualization of ray path for one horizontal layer. A and M are the common midpoints. S and R represent the source and receiver positions. h is the layer thickness, v is the layer-velocity, x is the offset and d is the ray path after reflecting off A.*

be taken into account. To do so, the root-mean-square (RMS) velocity is used. The RMS-velociy considers the time spent in each layer to calculate an average velocity,

$$v_{rms}^2 = \frac{1}{t_0} \sum_{i=1}^{N} v_i^2 \Delta \tau_i, \tag{2.2}$$

where v_i is the velocity in layer i, $\Delta \tau_i$ is the time spent in layer i and t_0 is the two way travel-time given by:

$$t_0 = \sum_{i=1}^{N} \Delta \tau_i. \tag{2.3}$$

By incorporating the RMS-velocity into equation 2.1, we obtain the expression for hyperbolic travel-time curves which is denoted:

$$t^2(x) = t_0^2 + \frac{x^2}{v_{rms}^2}. \tag{2.4}$$

Figure 2.1 is also showing a common depth point, A. If we add sources and receivers on each side, some primary reflections will have different incident angles but will reflect of the same point. A common-midpoint-gather (or CMP gather) is compromised of several traces with different incident angle, but with common depth points. CMP gathers are the primary data needed for AVO analysis.

2.1.2   Normal move-out correction

Figure 2.2 depicts a typical travel-time curve for a CMP-gather. Even though the reflection-point is fixed in space, the increasing incidence angle increases the length of the ray path. As a direct result, the travel-time increases, and the curve drifts away from the true geological position. The time-difference between the true geological position and the travel-time curve is defined as normal move-out (NMO),

$$\Delta t_{nmo} = t - t_0. \tag{2.5}$$
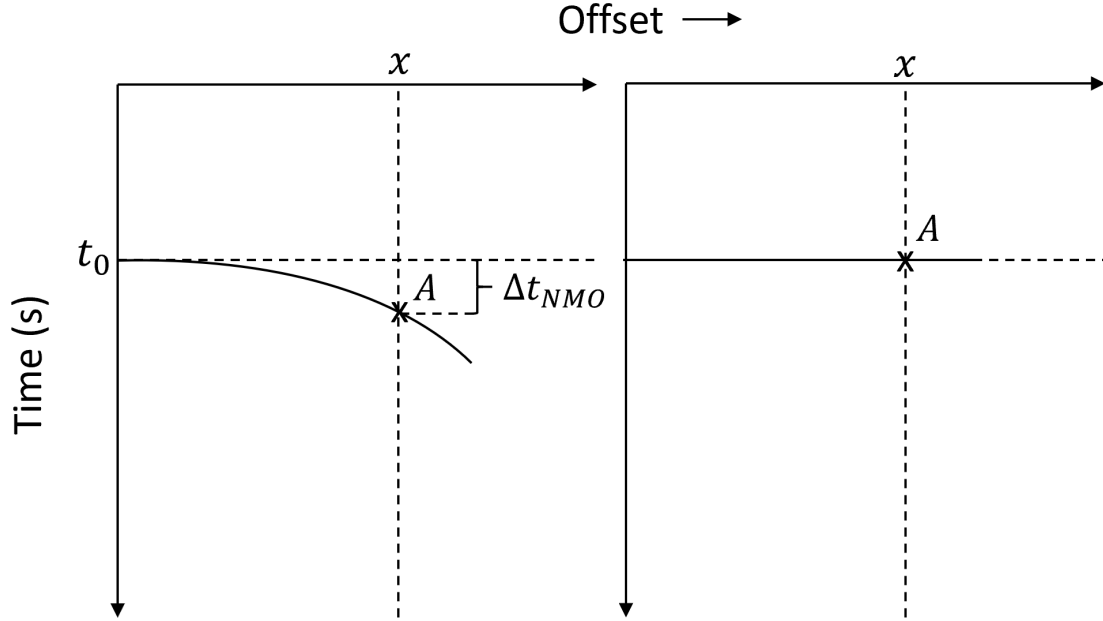
Figure 2.2: *Schematic illustration of an NMO correction (modified from Yilmaz (2001)). Left: the hyperbolic travel time curve pre NMO. Right: flat reflector post NMO.*

By assuming that reflection travel-times follow a hyperbolic trajectory given by equation 2.4, it is possible to remove this effect in order to get reflections that resemble the true geology. Figure 2.2 depicts the scenario, where traces are moved to their true geological location, A. By incorporating equation 2.4 into equation 2.5, the equation for NMO-correction is denoted:

$$\Delta t_{nmo} = t_0 \left[\sqrt{1 + \left(\frac{x}{v_{rms}} \right)^2} - 1 \right]. \tag{2.6}$$

Keep in mind that the velocity needed to correct for NMO is normally defined as the NMO-velcoity. However, the RMS-velocity can be considered a decent NMO-velocity.

2.1.3   NMO stretch

As a result of applying NMO correction, some traces experience stretching. Figure 2.3 describes the process, where the trace at offset x_1 experiences increased period when moved to its true subsurface location. In the time domain, the process is given by Yilmaz (2001) as:

$$\frac{\Delta f}{f} = \frac{\Delta t_{nmo}}{t_0}, \tag{2.7}$$

where f is the dominant frequency, Δf is the change in frequency, Δt_{nmo} is the difference in NMO, and t_0 is the zero-offset travel time. To get a better understanding of how the correction distorts the signal, one can examine the analytical expression

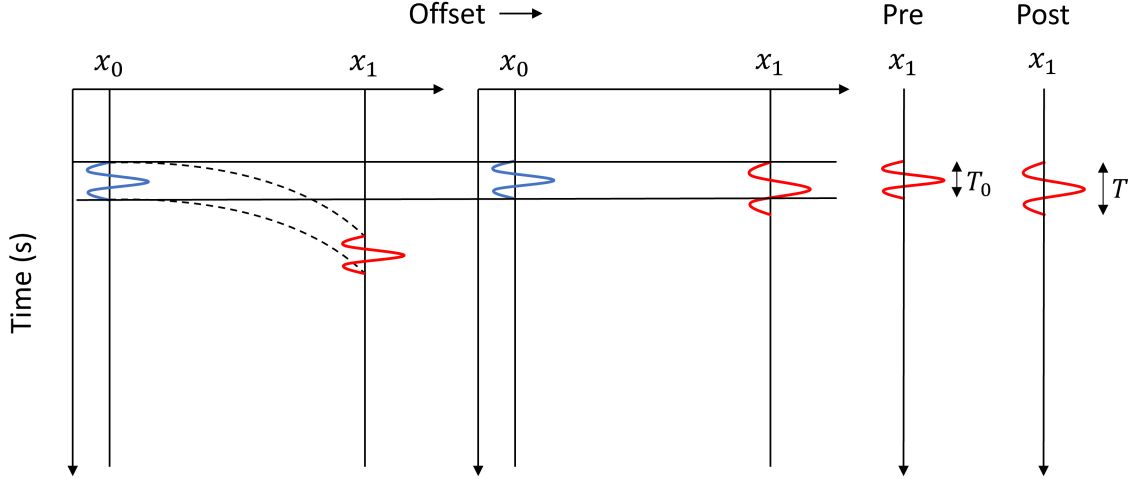**Figure 2.3:** *Schematic illustration of NMO stretch. The left graph depicts the situation pre-NMO, while the right graph represents the results post-NMO. The blue trace represents the zero-offset response, and the red trace is the one being stretched. Pre and post shows trace at x_1 before and after NMO correction. T and T_0 are the periods.*

for NMO stretch in the frequency domain derived by Dunkin & Levin (1973), given by:

$$\tilde{S}_x(f) = \frac{1}{\alpha_x} S_x \left(\frac{f}{a_x} \right), \tag{2.8}$$

where f is the frequency, S_x is the spectrum before NMO, $\tilde{S}_x$ is the spectrum after NMO, and a_x is the ratio of the time difference between the two events before and after NMO correction at offset x. As a_x becomes smaller with increasing offset, the frequency spectrum is reduced, resulting in an increase in period. The amount of move-out correction applied also plays a destructive role, further reducing the spectrum. Basically, shallow far-offset traces experience the most stretch, and have to be muted. In this study we consider NMO stretch to have been properly muted. In time, there has also been developed stretch-free NMO corrections (Perroud & Tygel (2004), Rupert & Chun (1975), Faccipieri et al. (2019)).

2.1.4 Residual move-out

Often the velocity used when correcting for move-out isn't 100% accurate. Over- or under-picking the velocity will result in traces that are slightly misplaced after correction. This small misplacement is referred to as residual move-out (RMO). When analyzing the AVO response, all traces have to be as properly aligned as possible in order to make sure the correct amplitudes are being compared. Even the smallest misalignments causes the AVO response to become in-accurate.

In addition, reflectors rarely confers in a perfect hyperbolic trajectory. Anisotropy or complex overburden may all create non-perfect hyperbolic trajectories. When these are flattened using the approach that follows the assumption that travel time follow

perfect hyperbolic trajectories, one are left with RMO even though the velocity was perfectly picked.

2.1.5 Pre-stack migration

Raw seismic data is oriented with respect to the observation points. Pre-stack migration involves repositioning data elements to their true geological position (Sheriff & Geldart (1995)). It is important reflections are correctly placed when analyzing the AVO response, to make sure the correct amplitudes are compared. In addition to moving reflections to their true subsurface positions, migration also improves the lateral resolution of the data. Increased resolution helps calculating the angle of incidence, which must be accurate for AVO analysis (Downton (2005)).

2.2 AVO/AVA Theory

AVO analysis uses the variation in the reflection coefficient as a function of incident angle to predict reservoir properties. In order for it to be reliable, a certain set of assumptions must be met (Walden (1991)). Firstly, it considers the earth to be a series of flat, homogenous, isotropic layers. Second, it assumes correct removal of geometrical spreading, absorption effects, multiples and other artifacts. In addition, pre-stack migration is assumed to have moved the amplitudes to their correct position.

2.2.1 Richard and Aki approximations

There are many approximations for the reflection coefficients, but only the ones used in this thesis will be presented, which are the ones first presented by Aki & Richards (1980), and then re-arranged by Shuey (1985). The formula is considered a weak contrast approximation for the PP-reflection coefficient as a function of the relative contrast between the elastic parameters (Aki & Richards (1980)), and is given by:

$$R(\theta) \approx \frac{1}{2}(1 - 4\beta^2 p^2)\frac{\Delta\rho}{\rho} + \frac{1}{2\cos^2\theta}\frac{\Delta\alpha}{\alpha} - 4\beta^2 p^2\frac{\Delta\beta}{\beta}, \tag{2.9}$$

where $\Delta\alpha$, $\Delta\beta$ and $\Delta\rho$ are the constrasts between the two layers, while α, β, ρ are the average elastic paramteres, and p is the ray parameter. Shuey (1985) then re-arranged it to:

$$R(\theta) \approx A + B\sin^2\theta + C\sin^2\tan^2, \tag{2.10}$$

where A, B and C are called intercept, gradient and curvature respectively, and are denoted:

$$A = \frac{1}{2}(\frac{\Delta\alpha}{\alpha} + \frac{\Delta\rho}{\rho}), \tag{2.11}$$

$$B = \frac{1}{2}\frac{\Delta\alpha}{\alpha} - 4k^2\frac{\Delta\beta}{\beta} - 2k^2\frac{\Delta\rho}{\rho}, \tag{2.12}$$

$$C = \frac{1}{2}\frac{\Delta\alpha}{\alpha}. \tag{2.13}$$

The intercept, A, and gradient, B, are considered to be at the very heart of AVO analysis. The curvature, C, is only considered important when modelling reflection coefficients above 30 degrees.

2.2.2 Framework for AVO analysis

The AVO response varies depending on the subsurface, and Rutherford & Williams (1989) proposed to categorize the different responses into three classes. Later, the classifications have been extended into four classes that are widely used today. The different classes define AVO behaviour at the top of any layer. The response is directly linked to the layer property and the contrast between the layer and the encasing lithology. The four classes are defined by the sign of the intercept, A and gradient, B, and shown in Figure 2.4.
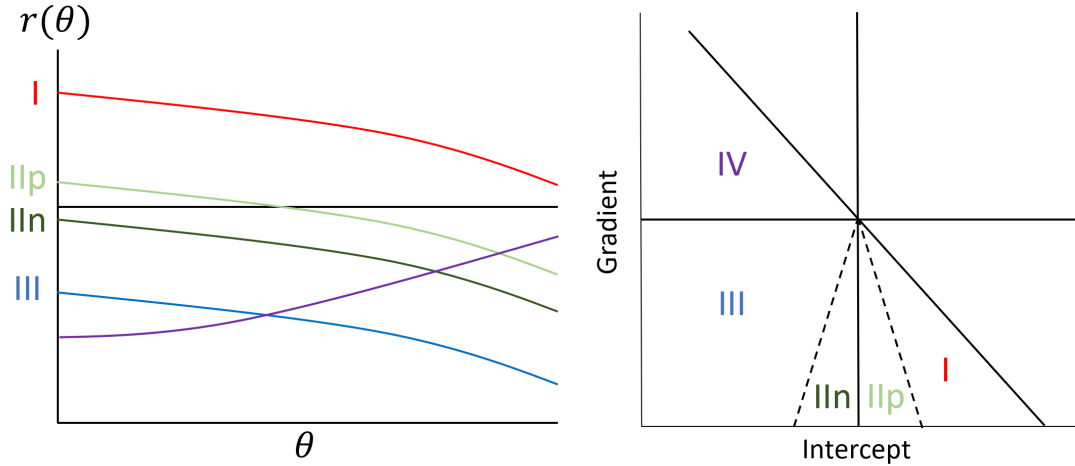
Figure 2.4: *Schematic illustration of typical AVO classes. Left: reflection coefficient as a function of angle. Right: Intercept and gradient cross-plot.*

2.2.3 Estimation of Intercept and Gradient

Estimation of A and B is done by converting the data from offset to angle, and then a popular approach is the least-squares linear regression method to determine the parameters. In this thesis only seismic up to, and including, 30 degrees is used, so it was found sufficient to use the weak contrast two-terms approximation, which is written as the vector product:

$$r(\theta) = A + B\sin^2\theta = \begin{bmatrix} 1 & \sin^2\theta \end{bmatrix}\begin{bmatrix} A \\ B \end{bmatrix}. \tag{2.14}$$

Incorporating several angles into expression 2.14 yields:

$$\mathbf{r} = \begin{bmatrix} r(\theta_1) \\ \vdots \\ r(\theta_n) \end{bmatrix} = \begin{bmatrix} 1 & \sin^2 \theta_1 \\ \vdots & \vdots \\ 1 & \sin^2 \theta_n \end{bmatrix} \begin{bmatrix} A \\ B \end{bmatrix} = \mathbf{Zm}, \tag{2.15}$$

where $\mathbf{Z}$ is a known design matrix, and $\mathbf{m}$ is a vector containing the unknown intercept and gradient. By assuming that the data, $\mathbf{d}$, represents noisy reflection coefficients, it is denoted:

$$\mathbf{d} = \begin{bmatrix} d(\theta_1) \\ \vdots \\ d(\theta_n) \end{bmatrix} = \begin{bmatrix} r(\theta_1) \\ \vdots \\ r(\theta_n) \end{bmatrix} + \begin{bmatrix} e(\theta_1) \\ \vdots \\ e(\theta_n) \end{bmatrix}. \tag{2.16}$$

The equations 2.15 and 2.16, can be summarized as:

$$\mathbf{d} = \mathbf{Zm} + \mathbf{e}, \tag{2.17}$$

where $\mathbf{e}$ is the error. By following the least-squares approach for linear regression, the unknown parameters can be found by the formula:

$$\hat{\mathbf{m}} = (\mathbf{Z}^{\mathbf{T}}\mathbf{Z})^{-1}\mathbf{Z}^{\mathbf{T}}\mathbf{d}. \tag{2.18}$$

2.2.4 Special case estimation of A and B for near and far stacks

In the case of a near and a far stack, A and B are estimated from two points. The linear regression is then reduced significantly. The near stack can be represented as:

$$N = A + B \sin^2 \theta_N, \tag{2.19}$$

where θ_N is the average angle of the near stack. The far stack can be defined as:

$$F = A + B \sin^2 \theta_F, \tag{2.20}$$

where θ_F is the average angle of the far stack. The gradient is then a scaled version of the difference between the near and far stacks, denoted:

$$B = c(F - N), \tag{2.21}$$

where c is the scaling factor given by:

$$c = \frac{1}{\sin^2 \theta_F - \sin^2 \theta_N}. \tag{2.22}$$

The intercept, A can then be estimated by:

$$A = N - B \sin^2 \theta_N. \tag{2.23}$$

2.2.5 Background model

Castagna et al. (1985) presented a generalized mudrock line, which we assume the background model follows, denoted:

$$\alpha = m\beta + b, \tag{2.24}$$

where α is the p-wave velocity, β is the s-wave velocity, $m = 1.16$ and $b = 1360\text{m/s}$. We also assume that the background model follows the law presented in Gardner et al. (1974), denoted:

$$\rho = c\alpha^d, \tag{2.25}$$

where ρ is the density, $d = 0.25$ and $c = 0.31$, which is an empirically derived constant. Seismic following these trends will be referred to as the background model/trend throughout this thesis.

By following these trends, Foster et al. (1993) presented a linear relationship between A and B given by:

$$B = \frac{A}{1 + \beta V_p \rho} \left[1 - \left(\frac{4\beta V_p}{\rho} + \frac{8}{\alpha} \frac{Vp}{V_s} \right) \left(\frac{V_s}{V_p} \right)^2 \right]. \tag{2.26}$$

It is important to note that A and B are linear functions of velocity and density only for small changes. Basically, for brine-filled sediments following the background trend, A and B are co-linear.

2.2.6 AVO fluid factor as rotation in AB domain

The main idea behind the fluid factor is to design a weighted stack that detects hydrocarbons and minimizes the seismic of brine-filled sediments (Smith & Gidlow (1987)). It is defined as a weighted stack of the intercept and gradient, and generally it can be formulated as a rotation in the A-B coordinate system given by:

$$R(\chi) = A\cos(\chi) + B\sin(\chi), \tag{2.27}$$

where χ is the rotation angle, popularly named chi angle.

2.2.7 Linear forward model for a time-angle gather

The synthetic angle-gathers in this thesis have been made following the approach presented by Buland & Omre (2003). The reflection coefficients in (2.2.1) can be written as:

$$r(t, \theta) = a_1(t, \theta) \frac{\partial}{\partial t} \ln \alpha(t) + a_2(t, \theta) \frac{\partial}{\partial t} \ln \beta(t) + a_3(t, \theta) \frac{\partial}{\partial t} \ln \rho(t), \tag{2.28}$$

where

$$a_1 = \frac{1}{2}(1 + \tan^2 \theta$$

$$a_2 = -4k^2 \sin^2 \theta \qquad (2.29)$$

$$a_3 = \frac{1}{2}(1 - 4k^2 \sin^2 \theta).$$

Expression 2.28 can be rewritten to the simpler form of:

$$r(t, \theta) = \mathbf{a}^T(t, \theta)\mathbf{m}'(t), \qquad (2.30)$$

where $\mathbf{m}$ are the elastic parameters in an earth model represented by the vector:

$$\mathbf{m} = \begin{bmatrix} \ln V_P \\ \ln V_S \\ \ln \rho \end{bmatrix}, \qquad (2.31)$$

and $\mathbf{A}$ is the sparse matrix defined as:

$$\mathbf{A} = \begin{bmatrix} A_{1,\theta_1} & A_{2,\theta_1} & A_{3,\theta_1} \\ \vdots & \vdots & \vdots \\ A_{1,\theta_p} & A_{2,\theta_p} & A_{3,\theta_p} \end{bmatrix}, \qquad (2.32)$$

where $\mathbf{A}_{n,\theta_i}$ are diagonal matrices containing a_1, a_2 and a_3 at each time sample. Further, the reflection coefficients between each time sample is defined as $\mathbf{r} = \mathbf{ADm}$, where $\mathbf{D}$ is a finite difference matrix defined as:

$$\mathbf{D} = \begin{bmatrix} D_0 & 0 & 0 \\ 0 & D_0 & 0 \\ 0 & 0 & D_0 \end{bmatrix}. \qquad (2.33)$$

The purpose is to convolve $\mathbf{r}$ with a wavelet vector through matrix multiplication to acquire the data,

$$\begin{bmatrix} d_1 \\ \vdots \\ d_i \\ \vdots \\ d_{na} \end{bmatrix} = \begin{bmatrix} W_1 & \dots & 0 & \dots & 0 \\ \vdots & \ddots & \vdots & & \vdots \\ 0 & \dots & W_i & \dots & 0 \\ \vdots & & \vdots & \ddots & \vdots \\ 0 & \dots & 0 & \dots & W_{na} \end{bmatrix} \begin{bmatrix} r_1 \\ \vdots \\ r_i \\ \vdots \\ r_{na} \end{bmatrix} + \begin{bmatrix} e_1 \\ \vdots \\ e_i \\ \vdots \\ e_{na} \end{bmatrix}, \qquad (2.34)$$

given by $\mathbf{d} = \mathbf{Wr}$, where $\mathbf{W}$ is the block-diagonal wavelet matrix. The equation can also be written as $\mathbf{d} = \mathbf{Gm} + \mathbf{e}$, where $\mathbf{G}$ is the linear forward operator, $\mathbf{m}$ is the vector containing the elastic parameters, and $\mathbf{e}$ is the noise.

2.2.8 Bayesian linearized AVO inversion

The AVO inversion used in this thesis is based on the method proposed by Buland & Omre (2003). Consider the linear forward model

$$\mathbf{d} = \mathbf{Gm} + \mathbf{e}. \tag{2.35}$$

By assuming Gaussian prior,

$$\mathbf{m} \sim \mathcal{N}_{n_m}(\boldsymbol{\mu}_m, \boldsymbol{\Sigma}_m), \tag{2.36}$$

where $\boldsymbol{\mu}_m$ is the prior expectation and $\boldsymbol{\Sigma}_m$ is the prior covariance matrix, and Gaussian likelihood, $p(\mathbf{d}|\mathbf{m})$, given by:

$$\mathbf{d}|\mathbf{m} \sim \mathcal{N}_{n_m}(\mathbf{Gm}, \boldsymbol{\Sigma}_e), \tag{2.37}$$

Buland & Omre (2003) developed an explicit expression for the solution to the inverse problem. The complete solution of the Bayesian inversion is represented by the posterior distribution denoted:

$$p(\mathbf{m}|\mathbf{d}) = \frac{p(\mathbf{d}|\mathbf{m}p(\mathbf{m})}{p(\mathbf{d})}. \tag{2.38}$$

In the linear Gaussian setting defined by Buland & Omre (2003), the posterior distribution can be defined as a conditional Gaussian distribution. The joint distributions of the model parameters $\mathbf{m}$ and $\mathbf{d}$ are defined as:

$$\begin{bmatrix} \mathbf{m} \\ \mathbf{d} \end{bmatrix} \sim \mathcal{N}_{n_m+n_d}\left(\begin{bmatrix} \boldsymbol{\mu}_m \\ \boldsymbol{\mu}_d \end{bmatrix}, \begin{bmatrix} \boldsymbol{\Sigma}_m & \boldsymbol{\Sigma}_{m,d} \\ \boldsymbol{\Sigma}_{d,m} & \boldsymbol{\Sigma}_d \end{bmatrix} \right), \tag{2.39}$$

where $\boldsymbol{\Sigma}_{d,m}$ is the cross-correlation between $\mathbf{d}$ and $\mathbf{m}$,

$$\boldsymbol{\Sigma}_{d,m} = \mathrm{Cov}\{\mathbf{d}, \mathbf{m}\} = \mathbf{G}\boldsymbol{\Sigma}_m, \tag{2.40}$$

and $\boldsymbol{\Sigma}_{m,d}$ is the transpose,

$$\boldsymbol{\Sigma}_{m,d} = \mathrm{Cov}\{\mathbf{m}, \mathbf{d}\} = \boldsymbol{\Sigma}_m \mathbf{G}^T. \tag{2.41}$$

The posterior distribution, $p(\mathbf{m}|\mathbf{d})$, is further given by:

$$\mathbf{m}|\mathbf{d} \sim \mathcal{N}_{n_m}(\mu_{m|d}, \boldsymbol{\Sigma}_{m|d}), \tag{2.42}$$

where the optimal solution vector is

$$\boldsymbol{\mu}_{m|d} = \boldsymbol{\mu} + \boldsymbol{\Sigma}_m \mathbf{G}^T \boldsymbol{\Sigma}_d^{-1}(\mathbf{d} - \boldsymbol{\mu}_d), \tag{2.43}$$

with posterior covariance

$$\boldsymbol{\Sigma}_{m|d} = \boldsymbol{\Sigma}_m - \boldsymbol{\Sigma}_m \mathbf{G}^T \boldsymbol{\Sigma}_d^{-1} \mathbf{G}\boldsymbol{\Sigma}_m. \tag{2.44}$$

The posterior contains the complete solution of the problem, including uncertainty.

Chapter 3

RMO effect on AVO

As a simple example to understand the fundamentals of how RMO effects the AVO response, one can visualize a simple scenario of two layers – a hard shale above a soft brine-filled sandstone. The decrease in acoustic impedance constitutes a negative reflection coefficient. Convolving with a Ricker-wavelet results in a seismic trace representing the reflection for a zero-incident angle. For the sake of simplicity, consider no change in amplitude with offset, meaning the gradient is zero, as in Figure 3.1.
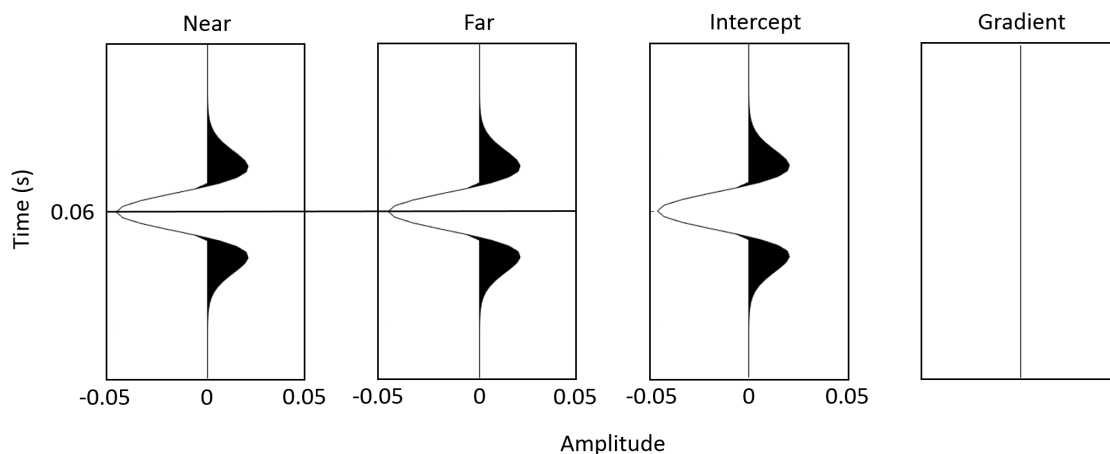

Figure 3.1: *Identical near and far traces, along with the estimated intercept and gradient.*

As the traces are identical, the gradient will be zero. However, if the far trace is shifted in time, either up or down, the gradient will become nonzero. This time shift is the RMO. As seen in Figure 3.2, even a minor time-shift of -2 ms causes a massive effect on the gradient. The intercept on the other hand is barely influenced. Another important observation from Figure 3.2 is that the gradient appears as the derivative of the intercept.
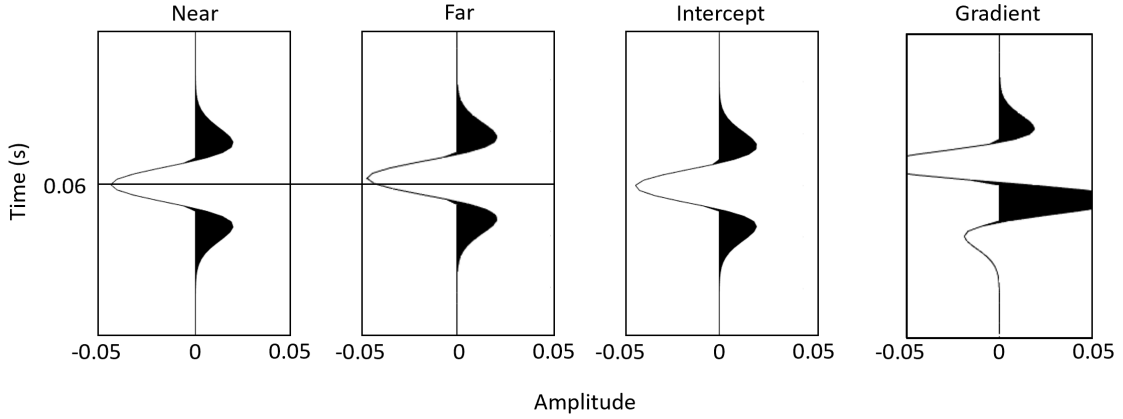
Figure 3.2: *Identical near and far traces, except the far has been shifted $-2\,ms$ in time, along with the intercept and gradient.*

When two traces are identical, the gradient is reduced to the time derivative of the intercept. The scenario is depicted in figure 3.3.
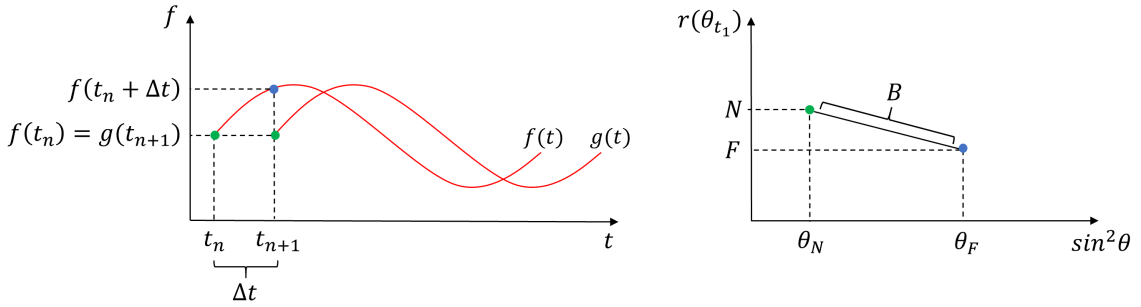

Figure 3.3: *Illustration showing the similarity between the gradient and the derivative. Left: Two identical functions, one of which is moved in time. Right: Near and far stack in an reflection coefficient vs reflection angle plot. Green points represent the Far. Blue points represent the Near.*

The left hand side shows two identical functions $f(t)$ and $g(t)$, one of which is shifted in time. Calculating the slope between the green and blue points in both graphs is the same, so the gradient can be determined by:

$$B = \frac{f(t_n + \Delta t) - f(t_n)}{\Delta t} \tag{3.1}$$

In other words $A'(t) = B$, and they can both be determined accurately by finite difference. Using finite difference to the determine the gradient is possible in this instance, but the larger the time shift, the poorer the gradient estimation is. Regardless, using finite difference results in an absolute value of the derivative of the trace with respect to time. However, this value must be scaled to be a real representation of the gradient, as the angles related to the traces play an important role in gradient estimation. The near stack is said to be 10 degrees and the far stack is 30 degrees, so the scaling factor depends on both of them.

21

The example showed in 3.2 shows how the gradient was affected by shifting the far trace -2 ms. To get a broader understanding of how the AVO response changes with RMO, several values were tested. A normal distribution defined as

$$\Delta t \sim \mathcal{N}(0, \sigma^2), \tag{3.2}$$

with $\mu = 0$ and $\sigma = 2$ ms was made to represent residual move-out. A Monte Carlo simulation was then run to draw 10,000 different values of Δt to see how different amounts of residual move-out affects the estimation of the intercept and gradient.

Figure 3.4 shows the distribution of intercept and gradient at the peak reflection of the reflection in figure 3.2. As seen in Figure 3.4, the intercept is only slightly influenced, and remains remotely close to the reflection coefficient of -0.047. The gradient however, experiences large changes as a function of time shift. It is important to note the difference in number of samples on the y-axis in Figure 3.4. It indicates that most of the estimated intercept values fall within the same values, while the gradient experiences a larger spread due to being heavily affected by adding residual move-out.
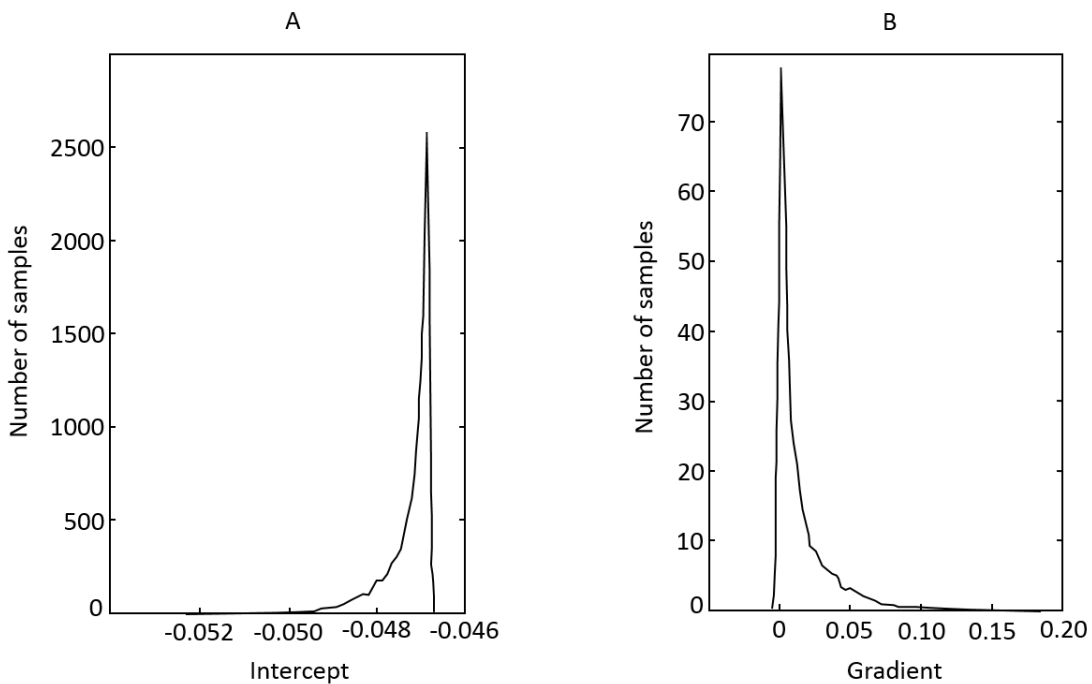

Figure 3.4: *Distribution of A and B after drawing 10,000 random RMO values.*

The main takeaway from this example is that the gradient is heavily altered by small misalignments, while the intercept experiences very small changes.

3.1 Effect on AB-plot

Figure 3.5 shows a near and a far trace completely following the background trend, and their respective intercept and gradient traces. To get an idea of how residual move-out effects the positioning of the individual intercept and gradient points in an AB-plot, the far trace was shifted up and down three milliseconds.
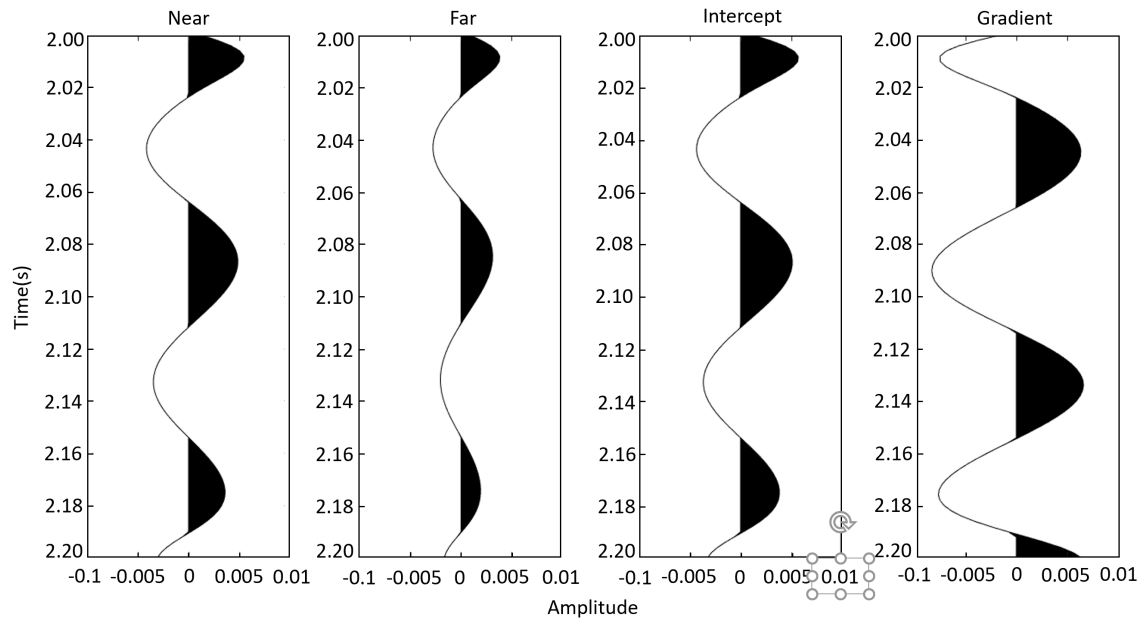

Figure 3.5: *Near and far traces following the background trend, along with the estimated intercept and gradient.*

Figure 3.6 is showing the resulting AB-crossplots when the far trace has been shifted up and down in time. The red points represents the original points when the far trace is correctly placed in time as in Figure 3.5. The blue points depicts the intercept and gradient points after shifting the trace up and down 3 ms. The AB-plot shows that the added residual move-out forces the individual points to deviate from the background trend, which will results in erroneous AVO analysis, specifically increased gradient amplitudes.
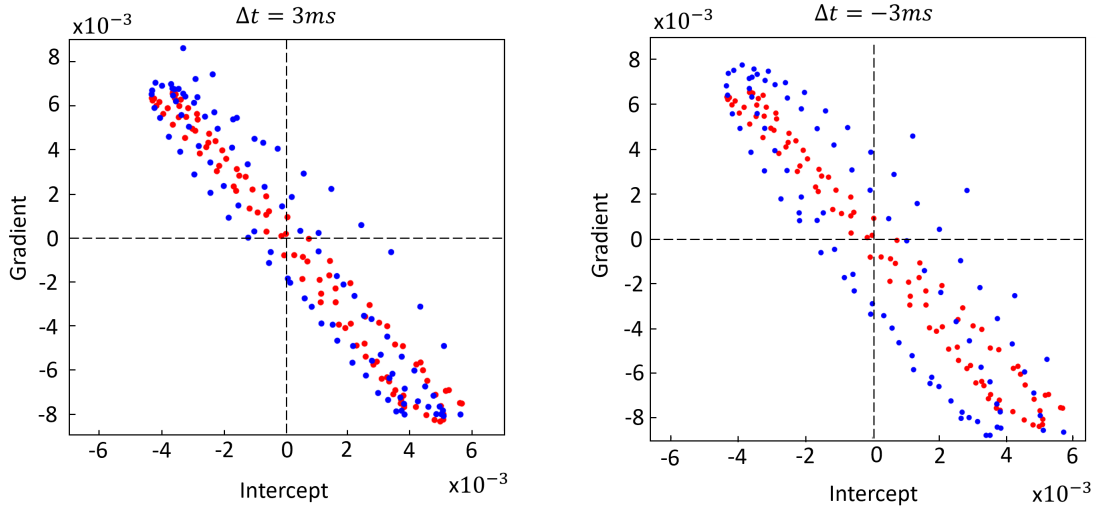
Figure 3.6: *A and B cross-plot for $\Delta t = \pm 3\,ms$. Red points: True AVO response. Blue points: AVO response after adding RMO to the data. Left: $+3\,ms$. Right:$-3\,ms$*

3.2 Apparent RMO

The seismic section showed in 3.5 section is completely following the background trend introduced in 2.2.5, and the optimal AVO response is obtained when the gather is completely flat. However, this isn't always the case. Figure 3.7 shows a seismic section which contains a Class 2n AVO anomaly, together with the corresponding intercept and gradient cross-plot. The red points represent the part of the seismic following the background trend, while the blue points are in the anomaly interval. Several of the reflectors in the interval between $t = 2.06\,\text{s}$ and $t = 2.16\,\text{s}$ are appearing to bend upwards with increasing angle. This behaviour might be mistaken as RMO, when it is in fact an AVO response. Hence, the term apparent residual move-out is presented. Apparent RMO brings us back to the main objective of this thesis, which is to propose a new method to correct for residual move-out that properly handles these important events.
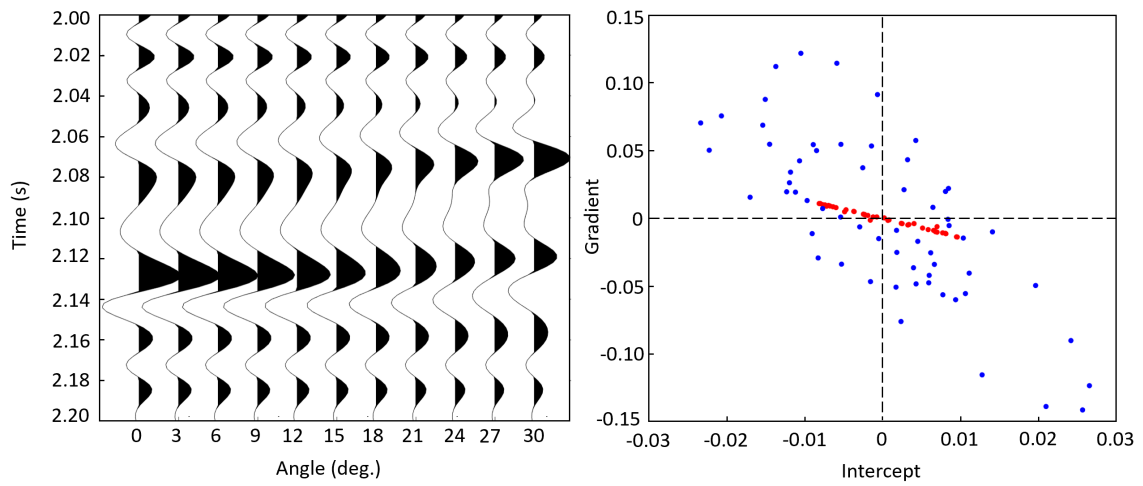
Figure 3.7: *Left: seismic gather illustrating apparent RMO. Right: the corresponding AVO response. Red: the seismic following the background trend (above and below the anomaly). Blue: points in the anomaly interval.*

Chapter 4

Data

Four methods will be tested on two synthetic sections of seismic data, with and without noise. One is a trend completely following the background trend explained in subsection 2.2.5, and another is a Class 2p anomaly experiencing apparent RMO. The purpose is to see how the different methods impact the AVO responses.

4.1   Model 1: Background trend

Figure 4.1 shows the seismic section completely following the background trend. It is smoothly varying, with an overall increasing trend of elastic parameters with depth. There are two major reflections in the gather, a trough at $t = 2.12$ s associated with the huge decrease in elastic parameters. In addition, there is a large peak at $t = 2.25$ s associated with a large increase in elastic parameters. Other than that, the rest of the reflections are results of small to medium contrasts. This section will be referred to as Model 1 throughout the thesis.
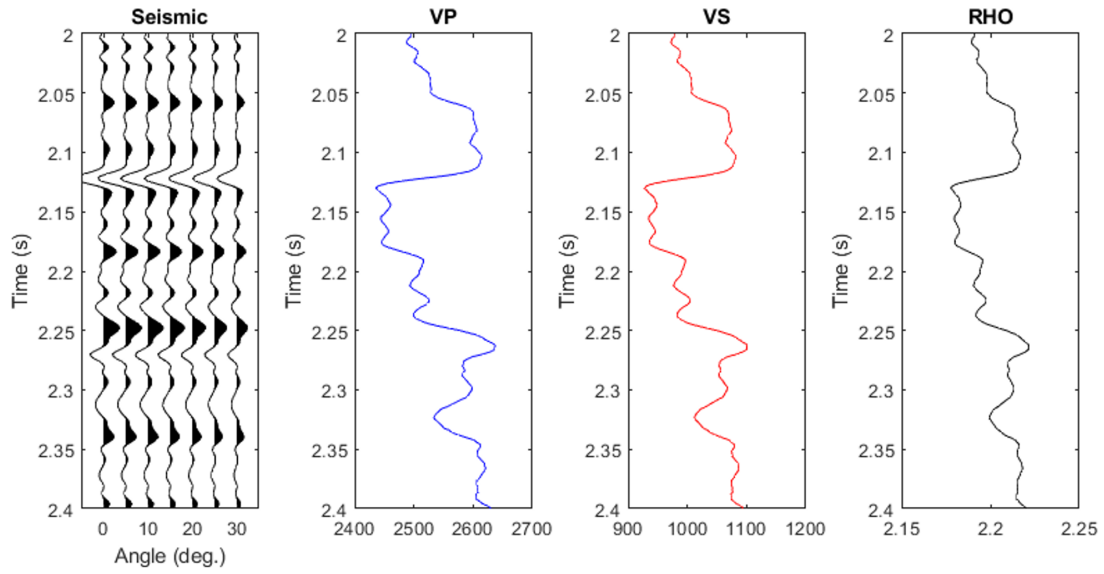
Figure 4.1: *Synthetic data following the background trend, along with the corresponding elastic parameters.*

4.2   Model 2: Class 2p anomaly

In addition to a seismic section completely following the background trend, another was also made. Figure 4.2 shows a seismic section with a Class 2p anomaly at approximately $t = 2.1\,\mathrm{s}$. By closely examining the seismic at this time, one can clearly see a strong trough appearing to bend downwards with increasing offset. This is a direct response to the AVO anomaly. As mentioned, this behavior can be misinterpreted as residual move-out, and is called apparent RMO throughout this study.
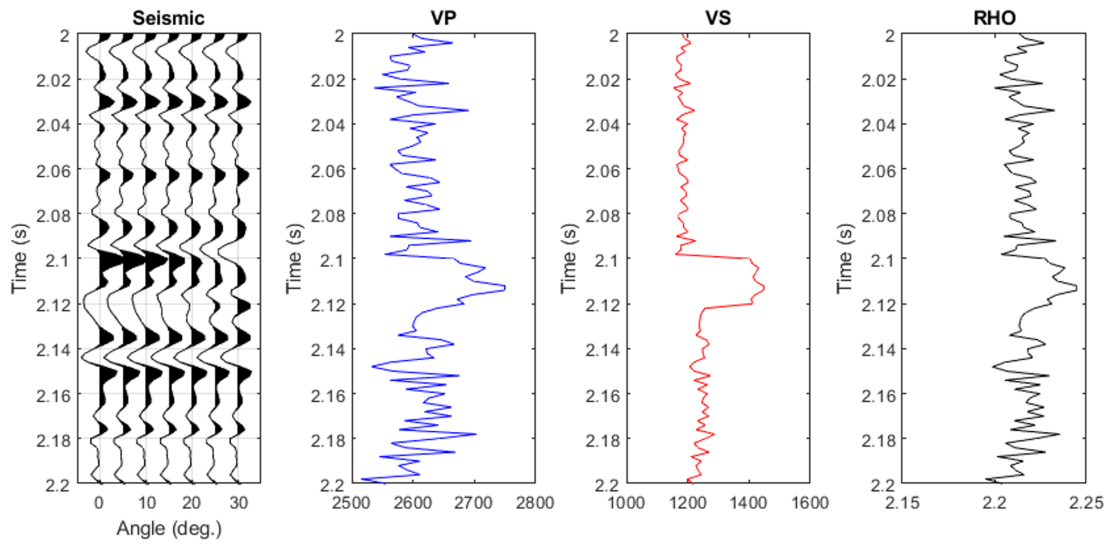
Figure 4.2: *Synthetic data containing AVO Class 2p anomaly at t = 2.09 s, together with the elastic parameters.*

When the gather contains more seismic following the background trend, it may outweigh the anomaly. Considering this thesis only uses a static approach to correcting for residual move-out, the anomaly would be correctly handled simply by correcting the seismic following the background trend. As the main purpose of testing the methods on the section containing the anomaly is to specifically see how they react to apparent RMO, it was cropped out of the seismic to make sure the background trend did not outweigh it. Figure 4.3 shows the cropped section only containing the reflection with apparent RMO. By looking at Figure 4.3, it the apparent RMO is even clearer.
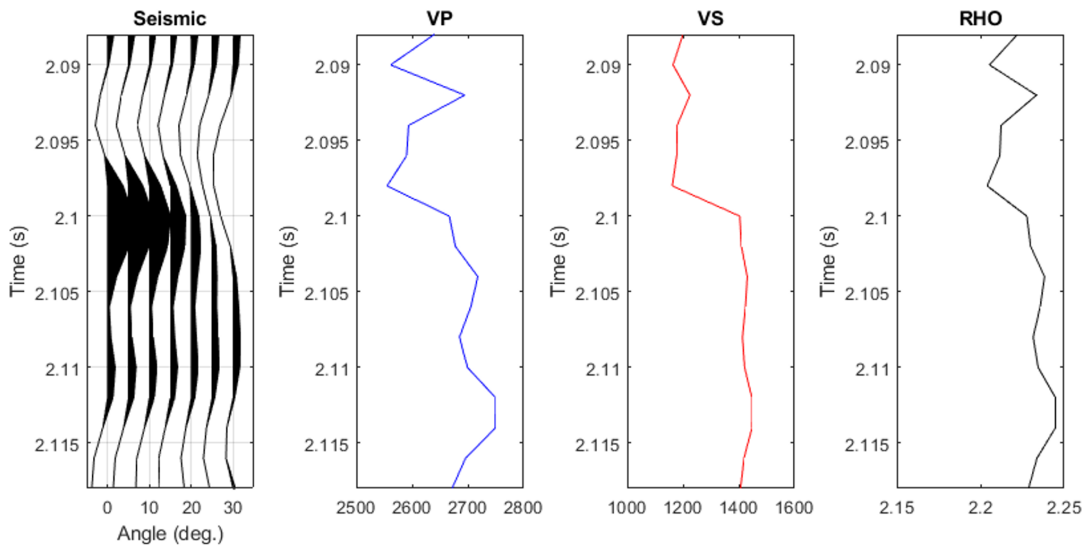

Figure 4.3: *AVO anomaly Class 2p cropped from the entire gather, along with the elastic parameters.*

28

4.3 Representation of noise

In addition to the two gathers shown, two identical gathers containing noise were made. The noise added was white Gaussian noise defined by normal distributions. For Model 1, the one following the background trend, noise was added on the form,

$$\mathbf{e}_1 \sim \mathcal{N}(\boldsymbol{\mu}_e, \boldsymbol{\sigma}_e^2 \mathbf{I}), \tag{4.1}$$

with $\boldsymbol{\mu}_e = 0$ and $\boldsymbol{\sigma}_e = 0.001^2$.

For the gather containing the anomaly the noise was defined as:

$$\mathbf{e}_2 \sim \mathcal{N}(\boldsymbol{\mu}_e, \boldsymbol{\sigma}_e^2 \mathbf{I}), \tag{4.2}$$

with $\boldsymbol{\mu}_e = 0$ and $\boldsymbol{\sigma}_e = 0.003^2$.

The noise was added to the seismic to test how the methods perform when there is some kind of distortion in the seismic. It is important to note that random white noise in is no way more damaging than noise that resembles primary reflection, like multiples. However, it does distort the signal to some extent, which in return should make it slightly harder on the methods.

4.4 Representation of RMO

An important part of this thesis is the mathematical representation of residual move-out. In Chapter 2, the theory behind the presence of residual move-out was discussed and linked to different sources. The simplest being errors in the velocity model, and a more complicated reason being linked to anisotropy and complex geology. As a result, this thesis will utilize one approach to add move-out to the data. We consider the source of the residual move-out to be irrelevant. As the purpose of this thesis is only to make AVO analysis more robust, and not improve the velocity model, we neglect the source but still consider it to be present. Throughout this study, RMO is assumed to be a slowly varying polynomial function, Δt, defined as:

$$\Delta t(\theta) = a\theta^2 + b\theta + c. \tag{4.3}$$

Considering the RMO is zero when the angle is zero, the last term, c, is neglected. By removing c one ensures the move-out curve is properly constrained, and the expression is reduced to:

$$\Delta t(\theta) = a\theta^2 + b\theta, \tag{4.4}$$

where b defines a linear line, while a allows for smooth curvature. Henceforth, Δt will be referred to as a move-out curve.

Chapter 5

Semblance/Max stack

Even though this thesis focuses on post-processing preconditioning of the data for AVO analysis, there exist techniques used during processing that are useful. Semblance, a measure of coherence, is considered one of the classical approaches used for velocity picking during processing of seismic data, but can be applied for residual move-out correction too. It is important to note that while processing the data, semblance is used as a method to find the velocity that results in the maximum stacking amplitude, which is not necessarily the optimal velocity for AVO analysis. Nonetheless, this chapter will review the use of Semblance as a method to correct for residual move-out post-processing, and explore how the methods sensitivity to small velocity variations impact the AVO response.

5.1 Theory and implementation

Stacked amplitude S along the hyperbolic trajectory given by two-way travel-time t_j is denoted:

$$S(t_j) = \sum_{i=1}^{M} d(x_i, t_j(x_i)),\tag{5.1}$$

where $S(t_j)$ is the stacked amplitude along two-way travel-time t_j, M is the number of traces, d is the amplitude at offset x_i at time $t_j(x_i)$. Basically, one calculates the stacking amplitude along different hyperbolic trajectories, using the formula for two-way travel time with different trial velocities:

$$t_j(x_i) = \sqrt{t_0^2 + \frac{x_i^2}{v_{rms}^2}},\tag{5.2}$$

where v_{rms} is the RMS-velocity which provides a decent stack. The hyperbolic trajectories given by expression 5.2 are directly linked to velocity-error, which is why

the maximum stacking amplitude is popular during velocity model building. Semblance is considered the normalized output-to-input energy ratio (Yilmaz (2001)), which is given by:

$$NE = \frac{1}{M} \frac{\sum_t \sum_{i=1}^{M} d(x_i, t_j)}{\sum_t \sum_{i=1}^{M} d(x_i, t_j)^2}. \tag{5.3}$$

There are several factors that need consideration when implementing this method. When working in the time-domain, it is only possible to shift traces up and down whole samples, unless one re-samples the data and interpolate in between, this reduces the accuracy needed when preconditioning the data for seismic analysis. On the other hand, in the fourier domain it is possible to accurately move traces up and down as a linear phase shift. In order to make the method as accurate as possible, a slightly different approach was taken. Firstly, the algorithm was designed to find the strongest reflection, then a window was set around it. The difference is located in the next step, where the trajectory was chosen to be a fixed flat line at the zero-offset time of the strongest reflection. A trial a and b in $\Delta t = a\theta^2 + b\theta$ was set, and the resulting residual move-out was applied to the seismic. The stacking amplitude along the flat line is then the stacking amplitude obtained at the given move-out curve, Δt. Basically, instead of having a fixed seismic section and making several trajectories, the trajectory was fixed and the seismic was moved up and down in the fourier domain. In addition, the method is linked to a and b rather than velocity. This approach was considered an easy solution to ensure the accuracy was at the level needed. The obtained stacking amplitudes along the trajectory for the different velocity errors were then normalized within the chosen window.

5.2 Examples

The purpose of implementing semblance was to see how it would work as a post-processing method to correct for residual move-out. In addition, to see if the methods sensitivity to small changes in the move-out curve is sufficient. Residual move-out was added to Model 1 in the form of $\Delta = 0.02\theta^2 + 0.002\theta$, depicted by the move-out curve in Figure 5.1
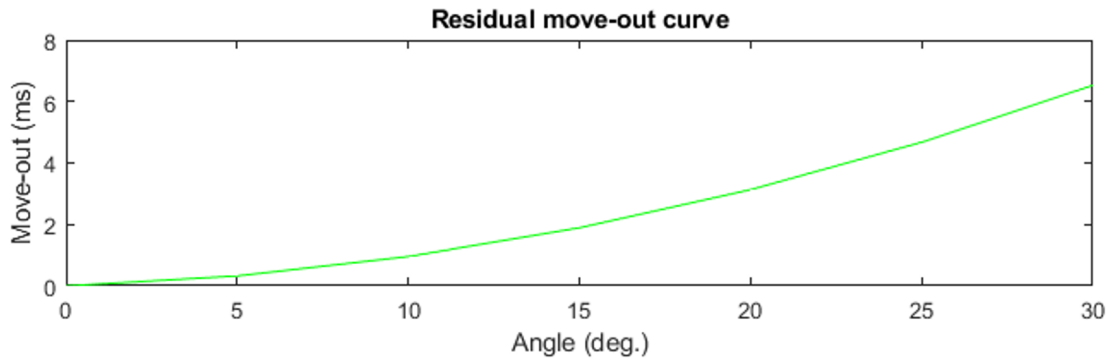

Figure 5.1: *Move-out curve representing the residual move-out added to Model 1 prior to testing Semblance.*

The second model, which contains the anomaly, was left un-touched as the purpose of applying Semblance to this gather was to see how it reacts to apparent RMO.

5.2.1   Model 1: Background trend

Figure 5.2 shows three seismic sections, and the trajectory which the stacking amplitude was calculated on. Several values of a and b were tested to calculate the stacked amplitude along the line, to see which parameters resulted in the highest amplitudes. The left gather is the original model, the middle gather is after applying the move-out curve in Figure 5.1, and the right gather is the results obtained post-correction. There is clear improvement in the gather, and it appears to be completely flattened. It is important to note that the move-out required to cancel the residual move-out applied by the curve in Figure 5.1, is the exact same, but negative to reverse the changes. In other words, the resulting move-out curve should be a perfect mirror-image of the one in Figure 5.1.
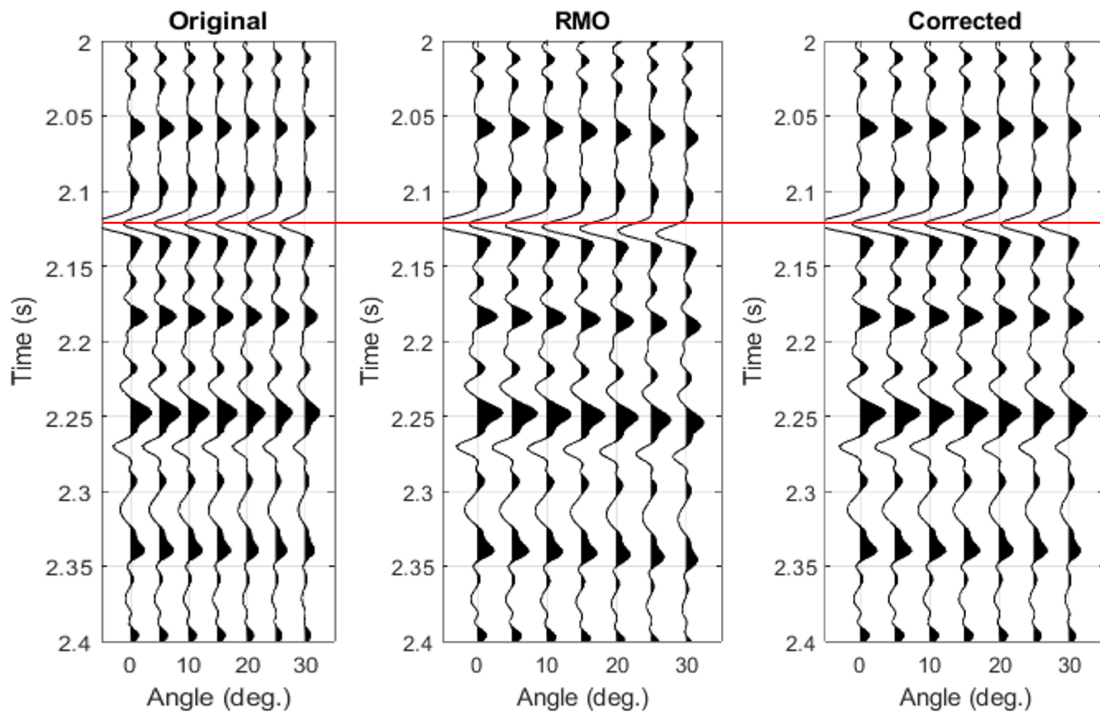

Figure 5.2: *Three gathers following the background trend. Left: original gather. Middle: gather with added RMO. Right: gather obtained after using Semblance. Red line: line which the amplitudes were stacked.*

Figure 5.3 shows the move-out curve applied to the seismic in green, while the blue curve represents the answer obtained by semblance. The absolute value of both move-out curves has been plotted, to make it easier to compare them. The two move-out curves are very similar, with slight changes towards the higher angles. The maximum difference in move-out is only 0.35ms. The right hand side of the

figure shows the semblance plot. It is important to remember that the normalized stacking amplitude was only calculated at one time sample, the one at the largest reflection which is the trough at the red line in Figure 5.2. Thus, the semblance plot is for this one time sample. The difference in color represents the different trajectories obtained by changing a and b. The top x-axis is the trajectory number, while the bottom x-axis shows the RMO at 30 degrees. Dark blue represents high stacking amplitude, while yellow is low. It can be clearly seen in the figure that several values show dark blue, but the highest stacking amplitude was acquired for trajectory 8, when the RMO at 30 degrees is 0.35ms. The true answer is trajectory 7, when the RMO is zero. Keep in mind that the true trajectory is also dark blue, but with slightly lower normalized stacking amplitude. The erroneous difference in stacking amplitude between the obtained and true answer is related to the methods sensitivity to small change in the move-out curves.
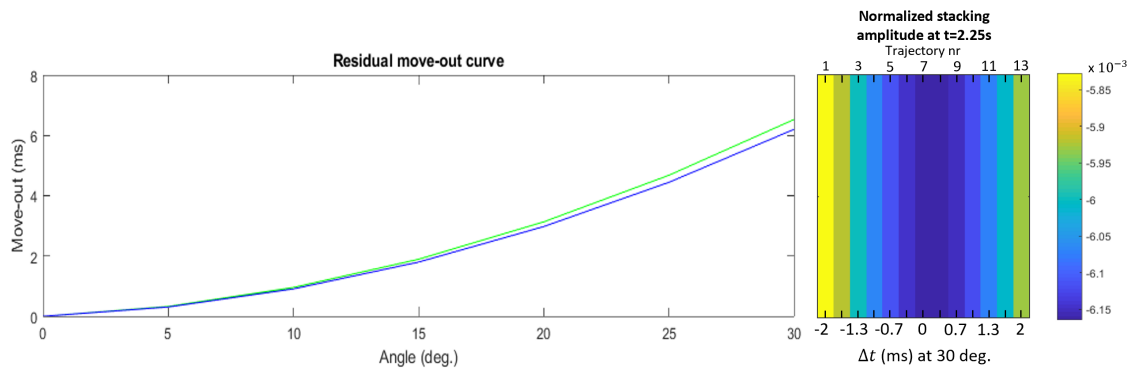

Figure 5.3: *Left: True move-out curve in green. Move-out curve obtained post-Semblance in blue. Right: Semblance plot for $t = 2.25$ s. Top x-axis: trajectory number. Bottom x-axis: Δt at 30 degrees.*

The method was also tested on noisy seismic to see how white Gaussian noise affects the sensitivity. In Figure 5.4, the same three gathers are shown with noise. The corrected gather shows clear improvement, and it seems to have been correctly flattened.
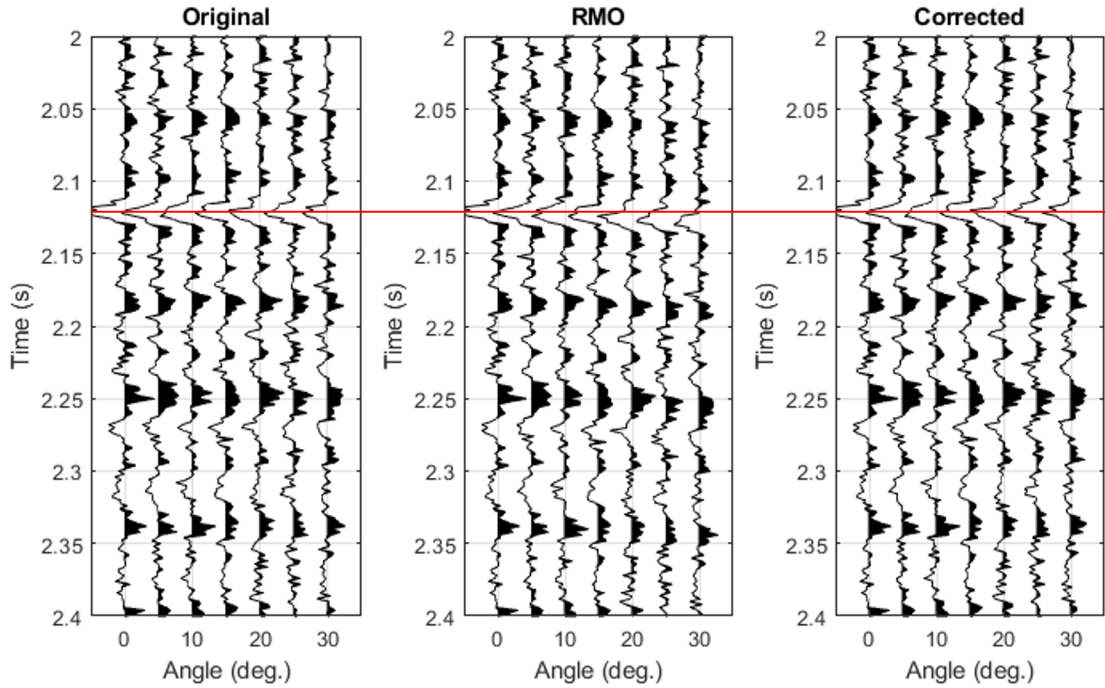
Figure 5.4: *White Gaussian noise. Three gathers following the background trend. Left: original gather. Middle: gather with added RMO. Right: gather obtained after using Semblance. Red line: line which the amplitudes were stacked.*

Figure 5.5 shows the comparison of the move-out curves. Even with the presence of noise, the curves are nearly identical, except for changes at the higher angles. Nonetheless, the difference here is not even close to being one whole sample. The semblance plot differs a lot from the one for the noise-free seismic, and the maximum normalized stacking amplitude was acquired at trajectory number 5, when the RMO is -0.7ms. Trajectory number seven represents the true answer, and based on the plot there appears to be at least 3 trajectories with higher stacking amplitudes, suggesting the sensitivity of the method decreases significantly with increasing noise.
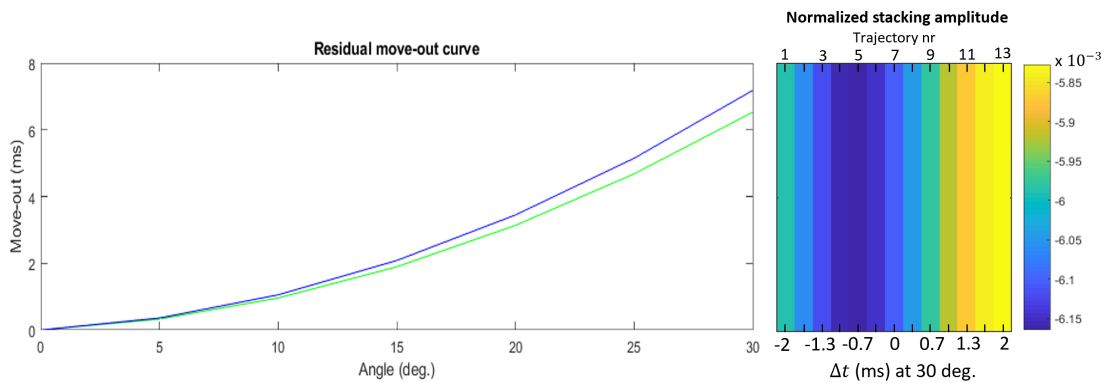

Figure 5.5: *Left: True move-out curve in green. Move-out curve obtained post-Semblance in blue. Right: Semblance plot for $t = 2.25$ s. Top x-axis: trajectory number. Bottom x-axis: Δt at 30 degrees.*

34

5.2.2 Model 2: Class 2p anomaly

The method was also tested on the gather containing the Class 2p anomaly. As mentioned, the gather was kept unchanged to see how Semblance reacts to apparent RMO. The left side of Figure 5.6 shows the true seismic, the middle gather represents the seismic after applying Semblance, and the right hand side shows the Semblance plot. The strongest reflection in which the stacking amplitude was calculated for is located at the red line. The method clearly has done what it is intended to do, find the a and b which result in the highest normalized stacking amplitude. However, in doing so, the anomaly has been completely altered. The trough at approximately $t = 2.095s$ is bending downwards in the true seismic, but is shifted in time to the point of doing the exact opposite.

As the strongest reflection was a peak in this model, the highest normalized stacking amplitude is positive which is represented by bright yellow. Trajectory number 8, when Δt is zero represents the original seismic. As shown by Figure 5.6, all negative values of Δt results in higher stacking amplitude than for trajectory nr 8. This means the stacking amplitude increases in the direction of wrongly flattening the reflection.
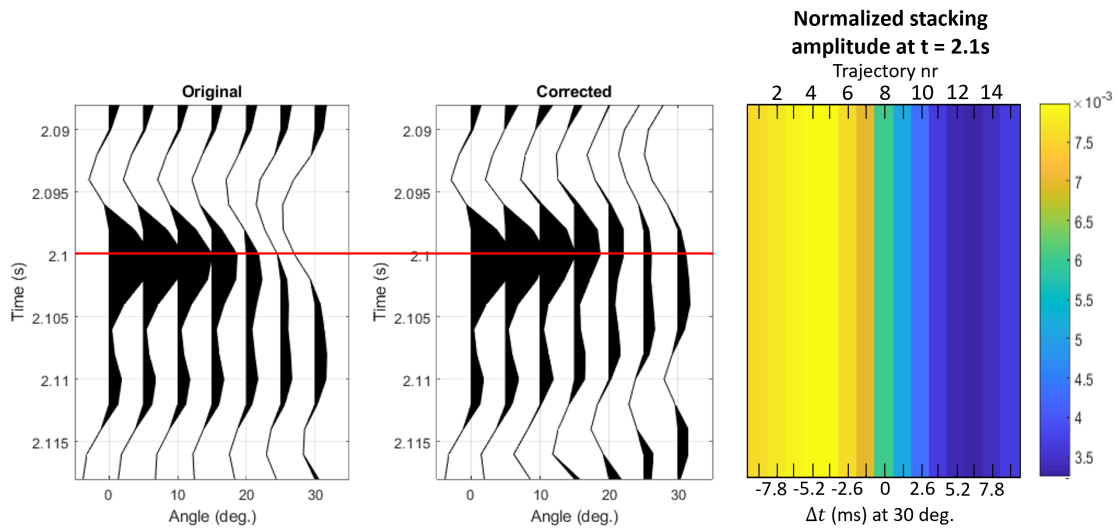

Figure 5.6: *Left: original AVO anomaly. Middle: The gather obtained after Semblance. Red line: line which the stacking amplitude was calculated on. Right: Semblance plot for $t = 2.1$ s. Top x-axis: trajectory number. Bottom x-axis: Δt at 30 degrees.*

The method was also applied on seismic containing white Gaussian noise. Figure 5.7 shows the original gather along with the post-Semblance gather. The right side of Figure 5.7 is the Semblance plot for $t = 2.1$ s. The case is the same as for the noise-free seismic. The peak at $t = 2.1$ s is flattened, which in return alters the trough between $t = 2.09$ s and $t = 2.095$ s to bend upwards. The peak which the stacking amplitude was calculated on is flattened. By examining the Semblance plot, the highest value is obtained at large negative move-out (bright yellow).
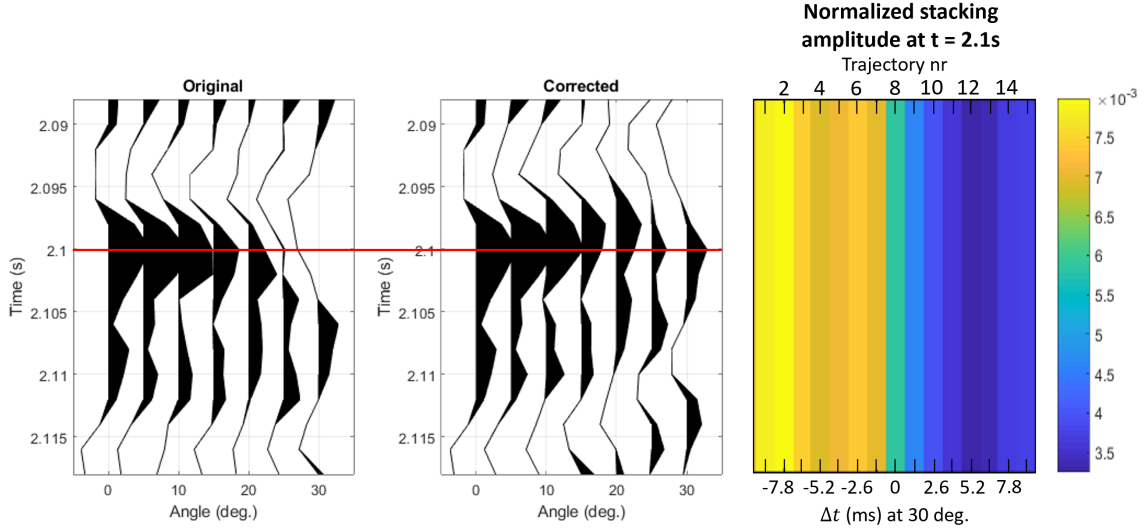
Figure 5.7: *Noisy seismic. Left: AVO anomaly pre-correction. Middle: seismic section post-correction. The red line represents the line which the stacking amplitude was calculated on. Right: Semblance plot at t = 2.1 s. Top x-axis: trajectory number. Bottom x-axis: Δt at 30 degrees.*

5.2.3 Discussion

The application of Semblance as a post-processing tool to correct for residual move-out was tested on the model following the background trend, and the gather containing an AVO anomaly. The results obtained on Model 1 show that the method does a great job in removing most of the residual move-out. The normalized stacking amplitude was not along the true trajectory, but very close. When white noise was added to the seismic, the sensitivity of the method decreased, and there were several trajectories with higher stacking amplitude than the true one. That being said, they were all a clear improvement to the gather altered with residual move-out. All in all, the method can be considered a simple, yet robust way to partially correct for residual move-out in the presence of brine filled layers.

For model 2 the case was quite different. As mentioned, no RMO was added to the gather containing the anomaly, as the purpose was to see how Semblance reacts to apparent RMO. As expected, the highest stacking amplitudes were along trajectories seemingly working towards flattening the reflection, which is considered a weakness as based on this observation, the user is advised to avoid known anomalies.

Other weaknesses are related to the nature of the approach. The purpose of using Semblance is to obtain the best stack. When preconditioning the data for AVO, we are only after the proper alignment of corresponding reflections, which often contradicts the best stack. Another weakness to the method is related to the uni-modal output. It does not provide any indication whether the user is under- or over-correcting the seismic. Lastly, there is one weakness to how the method was implemented in this thesis - a static approach. However, there have been developed dynamic approaches to implementing semblance where traces are being stretched

and squeezed to find better fits(Rickett & Lumley (2001), Wolberg (1990)). There are also other newly proposed methods to greatly improve semblance when there are multiples present, by combining it with dip filtering to supress multiple reflections (Li & Symes (2007)). These are all examples on the broad applications of Semblance.

5.3 AVO Analysis

Considering the purpose of this thesis is to determine the usefulness of several methods to precondition data for seismic analysis, it is only natural to examine the difference done to the AVO response. Intercept and gradient points were estimated for both models before and after the application of Semblance, to see the responses compare to the true AVO response. In addition, the coordinate system was rotated to obtain a fluid cube for Model 1. As the second model only contains an anomaly, the purpose of rotating the coordinate system to highlight one feature while removing another is lost. For this reason, there were not done any chi angle rotations for Model 2 in any of the chapters.

5.3.1 Model 1: Background trend

Figure 5.8 shows an intercept and gradient cross plot. The green points represent the true AVO response, while the red points is the AVO response after adding residual move-out to the data. The blue points depict post-Semblance response. The left figure represents noise-free seismic, while the right plot is in the presence of white Gaussian noise. In the noise-free case, there is clear improvement. The removal of residual move-out corrects the AVO response to the point of almost completely overlapping with the true. The spread of the points is completely removed, suggesting the gradient has the correct amplitudes at all time samples. The inclination of the trend followed by the points is reduced, making it correct, suggesting the vp/vs relationship is improved. For the gather containing noise, the difference is not as noticeable. In fact, the AVO response appears to not have improved much at all. Neither the inclination of the trend, nor the spread is affected much. This is likely related to the methods decreased sensitivity in the presence of noise.
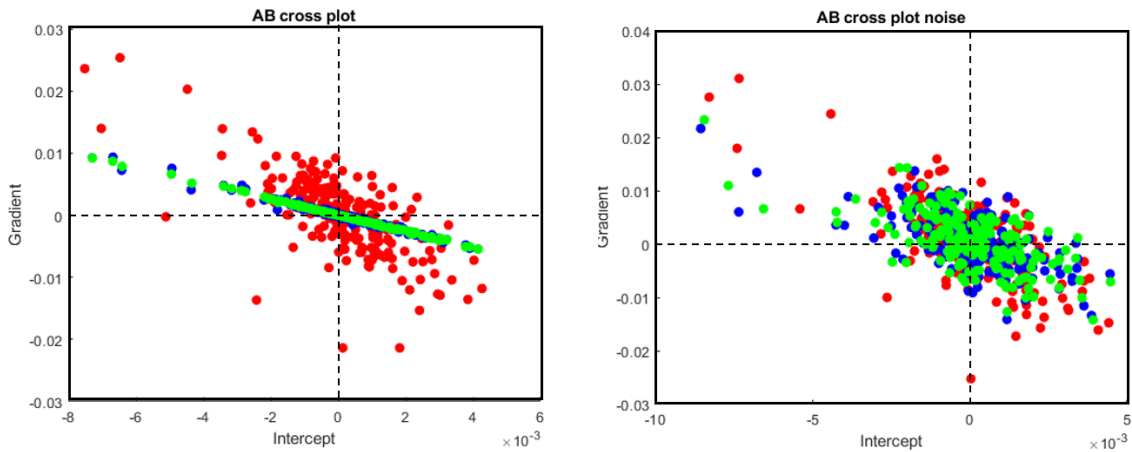
Figure 5.8: *Model 1 intercept and gradient cross-plot. Green: true AVO response. Blue: after correcting the seismic with Semblance. Red: after adding RMO. Left: Noise-free gather. Right: white Gaussian noise.*

The difference done to the AVO response is not always easily seen in cross-plots, especially for noisy seismic. To further investigate the change done to the intercept, the traces are shown by Figure 5.9. The figure shows all the intercept traces next to each other, with and without noise. There is hardly any difference done to the intercept, which is expected as it is barely influenced by small amounts of RMO, as discussed in Chapter 3.
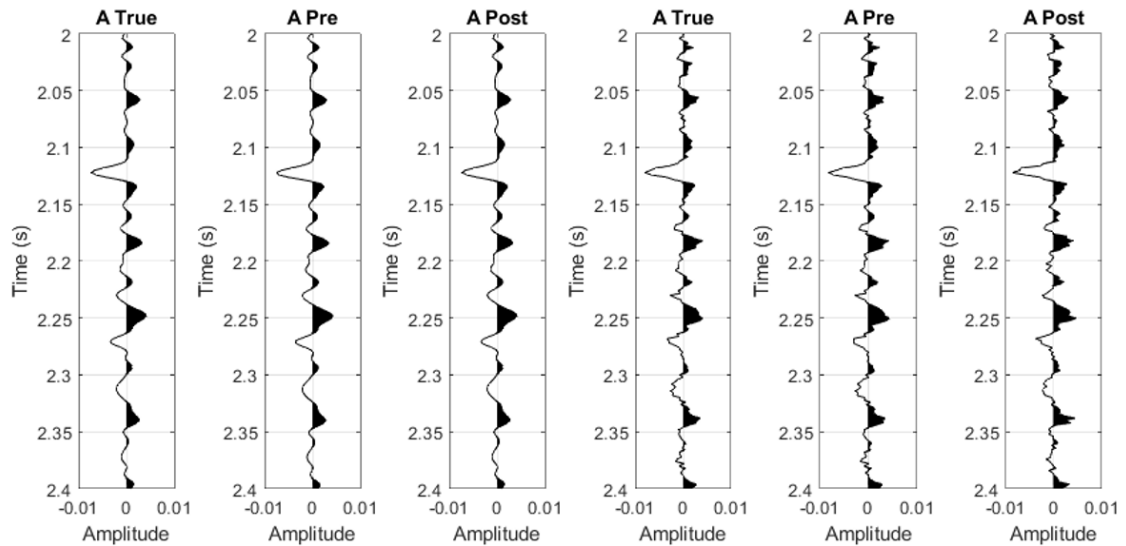

Figure 5.9: *Model 1 intercept traces. True: original gather. Pre: after adding RMO. Post: after correcting for RMO with Semblance. Three to the left: noise-free. Three to the right: white Gaussian noise.*

The gradient traces in Figure 5.10 shows the difference the tiny misalignment results in. When the true seismic is distorted with RMO, the amplitudes of the gradient are heavily increased as seen in the pre-traces. After the application of Semblance, the

"post" gradient is reduced to the original amplitudes for the noise-free case. In the presence of noise, there is not much of an improvement. This is further evidence the AVO response for the noisy seismic was not improved due to the methods decreased sensitivity in the presence of noise.
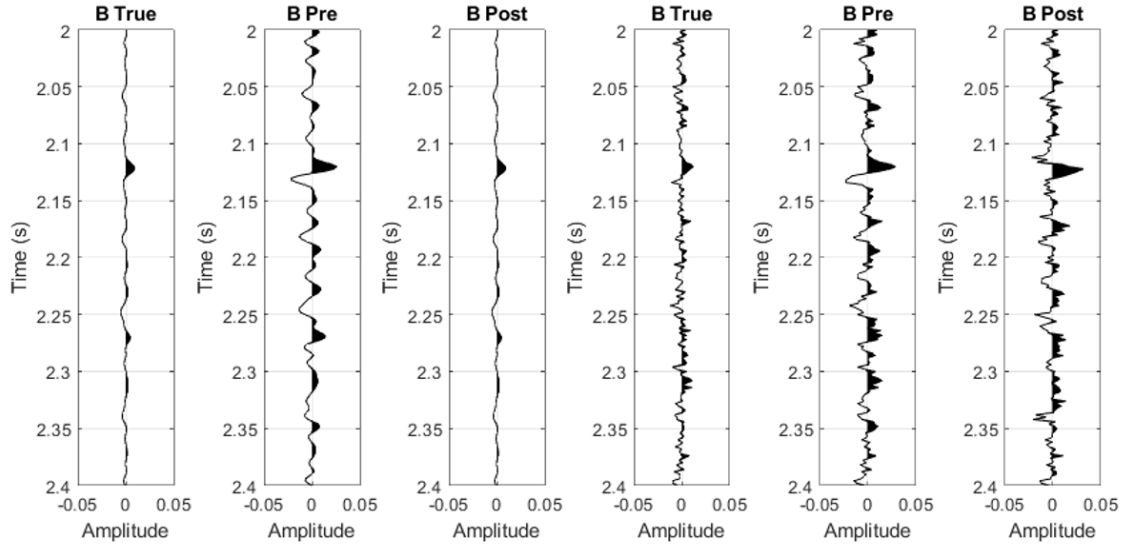

Figure 5.10: *Model 1 gradient traces. True: original gather. Pre: after adding RMO. Post: after correcting for RMO with Semblance. Three to the left: noise-free. Three to the right: white Gaussian noise.*

Figure 5.11 shows the fluid traces obtained by rotating the coordinate system. By comparing the pre-correction fluid trace to the true and post-correction traces, one can observe clear differences. Adding RMO to the data distorts the AVO response, making the rotation angle not as effective. By applying Semblance to remove the RMO, the amplitudes are returned to the original value of near-zero. As inferred from the cross plot and intercept and gradient traces, there was not much improvement to the AVO response for the gather containing noise. The true fluid trace has significantly smaller amplitudes than the pre and post traces. This is a further indication on that the inclination is not improved at all.
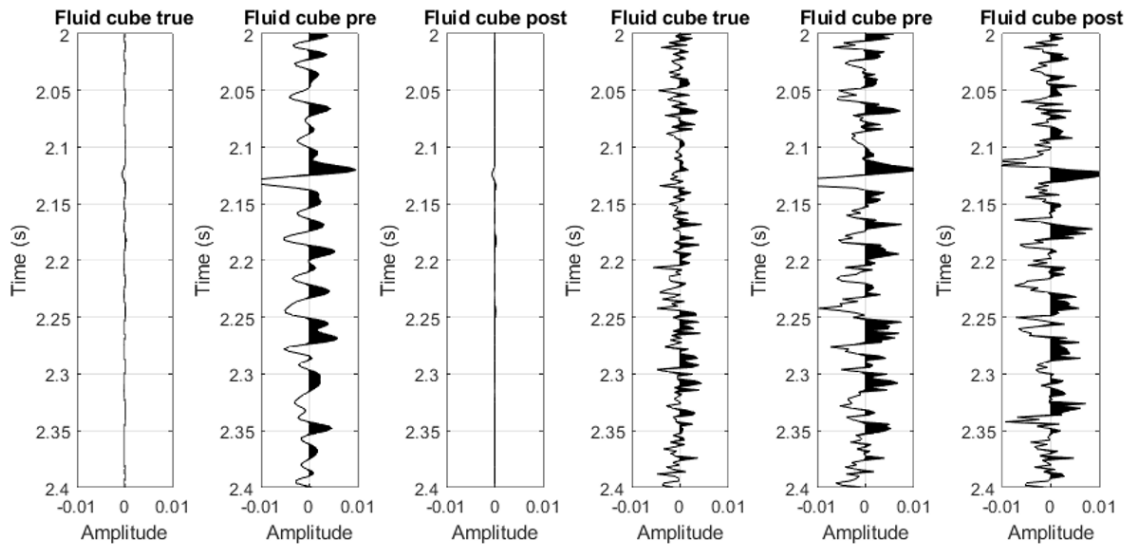
Figure 5.11: *Model 1 fluid traces: True, pre- and post-correction for seismic with and without noise. Three left traces are without noise, three right traces are with noise.*

5.3.2 Model 2: Class 2p anomaly

The results showed that Semblance handled the anomaly as expected - it flattened it. To see how severe of an impact this has on the AVO response, the intercept and gradient were cross-plotted for the seismic sections with and without noise, as seen in Figure 5.12. The green points represent the true AVO response, while the blue points show the AVO response after wrongly flattening the apparent RMO. Left side is for the noise-free case, while the right is in the presence of white noise. As there are not too many points, it is hard to make much of the difference only by looking at the cross-plot. The main observation is that the spread of the points for the noise-free case seem to decrease in the gradient direction.
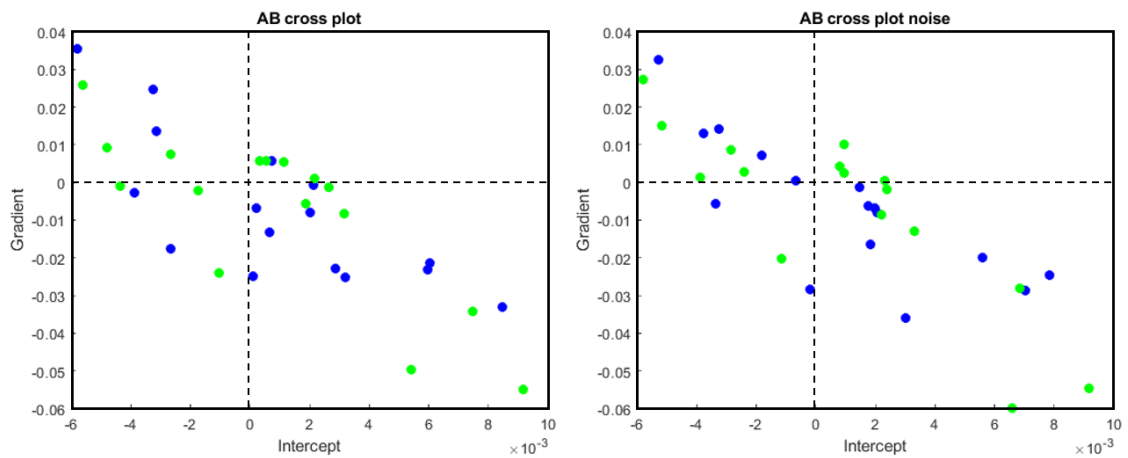

Figure 5.12: *Model 2 intercept and gradient cross-plot. Green: true AVO response. Blue: after applying Semblance. Left: noise-free. Right: white Gaussian noise.*

To further investigate the effect wrongly flattening the reflections has on the AVO response, the traces were examined. The intercept traces are shown in Figure 5.13. The two traces to the left are for the noise-free gather. True indicates the intercept from the original seismic, while post represents after the application of Semblance. There are small amplitude related differences to the intercepts, especially at $t = 2.09s$. In addition, the post trace for the noisy seismic appears to be shifted up in time compared to the true. Other than that, it is not affected much by the wrong doings of semblance. The general shape of all the traces are similar.
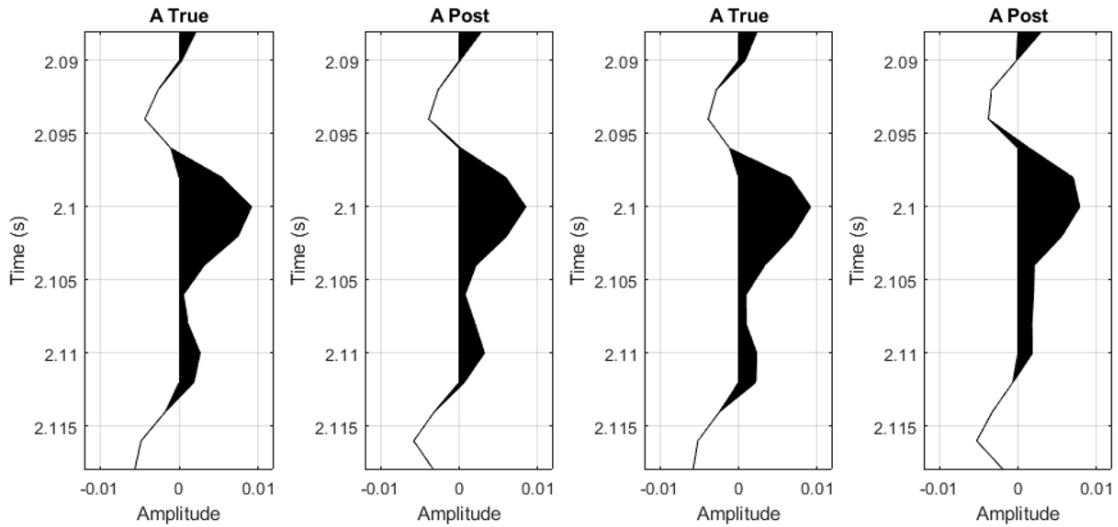

Figure 5.13: *Model 2 intercept traces: True: original gather. Post: after applying Semblance. Two to the left: noise-free. Two to the right: white Gaussian noise.*

Figure 5.14 shows the gradient traces for the true and post-Semblance gathers. There are clear differences seen in this Figure. Firstly, at $t = 2.09s$ the gradient changes from positive to negative, second the amplitudes are different throughout the entire trace. In fact, they are so different there are large changes in the general shape, especially for the traces with the presence of noise. This shows the severe impact wrongly handling of anomalies has on the gradient.
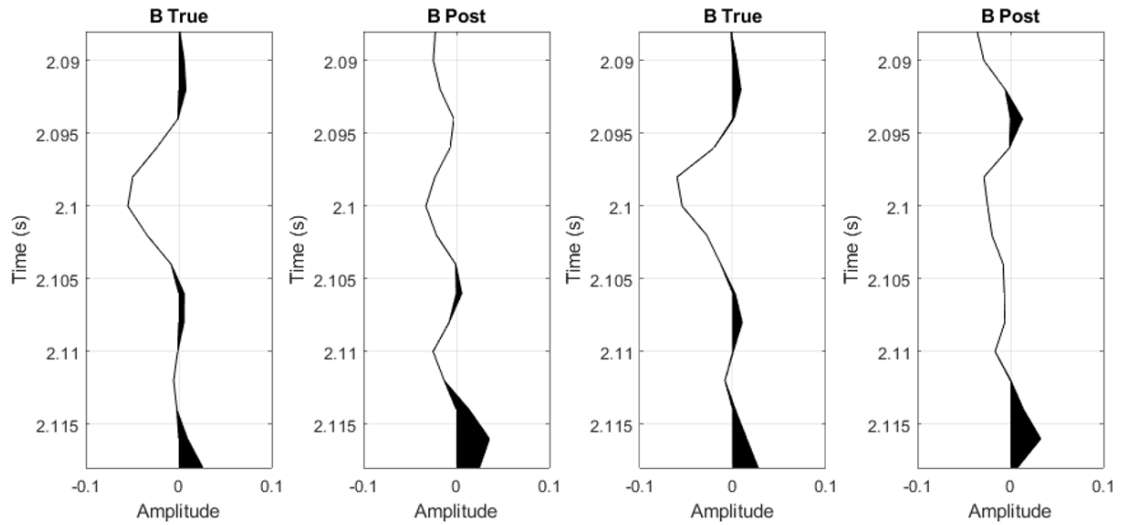
Figure 5.14: *Model 2 gradient traces: True: original gather. Post: after applying Semblance. Two to the left: noise-free. Two to the right: white Gaussian noise.*

5.3.3 Summary

The true AVO reponse was compared to the response in the presence of RMO, and after applying Semblance to correct for it, to see the difference done to the intercept and gradient. For Model 1 (the background trend), there was clear improvement in the noise-free data. The spread of the points was completely reduced, resulting in the gradient trace obtaining the correct amplitudes. The inclination of the trend the points were following was reduced, improving the vp/vs relationship. The fact that the fluid traces were zero for the true and the post-Semblance traces also proved then inclination was corrected. When noise was added to the seismic, there was not much improvement to the AVO response. The spread of the points remained unchanged, seen by the high amplitudes in the post-Semblance gradient trace. The inclination was not affected either, seen in the lack of decrease in amplitudes in the fluid trace. This is directly related to the decrease in sensitivity the method suffered from when adding noise to the seismic. It resulted in a less accurate correction, which in return did not improve the result.

For Model 2 (the anomaly) it was not easy to see the damage done by wrongly flattening the gather simply by looking at the cross plot alone. When looking at the intercept trace, there were clear amplitude differences. The gradient suffered from even more alterations, where some places it went from positive to negative. In addition, the general shape of the traces were different, especially for the noisy seismic. This erroneous response is directly linked to the methods approach to apparent residual move-out, where it seemingly flattened a reflector original intended to bend.

Chapter 6

Swans residual velocity indicator

The method of the residual velocity indicator (or RVI) is based on a methodology developed by Swan (2001), in which the sensitivity of AVO to residual move-out is exploited to obtain accurate velocities. Similarly to Semblance, the residual velocity indicator, or RVI, is directly linked to errors in the velocity model, but with increased sensitivity (Swan (2001). This chapter will present the theory derived in the paper, and explain how it was implemented to precondition the data for seismic analysis. The purpose of the implementation of this method is specifically to test the alleged enhanced sensitivity to small changes in the move-out curve denoted:

$$\Delta t = a\theta^2 + b\theta. \tag{6.1}$$

In addition to see how to see how it reacts to apparent RMO.

6.1 Theory and implementation

Time misalignment, Δt, due to velocity errors when following the assumption of hyperbolic travel times is denoted:

$$\Delta t = \sqrt{\left(\frac{x}{V + \Delta V}\right)^2 + t_0^2} - \sqrt{\left(\frac{x}{V}\right)^2 + t_0^2}, \tag{6.2}$$

where x is the offset, t_0 is the two-way travel-time, V is the velocity and ΔV is the velocity error. Following the approach derived in Swan (2001), it can be approximated by a truncated MacLaurin series,

$$\Delta t \approx \Delta V \frac{\partial(\Delta t)}{\partial(\Delta V)}\bigg|_{\Delta V = 0.} \tag{6.3}$$

Evaluating this difference at zero velocity error, the expression can be written as:

$$\Delta t \approx \frac{-x^2 \Delta V}{V^2 \sqrt{x^2 + (t_0 V)^2}} = -t_0 \sin\theta \tan\theta \frac{\Delta V}{V}. \tag{6.4}$$

43

By assuming that $\frac{\Delta V}{V}$ varies much slower than the intercept, $A(t)$, Swan derives an expression for the amplitude variation caused by the time misalignment Δt given by:

$$\Delta S = -t_0 \frac{\Delta V}{V} A'(t) \sin\theta \tan\theta, \qquad (6.5)$$

where $A'(t)$ is the time derivative of the intercept, which was explained in Chapter 3.

Analytic expressions for the intercept and gradient, denoted $A_a(t)$ and $B_a(t)$ can be obtained by adding them to i times their Hilbert transforms. By incorporating expression 6.5 into the analytical expression of the gradient, Swan derives an equation for the gradient estimated in the presence of a velocity error given:

$$B_a(t, \Delta V) = B_a(t) - t A'_a(t) \left(\frac{\Delta V}{V} \right). \qquad (6.6)$$

Using expression 6.6, and an analytic representations of the intercept and gradient, Swan derives an equation that effectively separates the velocity effects from the true AVO effects given by:

$$A_a(t) B^*(t, \Delta V) = A_a B^*(t) + i\omega_0 t \left(\frac{\Delta V}{V} \right) |A_a(t)|^2. \qquad (6.7)$$

The imaginary part of equation 6.7 is named the residual velocity indicator, RVI, while the real part of the equation is named the hydrocarbon indicator, or HCI. The velocity-error induced AVO response resides in the imaginary part, while the real AVO response is represented by the real part. This is key in implementing the method, as the goal is to minimize the RVI. It is important to note that the expression derived only experiences excellent separation between the real and velocity-error induced AVO responses when the relationship between the intercept and gradient is co-linear(Swan (2001)). Foster et al. (1993) showed that this is the case when the geology is following the background trend. For events with non-co-linear relationships between A and B, the imaginary part will also contain some of the real AVO response (Swan (2001)), which is the case for anomalies.

The method was implemented through a series of easy steps. First, the intercept and gradient were estimated at each time sample, then the RVI was calculated using equation 6.7. This was done for several a and b in $\Delta t = a\theta^2 + b\theta$ to see which values of a and b minimized the RVI.

6.2 Examples

After implementation, the method was tested on the gather following the background trend, and the gather containing the AVO class 2p. RMO defined by Figure 6.1 shows the amount that was added to Model 1. The curve is defined by the function $\Delta t = 0.02\theta^2 + 0.002\theta$. The purpose was to test the methods sensitivity to small

changes in the move-out curve, to see which values of a and b resulted in minimizing the RVI. It is important to note once again that the a and b obtained post-correction are the exact opposite of the a and b pre-correction, as this would reverse the residual move-out added.
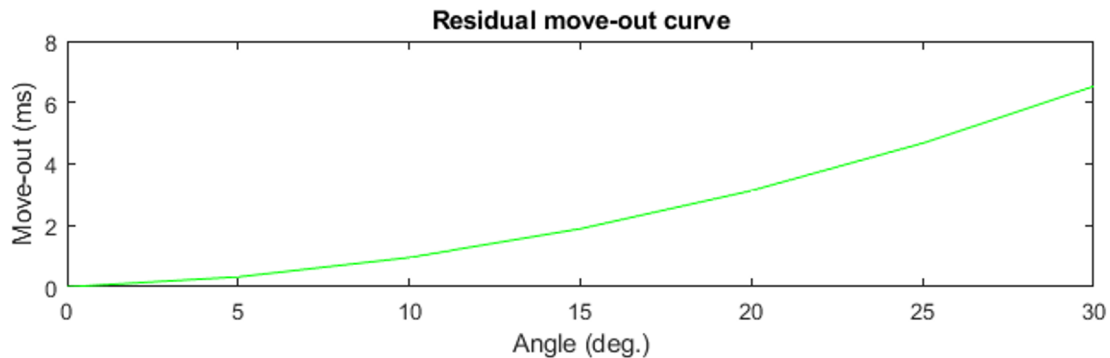

Figure 6.1: *Move-out curve showing the residual move-out added to Model 1 prior to testing the RVI.*

For Model 2, the gather containing the anomaly, a different approach was taken. No residual move-out was added to gather, as the purpose is to see whether the RVI is minimized in the presence of the apparent RMO, or when it is removed.

6.2.1 Model 1: Background trend

Figure 6.2 shows two seismic section together with the RVI. The gather on the left represents the gather obtained by adding the RMO defined in Figure 6.1, while the right gather shows the one post-correction. The middle gather shows the RVI. The top x-axis on the middle gather defines the trajectory number, while the bottom x-axis represents RMO at 30 degrees. From the Figure, the RVI is clearly minimized when Δt is zero, as it should be. This suggest that the method is indeed sensitive to the small velocity errors Semblance struggled with. The RVI-traces also appear to change phase depending on wether the RMO is positive or negative, which is very useful.
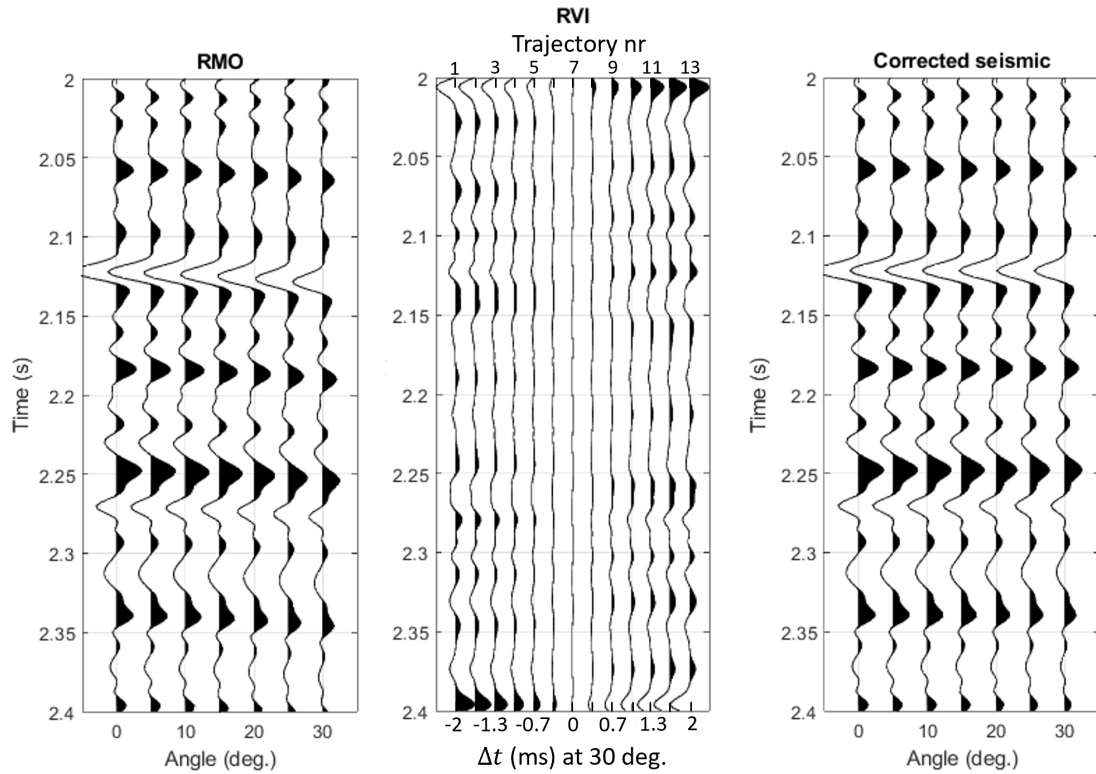
Figure 6.2: *Model 1 noise-free gathers. Left: original gather. Middle: RVI (top x-axis: trajectory number. Bottom x-axis: Δt at 30 degrees). Right: gather obtained after minimizing the RVI.*

In order to properly compare the move-out curve applied to the seismic, to the one obtained from minizming the RVI, the absolute value of both were compared in Figure 6.3. As expected, they are similar to the point of complete overlap, which is a further indication that the RVI was minimized when the RMO is completely removed.
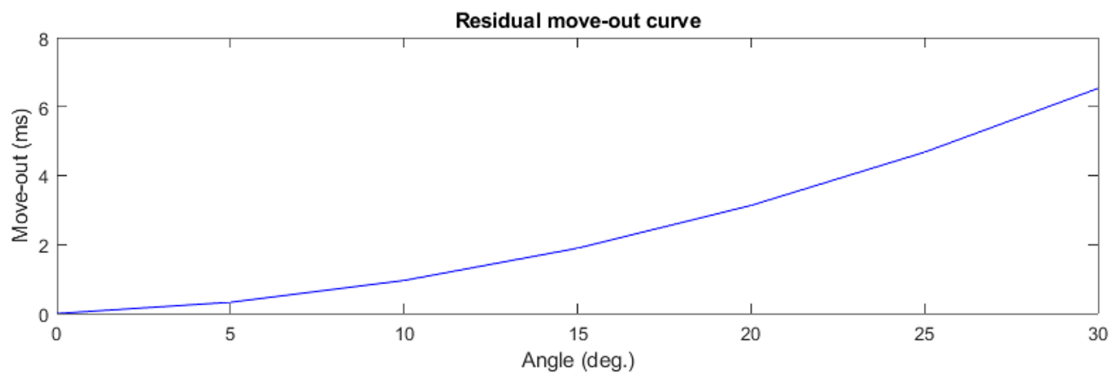
Figure 6.3: *Green: true move-out curve added prior to testing method. Blue: move-out curve obtained after minimizing RVI.*

The method was also tested on the same seismic section containing noise in Figure 6.4. However, this time the RVI is not minimized when Δt are zero at 30 degrees,

but rather when $\Delta t = 0.35$ ms. The RVI for that trajectory (nr. 6) is very similar to the true trajectory (nr 7), but it is slightly smaller. It is important to note that these are extremely small differences. Together with the results obtained on the noise-free data, this suggests there is indeed excellent separation between the real AVO response and the velocity-error induced AVO response when the seismic is completely following the background trend.
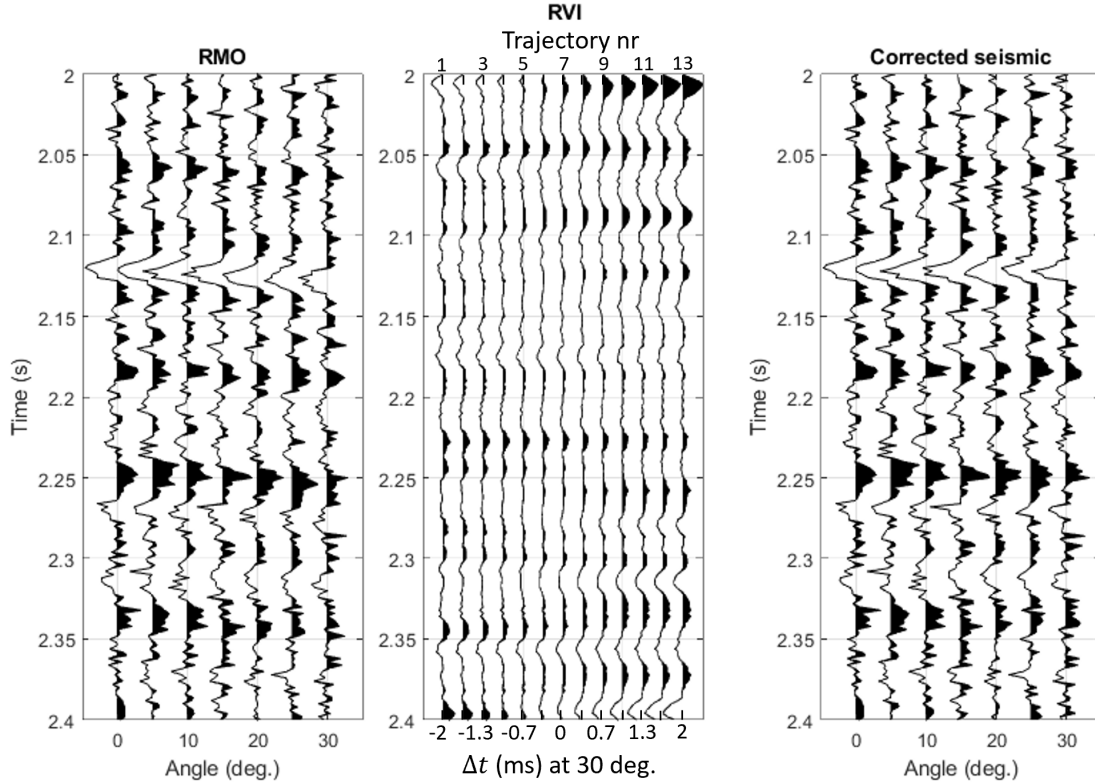

Figure 6.4: *Model 1 white Gaussian noise in gathers. Left: original gather. Middle: RVI (top x-axis: trajectory number. Bottom x-axis: Δt at 30 degrees) Right: gather obtained after minimizing the RVI.*

Figure 6.5 shows the real move-out curve in green and the one obtained by minimizing the RVI in blue. The difference between them increases with angle, but even at the highest angle it is still way less than half a sample, suggesting that the decrease in sensitivity in the presence of noise is minimal.
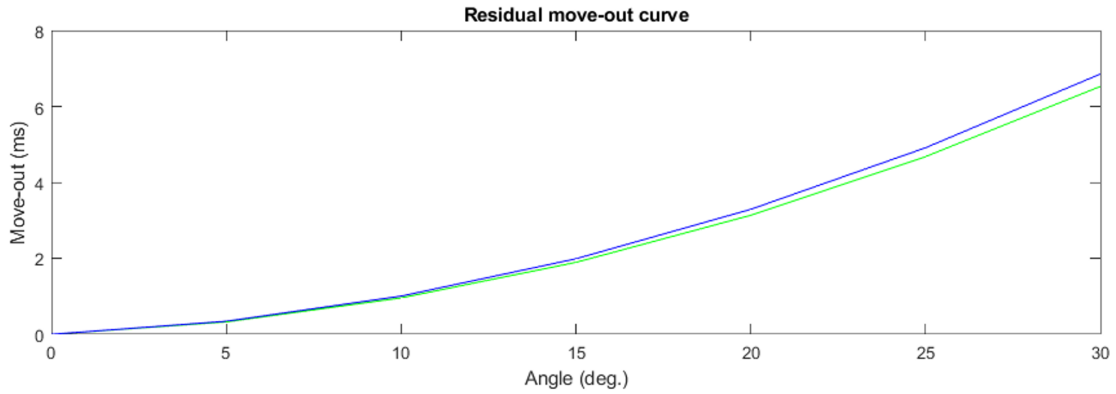
Figure 6.5: *Green: true move-out curve added prior to testing method. Blue: move-out curve obtained after minimizing RVI.*

6.2.2 Model 2: Class 2p anomaly

The main purpose of testing the method on a seismic section containing an anomaly, was to see how it reacts to apparent RMO. Keep in mind that there was not added any RMO to the data in this example. Figure 6.6 shows the original seismic, the RVI and the seismic obtained by using the minimized RVI. By looking at the middle gather it is quite clear that trajectory nr. 10 minimized the RVI. The corresponding seismic does not seem to make much sense. All the traces have been moved way down.
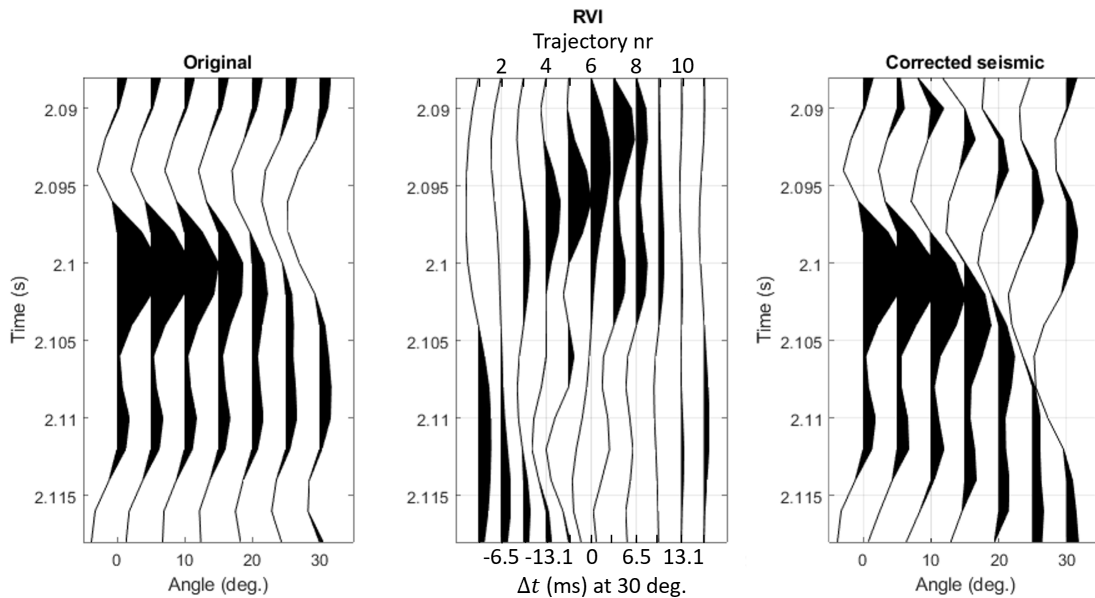

Figure 6.6: *Noise-free Model 2. Left: original gather. Middle: RVI. Top x-axis: trajectory number. Bottom x-axis: Δt at 30 degrees. Right: result after minimizing the RVI.*

Figure 6.7 shows the same scenario for seismic with white Gaussian noise. The RVI

clearly minimized for trajectory 10 or 11, it does not make much difference as both of them are quite wrong either way. Again, the method seems to have moved all the traces further down.
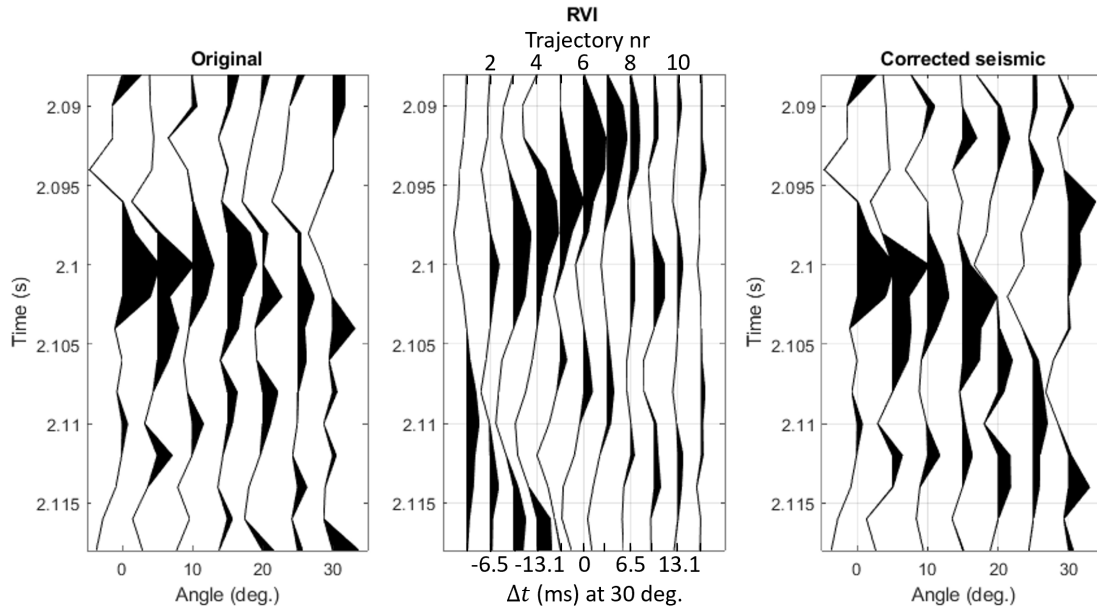

Figure 6.7: *Model 2 with white Gaussian noise. Left: original gather. Middle: RVI (top x-axis: trajectory number. Bottom x-axis: Δt at 30 degrees). Right: result after minimizing the RVI.*

6.2.3 Discussion

The method of RVI was implemented to test the enhanced sensitivity to small changes in the move-out curves, and to see how it handled apparent RMO. The results on Model 1 clearly showed that the method is sensitive to even the smallest changes to a and b, which is necessary before performing AVO analysis. In addition, the phase of the RVI-traces provide information on wether the user is over- or under-correcting. On the other hand, Model 2 showed undesirable results due to containing an anomaly. Like any other method, it has it weaknesses, and these lie within the assumptions made in order for the RVI to act desirably. As previously explained, the reason for the wrongly handling of model 2 is due to the non-co-linear relation-ship between intercept and gradient for the anomaly. Other important assumptions made are: constant velocity and consistent AVO behaviour in the analysis window, and short offset approximation for move-out and AVO analysis. These assumptions are often invalid in real data, which adds instability to the iteration process (Rat-cliffe & Roberts (2003)). Lastly, it is important to note that relating the derivative of the zero-offset trace to the gradient is only valid for small move-out errors.

It is important to note that my approach to implementing this method is not the optimal approach when dealing with an entire seismic cube. First, the calculation of the RVI can be automated by using efficient gradient based iterative methods. Second, due to noise and other ambiguities in the seismic, the RVI should not be

local, but rather averaged over 2D or 3D windows surrounding each analysis points (the interested reader is referred to (Swan (2001) for details).

6.3   AVO Analysis

To determine how the benefits of the RVI's enhanced sensitivity to small changes in the move-out curve, the AVO response was examined. The intercept and gradient was estimated for both models, along with the fluid trace for Model 1.

6.3.1   Model 1: Background trend example

Figure 6.8 shows the intercept and gradient cross plots for Model 1. The true response is represented by the green points, while the blue points show the response acquired after minimizing the RVI. The red points represent the response after adding RMO. The left side is for the noise-free data, and the right side is in the presence of noise. As seen in the Figure, the difference in the AVO responses for the noise-free data are huge. Firstly, the spread is completely reduced, resulting in accurate estimations of the gradient. Second, the inclination of the trend the points are following is flattened appropriately. In fact, the true AVO response completely overlaps with the post-correction response, which explains why the blue points are not visible on the left side of the figure. When noise was present, the RVI was not minimized when it should have, resulting in an erroneous AVO response. The spread of the points seems to barely be reduced, neither is the inclination.
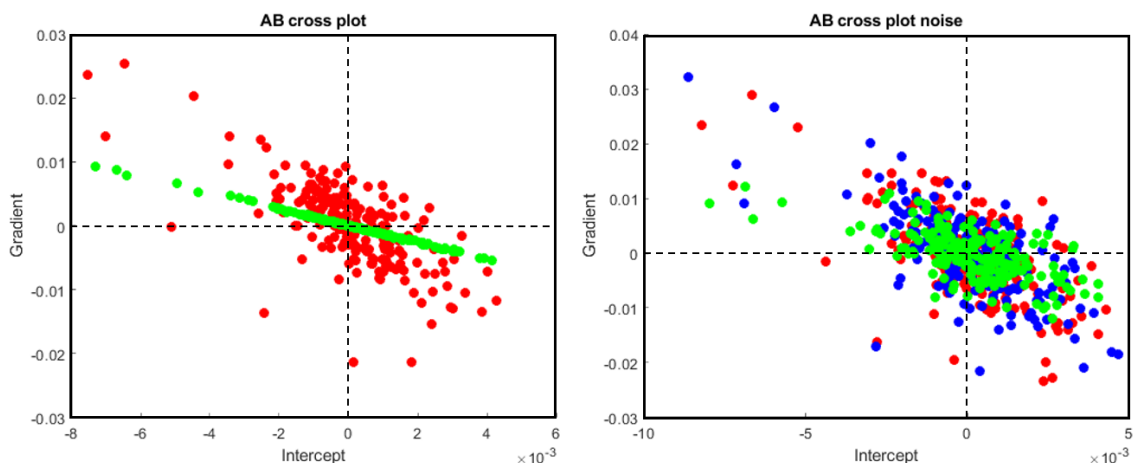

Figure 6.8: *Model 1 intercept and gradient cross plot. Green: original response. Blue: after minimizing RVI. Red: after adding RMO. Left: noise-free. Right: white Gaussian noise.*

Figure 6.9 shows the true, pre and post intercept traces. Pre represents the intercept obtained after adding RMO to the data, while post is after minimizing the RVI. As

there was not done much difference to the intercept, all traces are near-identical. By looking closely, one can observe small amplitude differences between the pre and post results for the noise-free seismic.
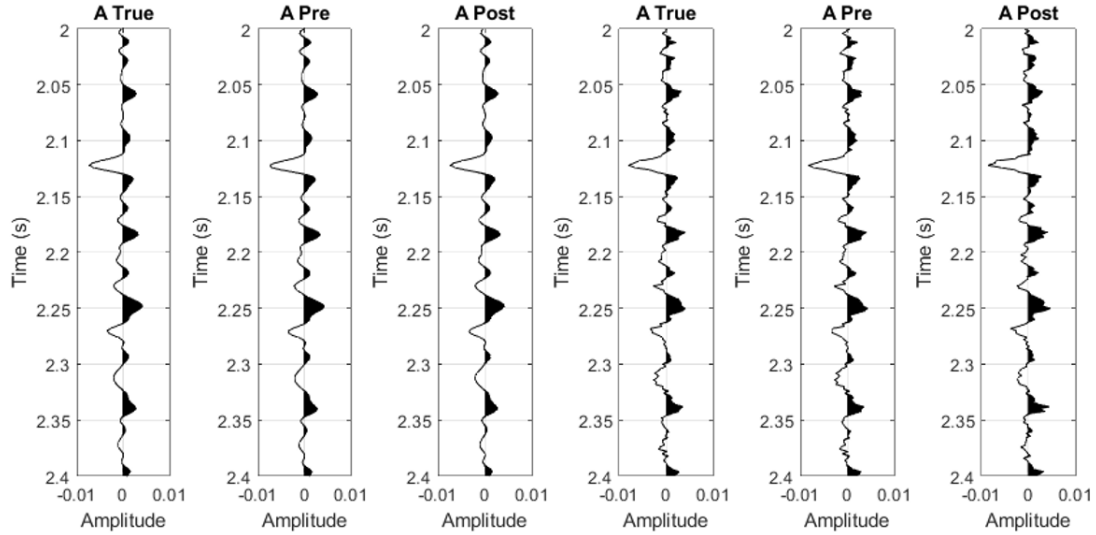

Figure 6.9: *Model 1 intercept traces. True: original seismic. Pre: after adding RMO. Post: after minimizing RVI. Three to the left: noise free. Three to the right: white Gaussian noise.*

Figure 6.10 shows the same, but for the gradient. For the noise-free seismic (three to the left) the true gradient is identical to the post gradient. For the noisy seismic the case is different. As the method did not completely flatten the gather, the post gradient trace experience too large amplitudes. This observation shows the difference even the tiniest amount of residual move-out makes on the AVO response.
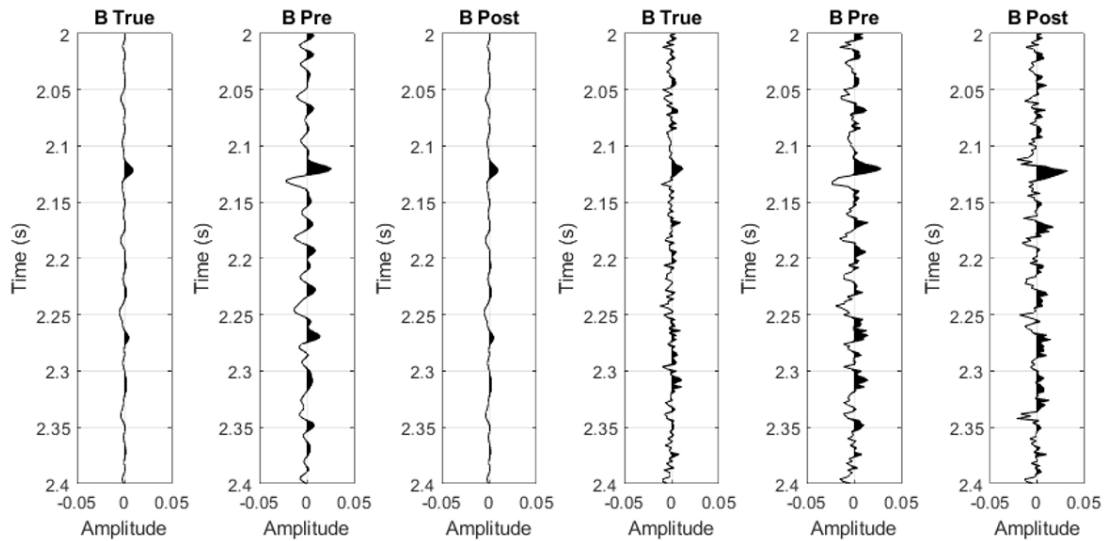

Figure 6.10: *Model 1 gradient traces. True: original seismic. Pre: after adding RMO. Post: after minimizing RVI. Three to the left: noise free. Three to the right: white Gaussian noise.*

To further investigate how the AVO response was affected, the coordinate system was rotated to obtain the fluid traces seen in Figure 6.11. For the noise-free seismic the true fluid trace is completely identical to the post-Swan fluid trace. They are near-zero which is the correct response as the seismic section is completely brine-filled. For the gather contaminated with white noise, the method did not completely remove the RMO, resulting in the post-Swan fluid trace to have much larger amplitudes than the true trace. This is further evidence the inclination of the trend was not corrected.
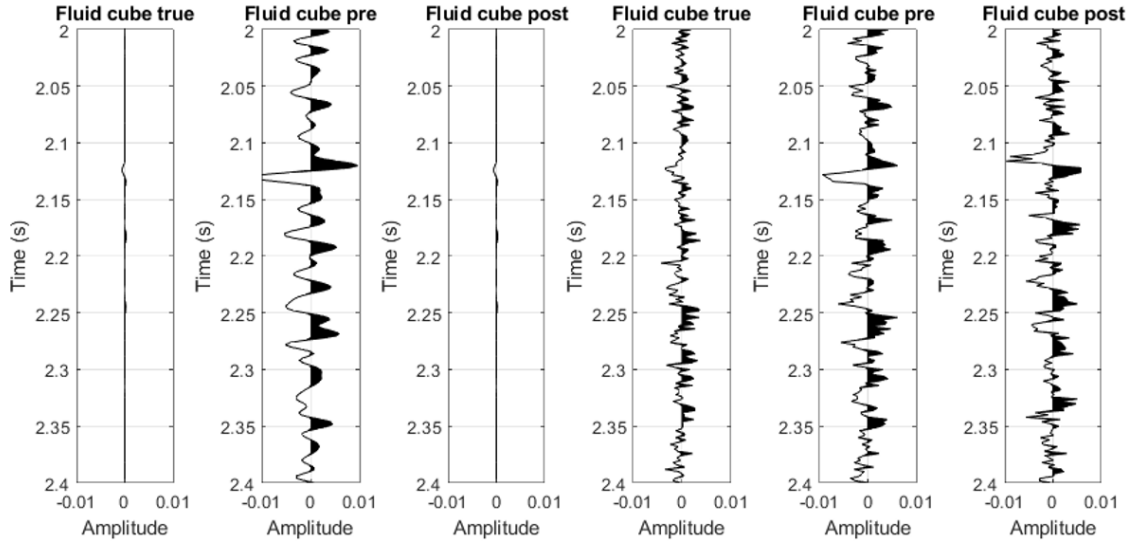

Figure 6.11: *Model 1 fluid traces. True: original seismic. Pre: after adding RMO. Post: after minimizing RVI. Three to the left: noise free. Three to the right: white Gaussian noise.*

6.3.2   Model 2: Class 2p anomaly

Figure 6.12 shows the AVO response for the Class 2p anomaly. The green points represent the true response, and the blue points shows the post-Swan response. The first observation in the noise-free case is that the post-Swan AVO response in blue seems to follow a linear line. This is a very interesting observation, as the method assumes co-linear relationship between the intercept and gradient. The fact that the RVI was minimized for this Δt suddenly make sense, as correcting the gather with the corresponding a and b resulted in a co-linear relationship between intercept and gradient. For the gather filled with white noise, the case is very much the same, but not as clear due to the noise.
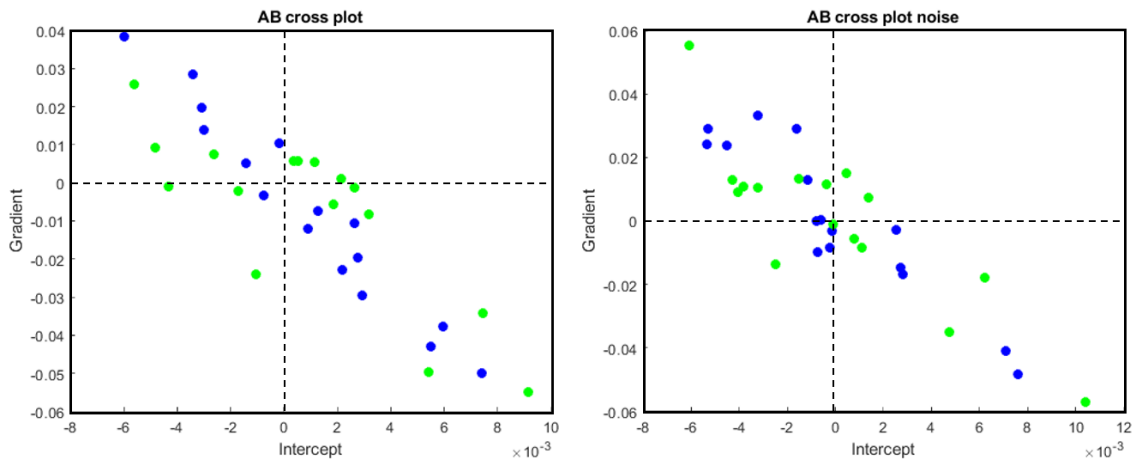
Figure 6.12: *Model 2 intercept and gradient cross plot. Green: true AVO response. Blue: after minimizing RVI. Left: noise-free gather. Right: white Gaussian noise.*

Considering Model 2 is so small, it might be hard to examine the AVO response by examining a few points in the cross-plot. To get a broader idea of how it was affected, the intercept traces are seen in Figure 6.14. There is not much difference between the traces for the noise-free case, except for a change from positive to negative amplitude slightly above $t = 2.09$ s, and amplitude differences between $t = 2.105$ s and 2.11 s. Despite these changes, the general shape of the traces are fairly similar.

When the noise is present the difference is quite obvious. Firstly, at $t = 2.09$ s the amplitude for the post-Swan intercept is negative, while the true is positive. There are also significant amplitude differences between $t = 2.105$ s and $t = 2.115$ s. In addition, the general shapes of the traces are very different.
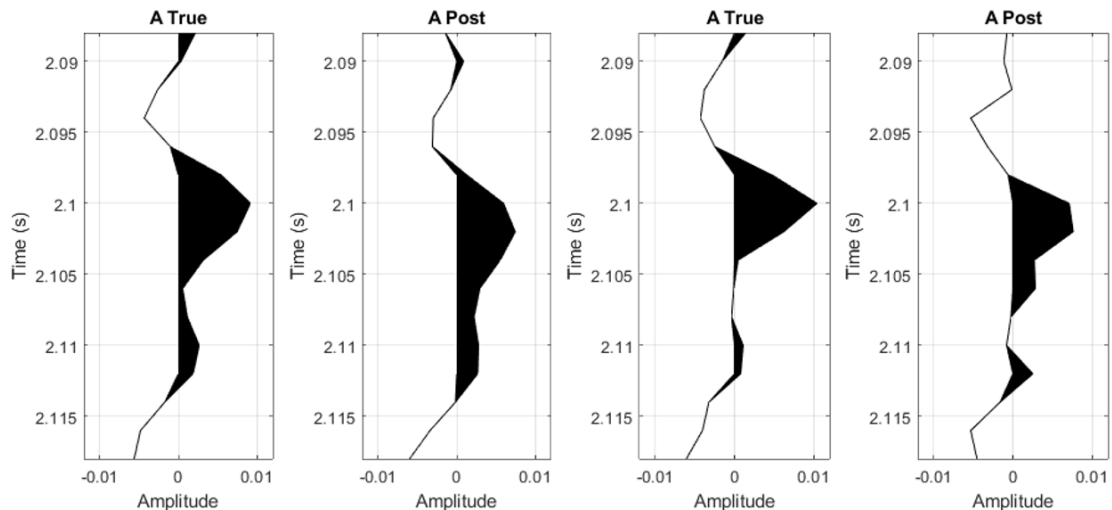

Figure 6.13: *Model 2 intercept. True: original gather. Post: after minimizing RVI. Two the left: without noise. Two to the right: white Gaussian noise.*

53

Figure 6.14 shows the true and post-Swan gradient. The difference in the traces are huge both for the noise-free and the noisy seismic. For the noise-free case, the amplitudes over the entire trace are very different, indicating the changes done to the seismic were so significant the traces do not even resemble each other. In the interval $t = 2.09$ s to $t = 2.095$ s and $t = 2.105$ s to $t = 2.11$ s, the gradient changes sign.

When the noise is present the difference is even larger, especially in between $t = 2.105$ s and $t = 2.11$ s, where the amplitude is changed from positive to negative in the entire interval. There are other severe changes to the gradient at $t = 2.095$:s too. Overall the traces for both noisy and noise-free seismic are altered to the point of complete change in both amplitudes and general shape.
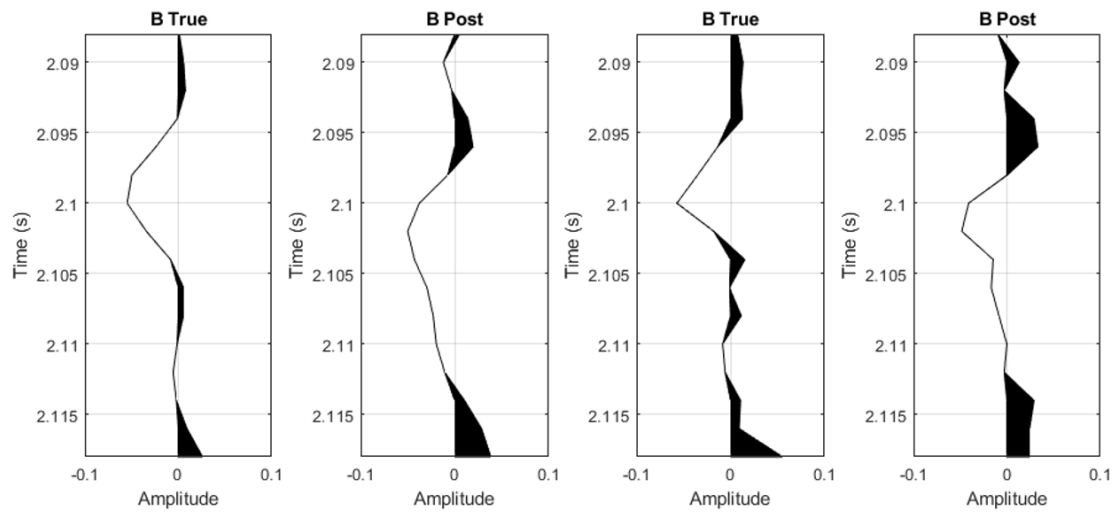

Figure 6.14: *Model 2 gradient traces. True: original gather. Post: after minimizing RVI. Two the left: without noise. Two to the right: white Gaussian noise.*

6.3.3   Summary

The intercept and gradient were estimated for both models, using the method of minimizing the residual velocity indicator. The RVI's sensitivity to velocity errors is large enough to completely remove RMO for the noise-free gather following the background trend, which results in a huge decrease in the spread and correct gradient amplitudes. In addition, the inclination of the trend the points are following becomes correct, as seen by rotating to achieve the fluid cube. When noise was present for the seismic following the background trend, it did not completely remove the residual move-out, but did a very good job. However, the resulting AVO response did not improve much, the gradient trace with RMO was fairly similar to the one post-Swan, and experienced larger amplitudes than the true. When rotating the cube to obtain the fluid traces, it was nowhere close to zero either.

The AVO response for Model 2 experienced heavy changes by minimizing the RVI.

The most interesting observation was seeing the near-perfect linear trend the points followed post-Swan, as a direct result to the RVI being minimized when the intercept and gradient are co-linear. Due to AVO reponse being altered in that degree, both the gradient and intercept went from being positive to negative in some places. In other words, the AVO response was completely altered to not even resembling the true. This is further evidence the user should avoid known anomalies when applying this method.

Chapter 7

Cross Correlation

Similarly to Semblance, Cross correlation is also a measure of coherence. Unlike Semblance, it is neither directly linked to the velocity, nor used during processing. It is considered a time-domain operation that is used to measure the similarity between two signals, as a function of displacement relative to each other in time. As RMO leads to misalignment between two traces as a function of time, it proves to be useful in correcting for it. This chapter will review the accuracy and usefulness of cross correlation as a method to precondition the data for seismic analysis. A method will be implemented and tested on the seismic sections described in Chapter 4. The AVO response will then be analysed to determine the usefulness.

7.1   Theory and implementation

The general formula for cross correlation is given by:

$$C_{xy} = \int x(\tau)y(t + \tau)d\tau, \qquad (7.1)$$

where $x(\tau)$ and $y(\tau)$ are the functions being compared at the lag τ . As a simple example consider two identical functions, one of which is moved in time as visualized by Figure 7.1. Cross correlation can be used to find the time-difference, Δt. It moves the function y along the time-axis, with a step-size equal to the sampling rate, to calculate the integral of their product at each lag. One lag corresponds to one sample. The integral is maximized when the functions are perfectly aligned.
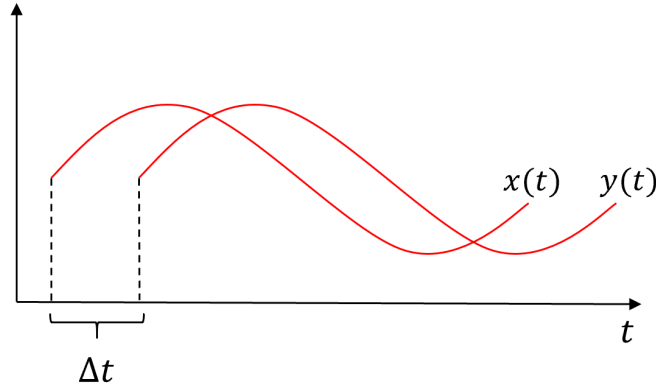
Figure 7.1: *Visualization of two similar functions displaced relative to each other in time.*

This can be applied to seismic to tackle the problem of residual move-out. As it is only possible to cross correlate two and two traces, the optimal application is to cross correlate the near and far trace. The approach consists of calculating the correlation functions of the near and far trace, $C_{f,n}$. Our goals is to find the difference in time that maximizes $C_{f,n}$. We denote

$$\Delta T = \operatorname*{argmax}_{t}[C_{f,n}(t)], \tag{7.2}$$

We time-shift the trace by ΔT to get the trace corrected for residual move-out given by

$$d(t) = f(t + \Delta T). \tag{7.3}$$

Cross-correlation can also be done in the fourier domain, where cross correlation is the same as multiplying with the complex conjugate,

$$C_{xy}(t) \leftrightarrow X^*(\omega)Y(\omega) = A_x(\omega)A_y(\omega)\exp[-i(\theta_x(\omega) - \theta_y(\omega))]. \tag{7.4}$$

The phase spectrum obtained is the difference between the phase-spectrums of the two traces that have been cross correlated. Considering a time-shift in the time domain is the same as a linear phase-shift in the fourier domain (Yilmaz (2001)), this difference can be used to correct for residual move-out. In order for this to work, the amplitude spectrum has to be remained unchanged, and one has to separate the changes in the phase spectrum that are constant and linear. However, in real life it is probably far to complicated, as both the amplitude and phase spectrum are affected by so many variables. For that reason, a time-domain cross-correlation was implemented to remove the linear phase shift. If we consider the time-corrected far trace by expression 7.3, we can define the corrected cross-correlation function as:

$$C_{d,n}(t) = c_{f,n}(t + \Delta T). \tag{7.5}$$

Since time-shift is a linear phase shift,

$$C_{d,n}(\omega) = \exp[i\omega\Delta T]C_{f,n}(\omega), \tag{7.6}$$

we have successfully removed the linear phase,

$$\theta_{c_{d,n}} = \theta_{c_{f,n}}(\omega) + \omega\Delta T. \tag{7.7}$$

7.2   Examples

We consider the residual move-out to be present, but the source to be irrelevant. Following this assumption, residual move-out described in Chapter 4 was added to the seismic in the form:

$$\Delta t(\theta) = 0.02\theta^2 + 0.002\theta. \qquad (7.8)$$

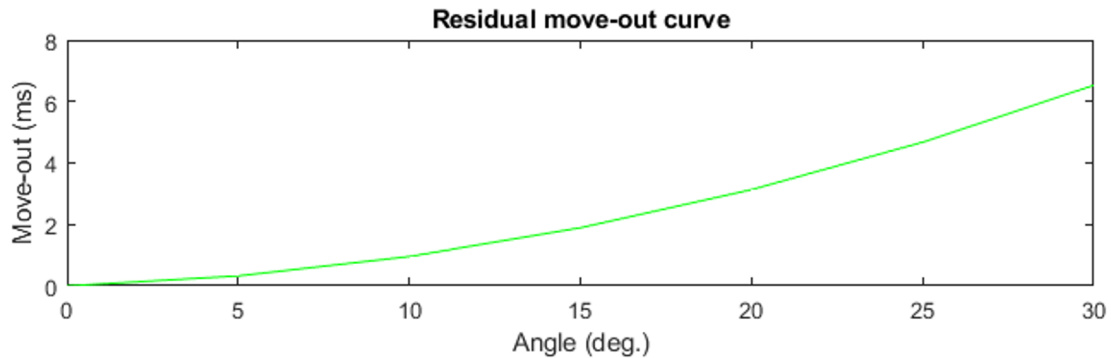The resulting move-out curve is seen in Figure 7.2.

Figure 7.2: *Model 1 move-out curve describing the residual move-out added to the data prior to testing cross correlation.*

The second gather which contains the anomaly was kept unchanged, to see how Cross correlation reacts to apparent RMO.

7.2.1   Model 1: Background trend example

As mentioned, the cross correlation was only applied on the near and far traces. In the context of correcting for residual move-out for Model 1, the near is represented by the zero-offset trace, while the far is the trace at 30 degrees. Figure 7.3 shows the near and far traces for the original seismic (left), the one altered by adding residual move-out (middle), and the one post-correction (right). The Cross correlation appears to correct the seismic appropriately, and removes RMO as intended.
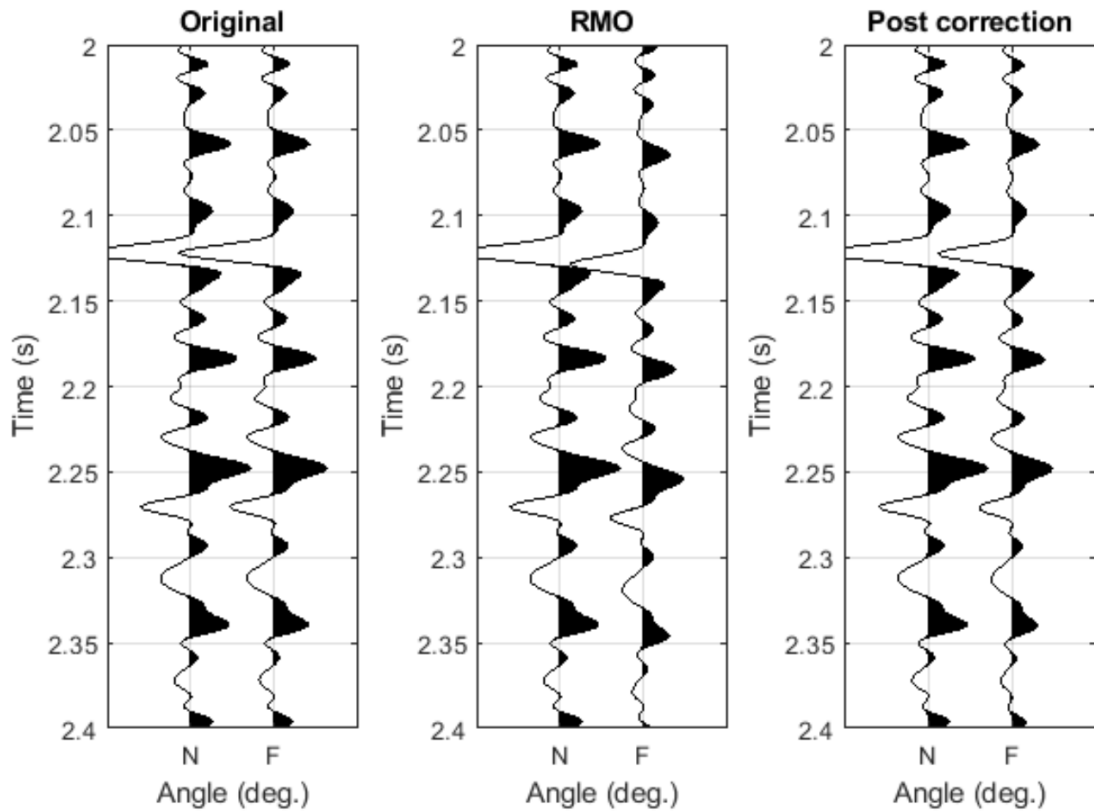
Figure 7.3: *Model 1 noise-free. Left: Original gather. Middle: after adding RMO. Right: after cross correlation.*

The correlation function in Figure 7.4 shows the correlation value at each lag. The integral of the product between the traces is clearly maximized at lag -3, meaning the far trace should be shifted -6 ms to remove the residual move-out. The results by applying this time shift is visualized in the gather to the right in Figure 7.3.
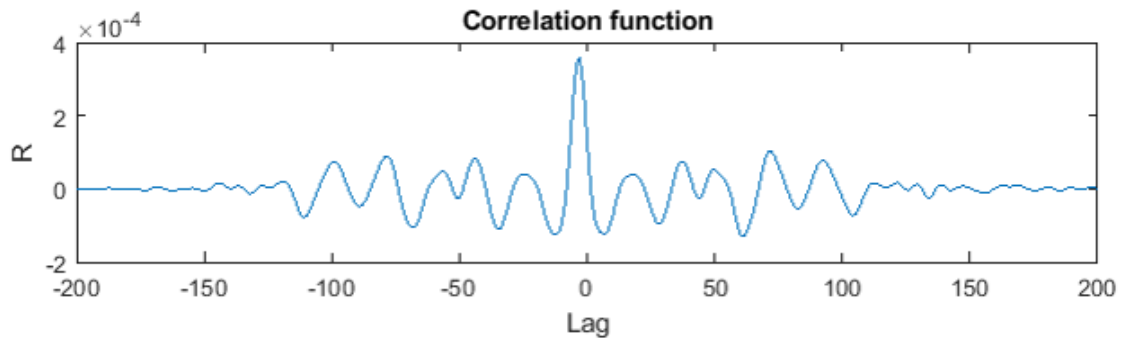

Figure 7.4: *Model 1 noise-free correlation function.*

The method was also tested on a seismic section with the presence of white Gaussian noise. Again, the post-correction gather greatly resembles the original gather.
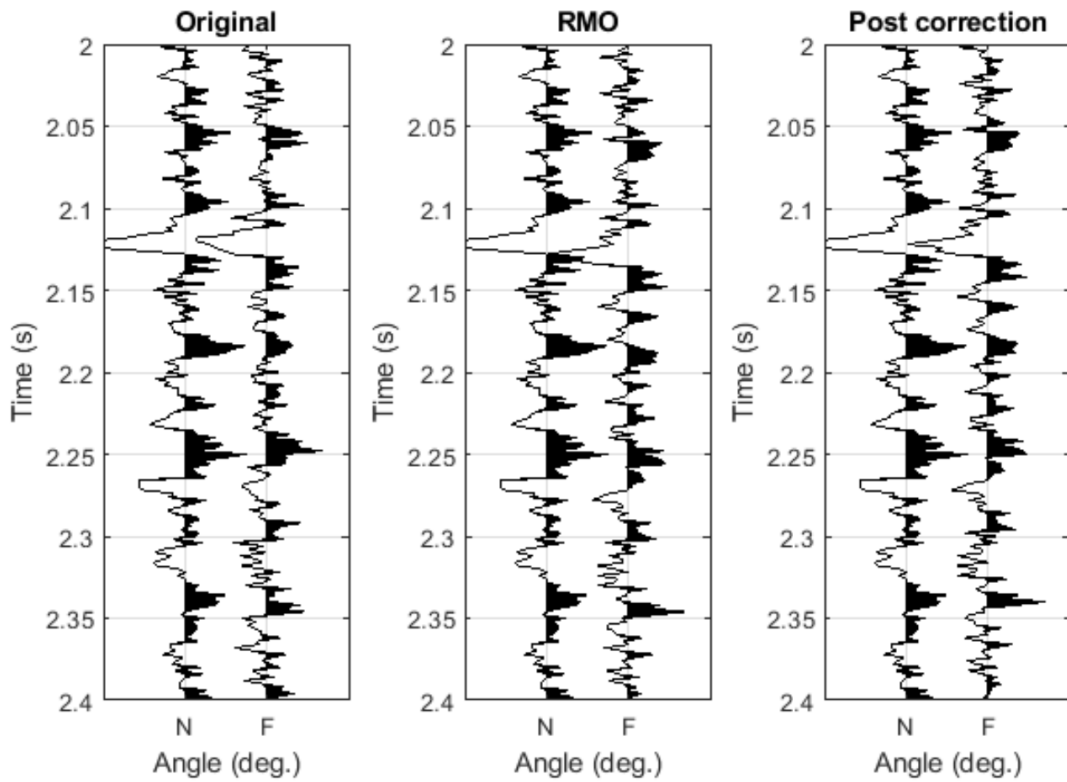
Figure 7.5: *Model 1 with white Gaussian noise. Left: Original gather. Middle: after adding RMO. Right: after cross correlation.*

The correlation function when noise is present can be seen in Figure 7.6. It is nearly identical to the one without noise, except some slight distortions. Nonetheless, the peak is located at the exact same lag, meaning the corrected gather was obtained by shifting the trace -6 ms in time.
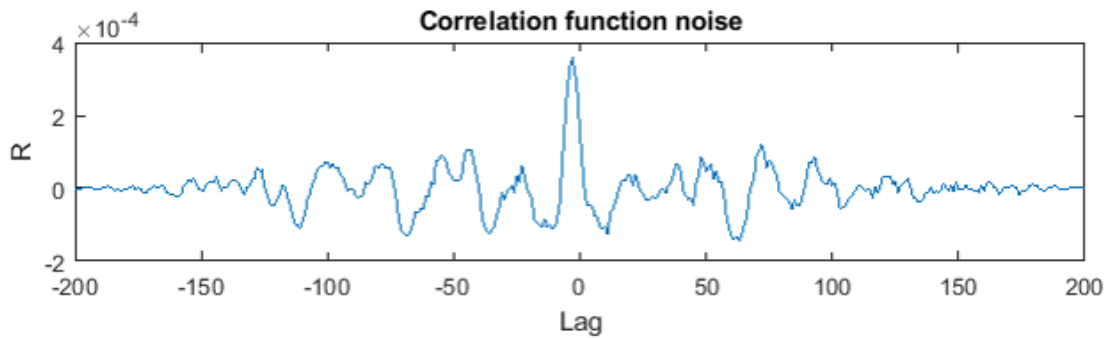

Figure 7.6: *Model 1 with white Gaussian noise correlation function.*

7.2.2 Model 2: Class 2p anomaly

Figure 7.7 shows the near and far traces of the original seismic, and the one after cross correlation was applied. Keep in mind that no RMO was added to this model. The far trace seems to be shifted up, as a result the reflections appear to align in time. In other words, the gather is flattened, and the apparent RMO is wrongly handled.
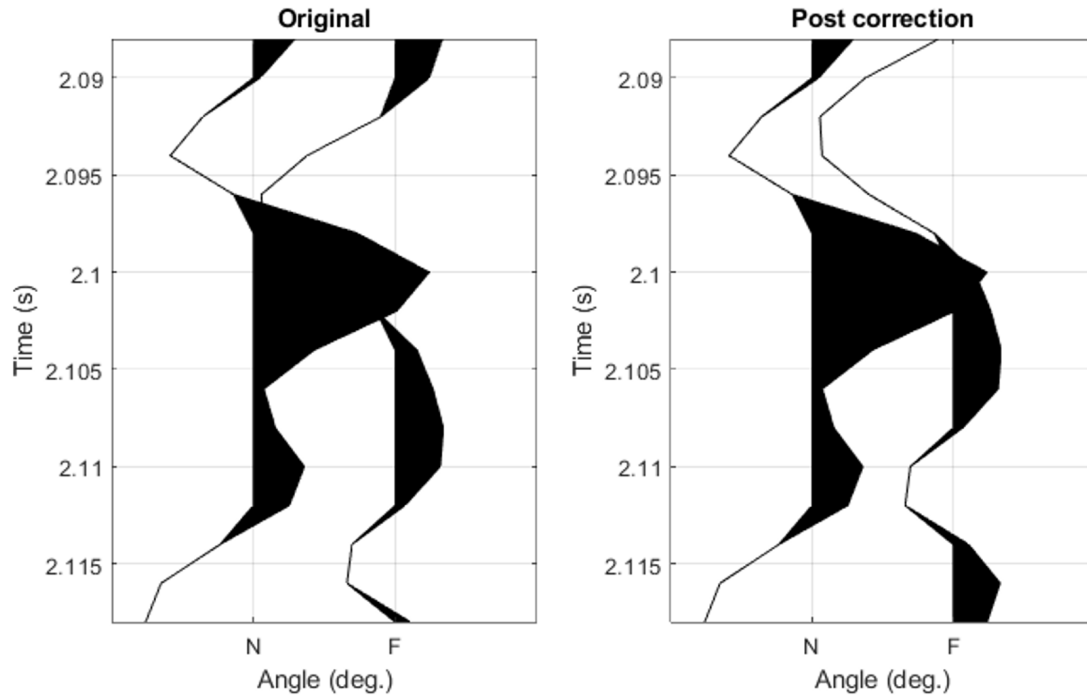

Figure 7.7: *Model 2 without noise. Left: original gather. Right: after cross correlation.*

The correlation function in Figure 7.8 behaves oddly compared to Model 1. The peak is located at lag -10, meaning the seismic was shifted -20 ms in order to obtain the corrected gather. Applying said time-shift in return wrongly flattened the gather. It is important to note the second positive peak at lag +3, meaning a time-shift of +6 ms would also result in a large integral of their product. However, shifting the seismic with +6 ms would result in an erroneous gather too.
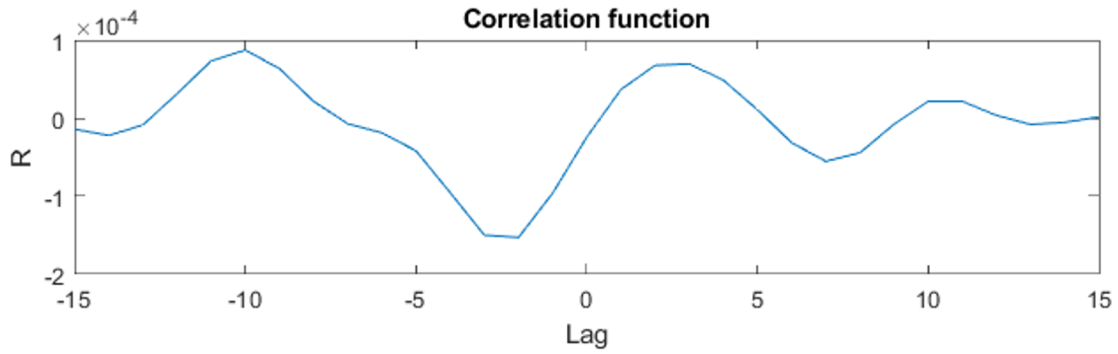
Figure 7.8: *Model 2 noise-free correlation function.*

The method was also applied on noisy seismic seen in Figure 7.9. As expected, the result is the same. The far trace has been moved making the reflections align.
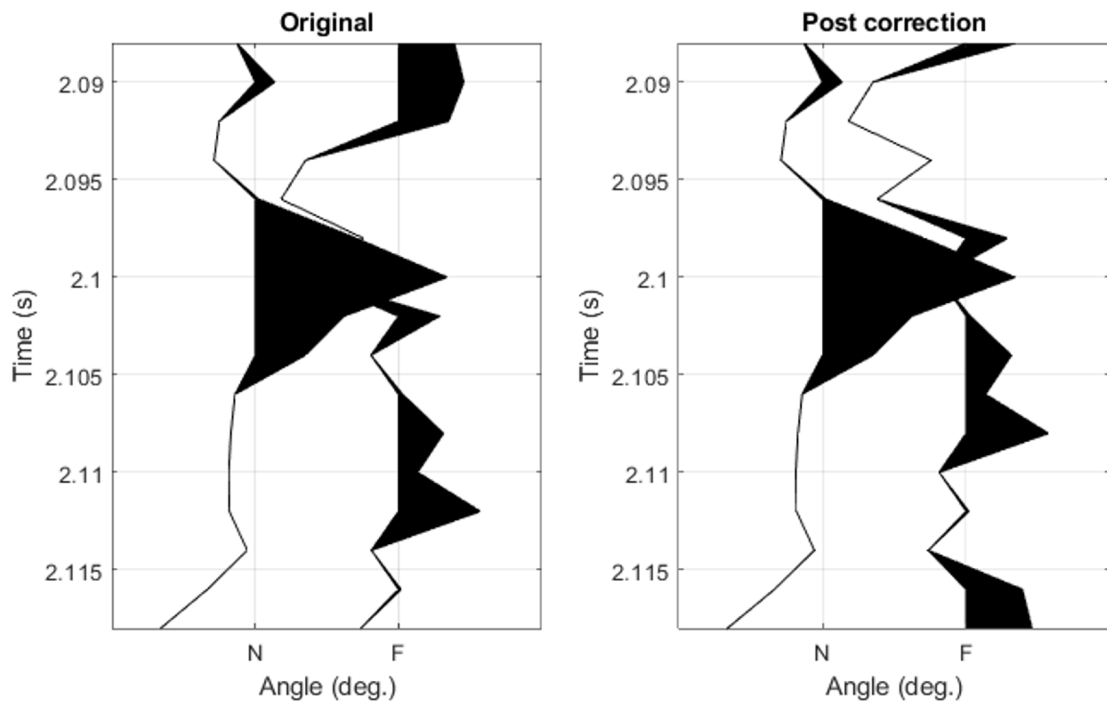

Figure 7.9: *Model 2 with white Gaussian noise. Left: Original gather. Right: after cross correlation.*

The correlation function for the noisy seismic can be seen in Figure 7.10. The correlation function shows two peaks, at plus and minus 5 lags, meaning the integral of their product is maximized by shifting the far trace either up or down 10ms. Either time shift would result in a highly erroneous result.
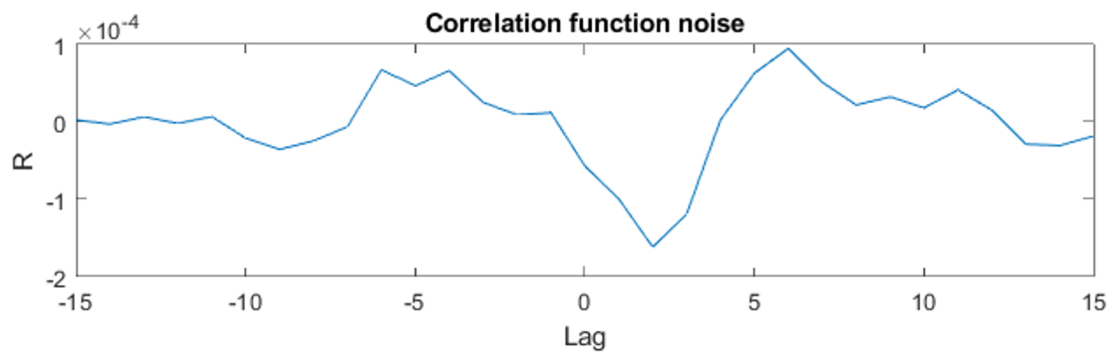
Figure 7.10: *Model 2 with white Gaussian noise correlation function.*

7.2.3 Discussion

There are several strengths and weaknesses to using cross correlation to correct for RMO. On Model 1 it did an outstanding job, but Model 2 was completely wrongly handled. Partly due to the dissimilarity between the near and the far, but mainly because off the apparent RMO. As cross correlation is a measure of similarity, the difference between the near and far for Model 2 makes the method struggle to work the way intended. Generally speaking, one way to make sure near and far traces are as similar as possible prior to using cross correlation, is to match the frequency bandwidth. That way, any differences in resolution causing the difference between the traces is removed. In the example of Model 2, the near and far traces are different to reasons beyond the frequency spectrum, so it would not make much difference in a real-data example of the anomaly either.

Another weakness to cross correlation in the time-domain is the lack of accuracy for sub-sample residual move-out. Normally, this can be easily accounted for by simply re-sampling the data, or by interpolation, but it was not done here. However, whether this is done or not, the method implemented is still a static RMO corrector. But, there exists approaches to a dynamic approach too, which will be discussed in Chapter 9.

Overall, it is an effective measure of similarity which is very useful to remove the RMO in instances where the seismic optimally should be flattened (Model 1). It is robust, works just as well even with the presence of noise.

7.3 AVO Analysis

As the purpose of this thesis is to examine the usefulness of different methods as a means to precondition the data for seismic analysis, the AVO responses were examined.

7.3.1 Model 1: Background trend example

Figure 7.11 shows an intercept and gradient cross plot for the seismic following the background trend, both with (right) and without (left) noise. The green points represent the true AVO response, the blue points are showing after the use of cross correlation to correct for it, and finally the red points are with the residual move-out present. The first observation from the plot from the seismic section without noise is the decrease in spread after the seismic is corrected using cross correlation. However, the decreased accuracy related to the sampling rate makes it imperfect. The spread is decreased a lot, but the inclination of the blue points is too steep, suggesting the vp/vs will be slightly wrong. The difference is harder to see at first sight when the noise is present, but the inclination of the true and corrected seismic have a slightly flatter inclination than the seismic with RMO. The spread is similar though.
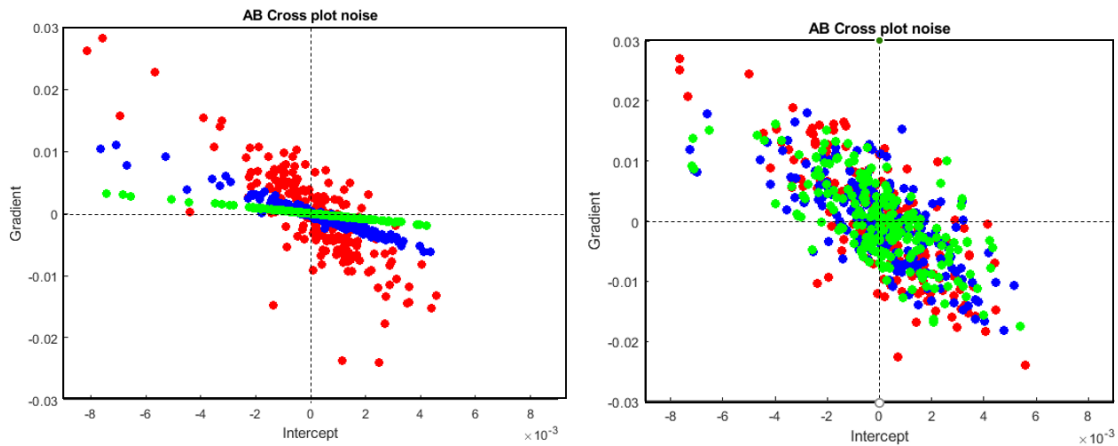

Figure 7.11: *Model 1 intercept and gradient cross plot. Green: true AVO response. Blue: after cross correlation. Red: after adding RMO. Left: without noise. right: white Gaussian noise.*

The intercept traces for the true response, the response with RMO and after cross correlation are all in Figure 7.12. Considering the small changes done to the intercept by the small move-out, it is expected that they are all very similar. There are slight differences in the amplitude in the pre intercept compared to the others, but it is small.
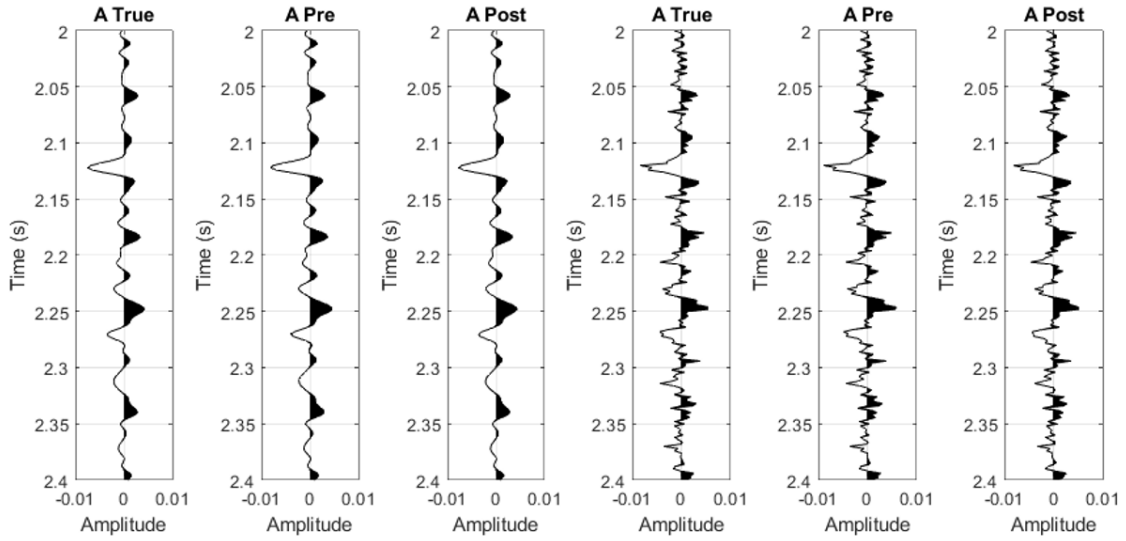
Figure 7.12: *Model 1 intercept traces. True: original seismic. Pre: after adding RMO. Post: after cross correlation. Three to the left: without noise. Three to the right: white Gaussian noise.*

The gradient however, shows larger differences as seen in Figure 7.13. The amplitudes in the true gradient are sufficiently smaller than the pre response. The gradient acquired after correcting the seismic shows great reduction in amplitudes, but it is not perfect. The amplitude differences is again related to the implementation of the method, where sub-sample move-out is not removed by interpolation or re-sampling.
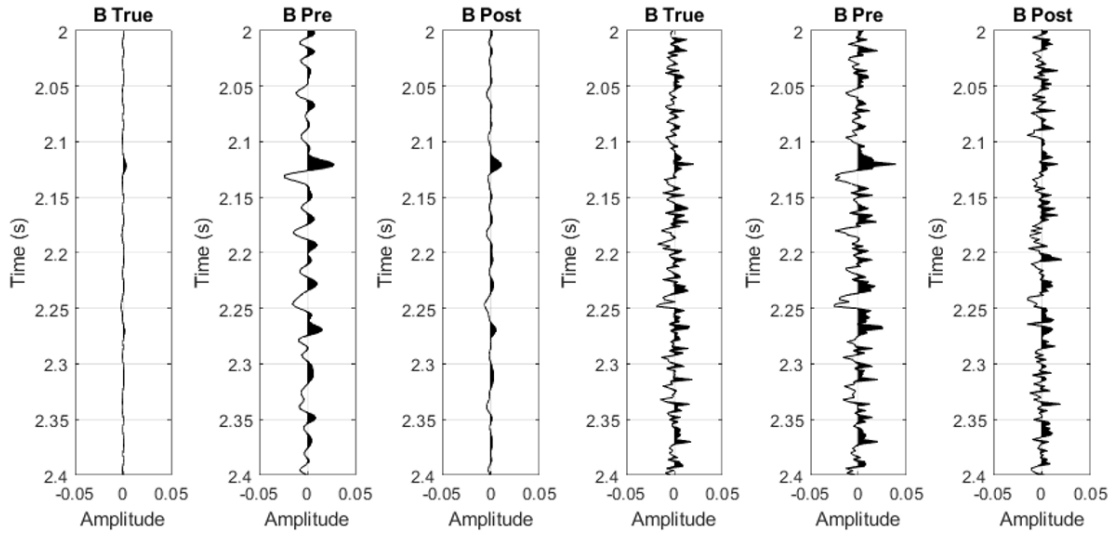

Figure 7.13: *Model 1 gradient traces. True: original seismic. Pre: after adding RMO. Post: after cross correlation. Three to the left: without noise. Three to the right: white Gaussian noise.*

Figure 7.14 shows the fluid traces obtained by rotating the coordinate system. The figure clearly shows the fluid traces is near-zero for the true and post-correction

65

AVO reponses for the noise-free case. This shows the importance of the job done by cross correlating the traces in this instance. However, in the presence of noise, the post-correction fluid trace is not reduced in amplitudes.
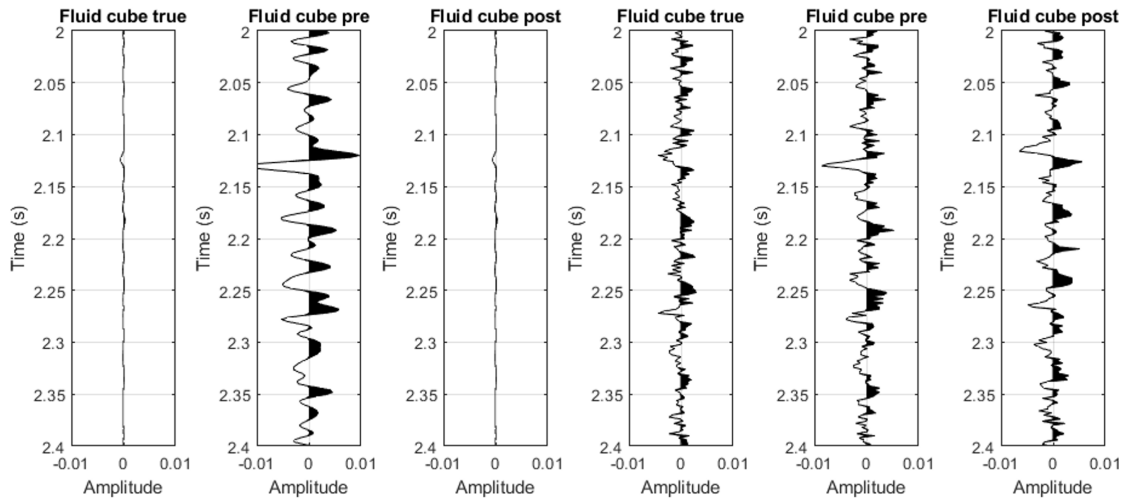

Figure 7.14: *Model 1 fluid traces. True: original seismic. Pre: after adding RMO. Post: after cross correlation. Three to the left: without noise. Three to the right: white Gaussian noise.*

7.3.2   Model 2: Class 2p anomaly

Figure 7.15 shows the true and post-correction AVO responses fir Model 2. It is important to remember that for this model, there was not added any RMO to alter the gather. The goal was simply to see if the method wrongly handled apparent RMO or not. The blue points represent the AVO response post-correction, while the green points are the true AVO reponse. Considering the small time-window of the anomaly, not many points are plotted. The first observation is the blue points for the noise-free case seem to shift to following a trend with a flatter inclination. The spread is also slightly increased, meaning the gradient amplitude should increase in large areas. The AVO response for the noisy seismic is hard to make much of by only looking at the cross plot.
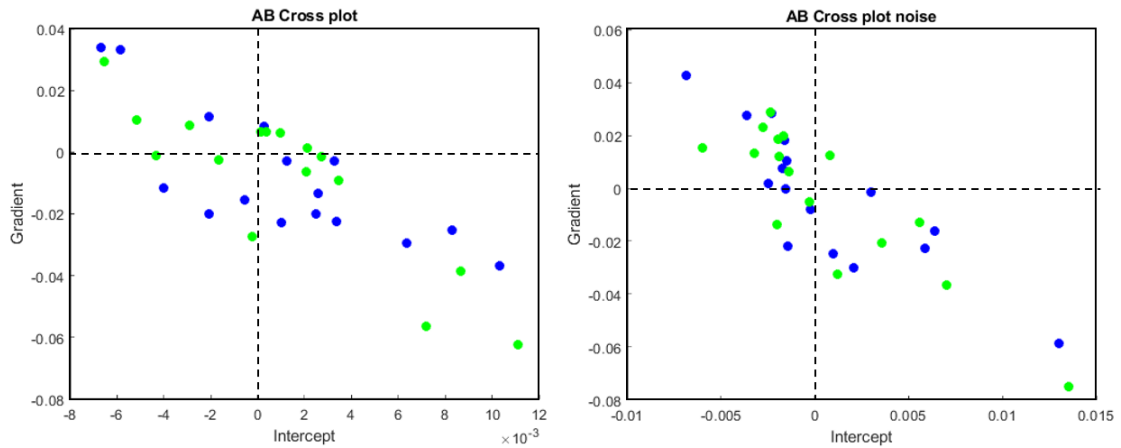
Figure 7.15: *Model 2 intercept and gradient cross plot. Green: true AVO response. Blue: AVO response with RMO. Left: without noise. Righ: white Gaussian noise.*

By looking at the intercept traces in Figure 7.16, we can see amplitude differences between the true and post-correction responses, especially in the top of the section at around $t = 2.09$. However, this difference is small. The general shape of the traces is still very much the same.
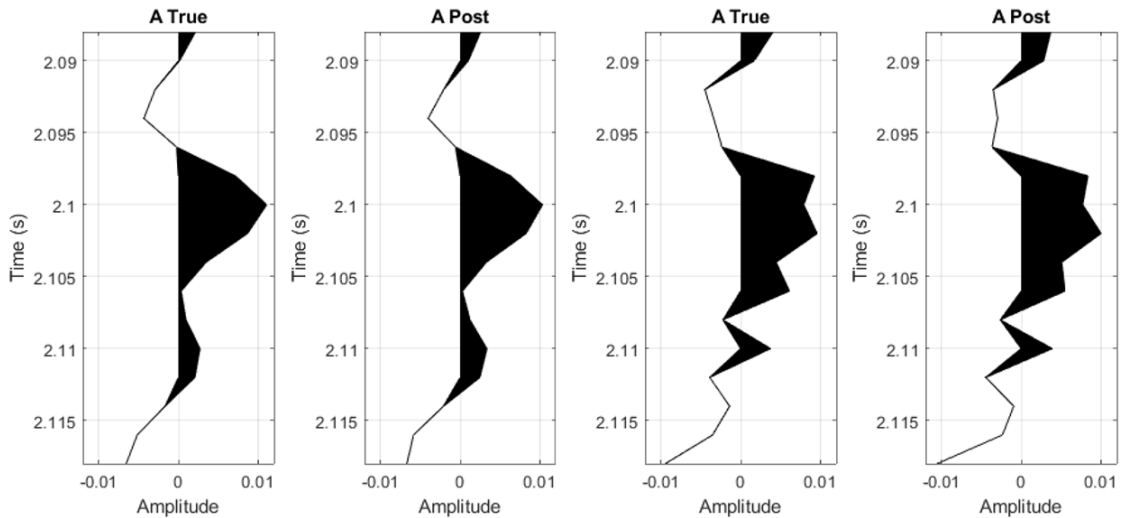

Figure 7.16: *Model 2 intercept traces. True: original gather. Post: after cross correlation. Two to the left: noise-free. Two to the right: white Gaussian noise.*

The gradient traces experience much more variation than the intercept, as seen in Figure 7.17. The clearest difference is at $t = 2.09$ s, where the amplitude changes sign, both for the seismic with and without noise. Wrongly flattening the gather causes this dramatic difference. Apart from the change at the upper part of the anomaly, the traces share shape, but there are massive differences in amplitudes when noise is and is not present.
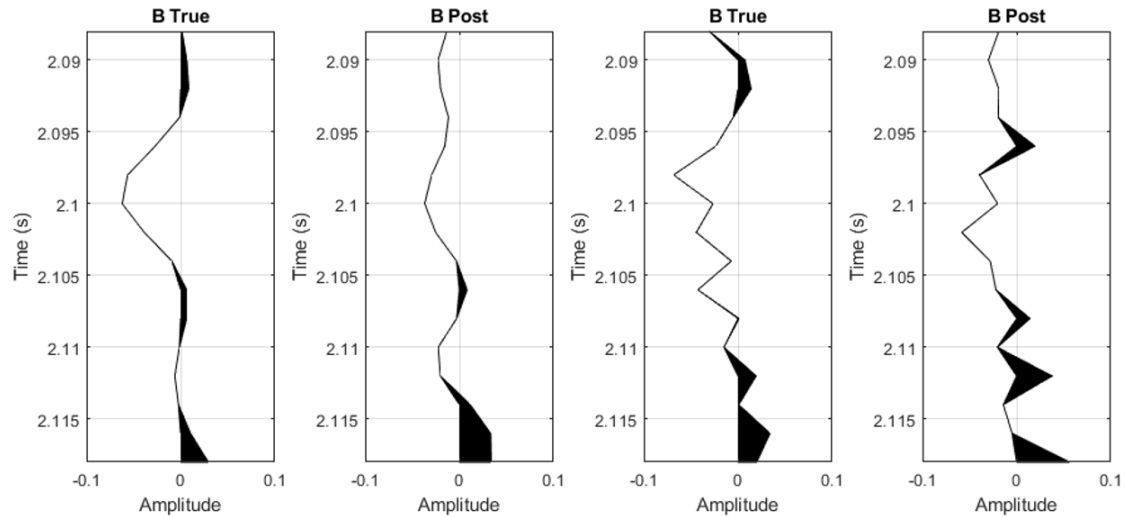
Figure 7.17: *Model 2 gradient traces. True: original gather. Post: after cross correlation. Two to the left: noise-free. Two to the right: white Gaussian noise.*

7.3.3 Summary

The AVO response for model 1 was greatly improved by applying cross correlation to correct for the residual move-out applied to the seismic. Considering the intercept and gradient where estimated by only using two points (N and F), the inclination of the background trend appears to become very flat. This resulted in a very high chi angle rotation to obtain the fluid cubes. Even though it didn't remove all the residual move-out, what was removed provided huge difference in estimation of the gradient. Considering the fluid cube was near-zero strengthens the importance too.

For model 2 the results weren't good, but expected. The intercept wasn't affected much, but the gradient estimation was completely wrong.

Chapter 8

Joint Bayesian AVO and RMO inversion

In a Bayesian setting, prior knowledge is combined with measured data to quantify the degree of belief in an event. The prior knowledge is considered to be what is known before acquiring data. In the context of seismic modelling and inversion, the seismic is considered the observed data, so the prior knowledge can be everything else. It is common to consider even well log data to be known *a priori*, as done in this thesis. Considering the uncertainty in seismic, a Bayesian setting is considered a natural approach when solving geophysical problems. This chapter will present the theory of a newly developed joint Bayesian AVO and RMO inversion, considered an extension to the method first proposed in Buland & Omre (2003), and then test its ability to perform the needed preconditioning done prior to AVO analysis.

8.1 Theory and implementation

Bayes theorem describes the probability of one event happening given another already has occurred, and is given by:

$$p(a|b) = \frac{p(b|a)p(a)}{p(b)},\qquad(8.1)$$

where $p(a)$ and $p(b)$ are the probabilities of the independent events a and b happening. The probability of event a happening given b already happened, is known as the posterior, $p(a|b)$, while $p(b|a)$ is the probability of event b happening given a already has, also known as the likelihood. In the context of seismic inversion (and solving the problem $\mathbf{d} = g(\mathbf{m}) + \mathbf{e}$) the equation can be rewritten to the form:

$$p(\mathbf{m}|\mathbf{d}) = \frac{p(\mathbf{d}|\mathbf{m})p(\mathbf{m})}{p(\mathbf{d})},\qquad(8.2)$$

where the vectors $\mathbf{d}$ and $\mathbf{m}$ represents the data and elastic parameters respectively. Since $p(\mathbf{d})$ does not depend on the unknown $\mathbf{m}$, it can be considered a normalizing constant for the posterior distribution (Buland & Omre (2003)). This reduces the expression to:

$$p(\mathbf{m}|\mathbf{d}) \propto p(\mathbf{d}|\mathbf{m})p(\mathbf{m}). \tag{8.3}$$

The purpose of this chapter is to present a new approach based on an expansion of the inversion first presented by Buland & Omre (2003) to not only invert for the elastic parameters, but also the RMO given by the formula $\Delta t(\theta) = a\theta^2 + b\theta$, now denoted as:

$$\boldsymbol{\zeta} = \begin{bmatrix} a \\ b \end{bmatrix}. \tag{8.4}$$

Incorporating the RMO, $\boldsymbol{\zeta}$, into expression 8.3 yields:

$$p(\mathbf{m}, \boldsymbol{\zeta}|\mathbf{d}) \propto p(\mathbf{d}|\mathbf{m}, \boldsymbol{\zeta})p(\mathbf{m}, \boldsymbol{\zeta}), \tag{8.5}$$

where $p(\mathbf{m}, \boldsymbol{\zeta}|\mathbf{d})$ is the posterior probability, which reads as "the probability of $\mathbf{m}$ and $\boldsymbol{\zeta}$ given the data $\mathbf{d}$". We assume $\mathbf{m}$ and $\boldsymbol{\zeta}$ are statistically independent, so $\text{Cov}(\mathbf{m}, \boldsymbol{\zeta}) = 0$, and the expression can be written as:

$$p(\mathbf{m}, \boldsymbol{\zeta}|\mathbf{d}) \propto p(\mathbf{d}|\mathbf{m}, \boldsymbol{\zeta})p(\mathbf{m})p(\boldsymbol{\zeta}), \tag{8.6}$$

where $p(\mathbf{d}|\mathbf{m}, \boldsymbol{\zeta})$ is the likelihood of $\mathbf{d}$ given $\mathbf{m}$ and $\boldsymbol{\zeta}$, and $p(\mathbf{m})$ and $p(\boldsymbol{\zeta})$ are the prior distributions of $\mathbf{m}$ and $\boldsymbol{\zeta}$ respectively.

The goal is to maximize the posterior distribution $p(\mathbf{m}, \boldsymbol{\zeta}|\mathbf{d})$, and since the data is given and considered a normalizing constant, the maximum posterior distribution, MAP, is:

$$\left[\hat{\mathbf{m}}, \hat{\boldsymbol{\zeta}}\right] = \underset{\mathbf{m}, \boldsymbol{\zeta}_t}{\text{argmax}}(p(\mathbf{d}|\mathbf{m}, \boldsymbol{\zeta}_t)p(\mathbf{m})p(\boldsymbol{\zeta}_t)). \tag{8.7}$$

Keep in mind that the MAP is only the optimal solution. This is a big difference between this approach and the one presented in Buland & Omre (2003), where they completely remain in the Bayesian domain by deriving an expression for the complete posterior solution.

When both the likelihood and prior models are Gaussian, the MAP corresponds to minimizing the objective function:

$$\phi(\mathbf{m}, \boldsymbol{\zeta}) = \frac{1}{2}(\mathbf{d}(\boldsymbol{\zeta}) - g(\mathbf{m}))^T \boldsymbol{\Sigma}_e^{-1}(\mathbf{d}(\boldsymbol{\zeta}) - g(\mathbf{m})) + \frac{1}{2}(\mathbf{m} - \boldsymbol{\mu}_m)^T \boldsymbol{\Sigma}_e^{-1}(\mathbf{m} - \boldsymbol{\mu}_m)$$
$$+ \frac{1}{2}\left(\frac{a^2}{\Sigma_a^2}\right) + \frac{1}{2}\left(\frac{b^2}{\Sigma_b^2}\right). \tag{8.8}$$

Another main difference from the method proposed by Buland & Omre (2003) is the addition of $p(\boldsymbol{\zeta})$, and that $\mathbf{d}$ is changed as a function of $\boldsymbol{\zeta}$ and not kept constant. Basically, we want to find the data and elastic parameters which results in the highest posterior.

It is important to note that for a given $\mathbf{d}$ and $\boldsymbol{\zeta}$, the optimal solution for $\mathbf{m}$ is given by the posterior expectation $\boldsymbol{\mu}_{\mathbf{m}|\mathbf{d}}$, which can be found using the explicit expression derived in 2.2.8 and Buland & Omre (2003).

In order to minimize the objective function we have to look at the gradient, which represents the change of the function as a function of its parameters. At the minimum point, the gradient is zero,

$$\nabla\phi(\mathbf{m}, \zeta) = 0. \tag{8.9}$$

In order to solve this multi-dimensional problem, a numerical approach using Newton's method has been chosen, which generally is denoted:

$$\boldsymbol{\zeta}_{k+1} = \boldsymbol{\zeta}_k - \mathbf{H}_k^{-1}\nabla\phi(\mathbf{m}, \boldsymbol{\zeta}_k), \tag{8.10}$$

where $\mathbf{H}$ is the Hessian matrix, and $\nabla\phi(\mathbf{m}, \boldsymbol{\zeta}_k)$ is the gradient with regards to $\boldsymbol{\zeta}$. Considering we can use the Bayesian linearized AVO inversion method described in subsection 2.2.8 to find the optimal $\mathbf{m}$, the algorithm can be simplified to only find the optimal $\mathbf{d}$, by estimating the residual move-out,

$$\boldsymbol{\zeta}_{k+1} = \begin{bmatrix} a_{k+1} \\ b_{k+1} \end{bmatrix} = \begin{bmatrix} a_k \\ b_k \end{bmatrix} - \mathbf{H}_k^{-1}\nabla\phi(\mathbf{m}, \boldsymbol{\zeta}), \tag{8.11}$$

where the Hessian matrix which is given by:

$$\mathbf{H} = \begin{bmatrix} \frac{\partial^2 \nabla\phi(\mathbf{m}, \boldsymbol{\zeta}_t)}{\partial a^2} & \frac{\partial^2 \nabla\phi(\mathbf{m}, \boldsymbol{\zeta}_t)}{\partial a \partial b} \\ \frac{\partial^2 \nabla\phi(\mathbf{m}, \boldsymbol{\zeta}_t)}{\partial a \partial b} & \frac{\partial^2 \nabla\phi(\mathbf{m}, \boldsymbol{\zeta}_t)}{\partial b^2} \end{bmatrix}. \tag{8.12}$$

Given the non-linearity of the problem, we do not have explicit expressions for the solutions for $\boldsymbol{\zeta}$, and the Hessian matrix has to be found numerically. As mentioned, the objective function is at a minimum point when the gradient is zero and the Hessian is positive definite. However, this is not just the case for the global minimum, but also a local one. For that reason, one should be cautious with the initial guess in order to make sure the algorithm does not get caught in a poor local minimum. It is important to note that we assume Gaussian $\boldsymbol{\zeta}$, while for $\mathbf{m}$ only the posterior from the Bayesian linearized AVO inversion is used. In other words, $\boldsymbol{\zeta}$ and $\mathbf{m}$ are optimized one at the time.

8.2   Model 1: Background trend

The joint AVO and RMO inversion was implemented and tested on the seismic sections. The method differs from semblance and RVI in the sense that it is not directly related to velocity errors. We consider RMO a combination of velocity errors, anisotropy, complex geology and other reasons, and to be defined by $\Delta t = a\theta^2 + b\theta$. It was added to the data prior to inversion by:

$$\boldsymbol{\zeta}_{pre} = \begin{bmatrix} 0.02 \\ 0.002 \end{bmatrix}. \tag{8.13}$$

Figure 8.1 depicts the move-out curve. It is important to note once again that the values given by $\boldsymbol{\zeta}$ in expression 8.13 is not the only desirable solution.
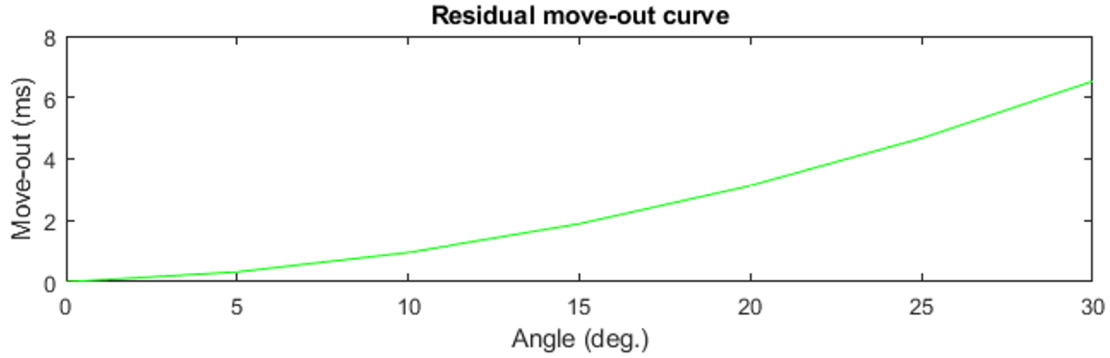

Figure 8.1: *Model 1 move-out curve describing the residual move-out added to the seismic prior to inversion.*

8.2.1 Prior information

Considering we have no idea whether the RMO is positive or negative *a priori*, we have to define prior distributions for a and b that cover reasonable amounts of positive and negative RMO. In addition, prior models for the elastic parameters have to be defined too. For Model 1 the prior model for a and b are defined by:

$$\begin{bmatrix} \mathbf{a} \\ \mathbf{b} \end{bmatrix} \sim \mathcal{N}\left(\begin{bmatrix} 0 \\ 0 \end{bmatrix}, \begin{bmatrix} \sigma_a^2 & 0 \\ 0 & \sigma_b^2 \end{bmatrix} \right), \tag{8.14}$$

with $\sigma_a = 0.015$, and $\sigma_b = 0.0015$. It is important to note that a and b are assumed independent, meaning $\mathrm{Cov}(a,b) = 0$. However, correlation between the constants may be defined by the user if found desirable. The normal distributions are shown in Figure 8.2. The left side of the figure is the normal distribution for a, while the middle figure shows the distribution for b. The right side of the figure shows 200 random move-out curves from the distributions, which are clearly covering the range of the RMO applied to the data prior to inversion.
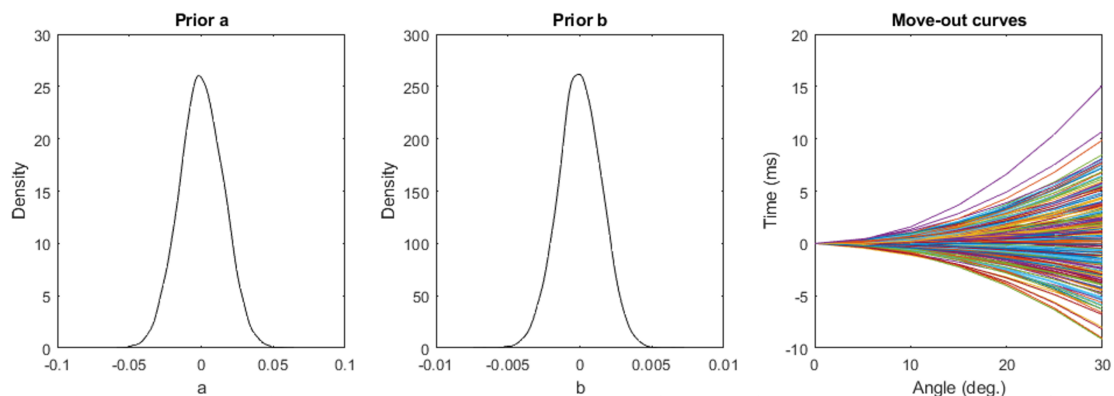
Figure 8.2: *Model 1. Left: Prior distribution for a. Middle: Prior distribution for b. Right: 200 random move-out curves from distributions.*

Regarding the prior distributions for the elastic parameters, they are easier to set than the prior for a and b, as the self-made Vp-, Vs- and density-logs can be considered to be known *a priori*. As they are somewhat following a low-frequency trend of increasing values with depth, the mean of the distributions were set to follow a line with a similar trend. The standard deviation for all of them was chosen to acquire distributions vague enough to cover the range of values and them some. The different distributions are seen in Figure 8.3, where the black lines are the real log values, and the red dotted lines represent the 90% confidence interval.
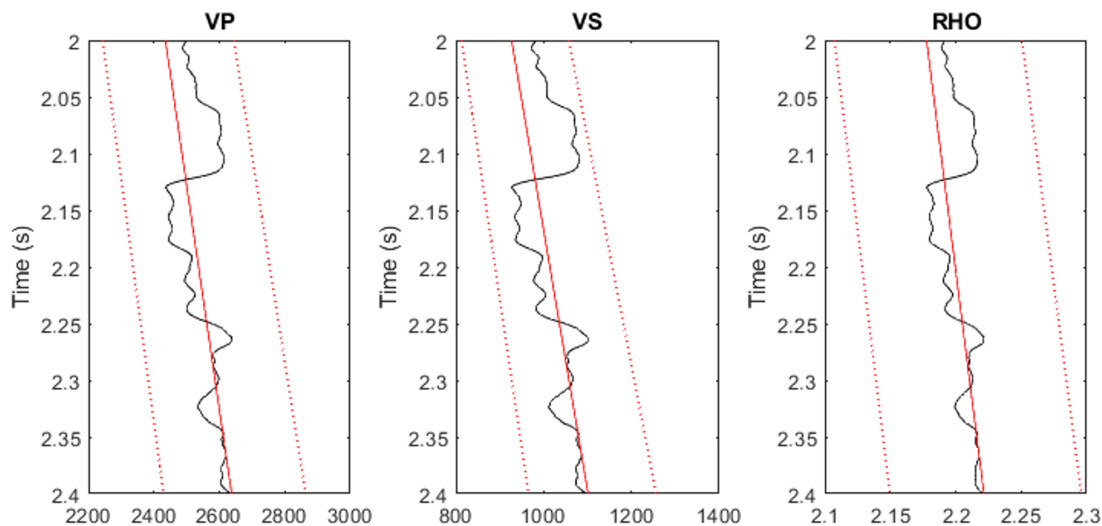

Figure 8.3: *Model 1 elastic parameter prior distributions. Black line: true parameters. Red line: mean prior parameters. Red dotted line: prior 90% confidence interval.*

8.2.2   Noise free gather

Figure 8.4 shows three seismic sections completely following the background trend. On the left we have the original seismic modelled from the logs in figure 8.3. The

73

middle gather has been altered by adding RMO, while the right is showing the corrected seismic after inversion. One can clearly see that the residual move-out is removed, and the gather has been flattened - as it should be.
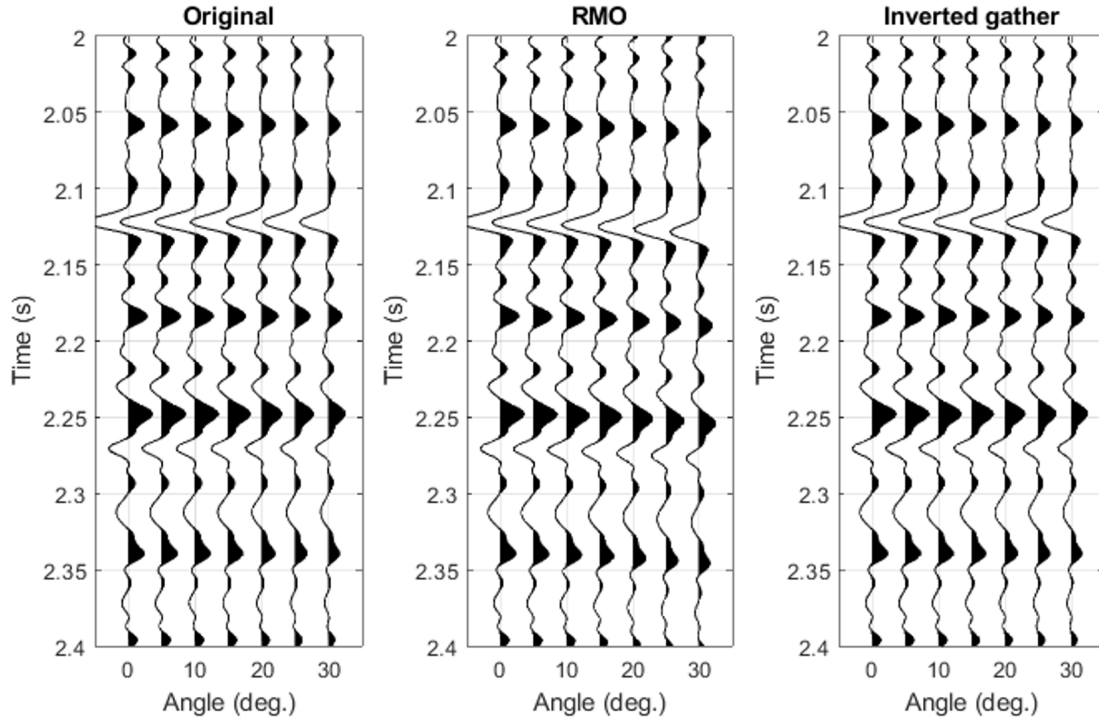

Figure 8.4: *Model 1 without noise. Left: Original gather. Middle: gather with RMO. Right: gather obtained from inversion.*

The iteration process is shown in Figure 8.5. The graph clearly shows that a large step was made early in the iteration process, followed by a small step to correct the slight over-stepping. The initial guesses are represented by the first value in the graph, and where randomly drawn from the distributions showed in Figure 8.2 in section 8.2.1. It is important to note that a natural initial guess would be to assume there is no residual move-out present, in other words $a = 0$ and $b = 0$. However, they were randomly drawn from the distributions to investigate the importance of a decent initial guess to not get trapped in a local minimum.
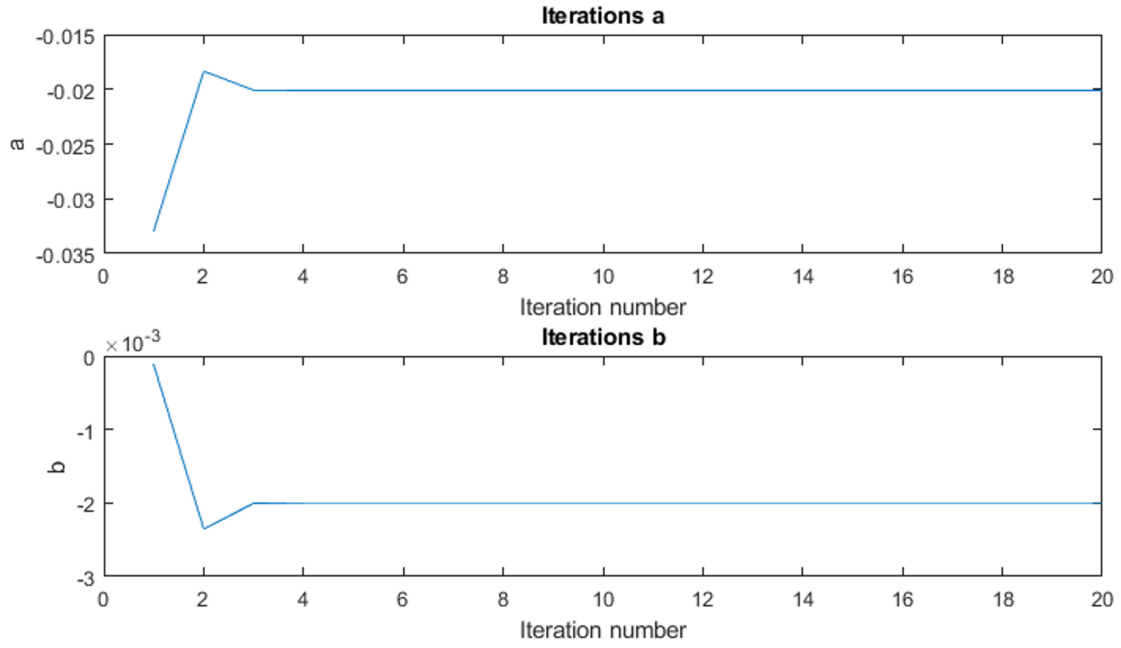
Figure 8.5: *Model 1 noise-free iteration process for a and b.*

The answer obtained was:

$$\boldsymbol{\zeta}_{post} = \begin{bmatrix} -0.0201 \\ -0.0020 \end{bmatrix}.$$ (8.15)

It is important to note that the method corrects the seismic by an amount that cancels out the RMO added prior to inversion. Hence, the answer obtained from the method will be of opposite sign, and $\boldsymbol{\zeta}_{post}$ will mirror $\boldsymbol{\zeta}_{pre}$. In order to compare the move-out curves properly, the absolute value of the move-out curves were plotted as seen in Figure 8.6. As the figure shows, the curves are similar to the point of near-complete overlap.
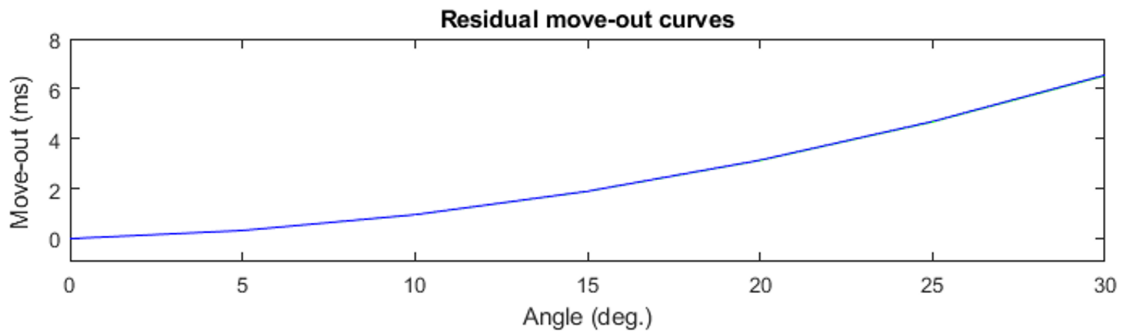

Figure 8.6: *Model 1 noise-free move-out curves. Green: true move-out curve added to the seismic. Blue: move-out curve obtained from inversion.*

Elastic parameters

In addition to acquiring the residual move-out, the elastic parameters are also inverted for. To see the improvement in elastic parameters done by correcting for RMO, the seismic section altered with RMO was also inverted using the Bayesian linearized AVO inversion described in 2.2.8. Figure 8.7 depicts the seismic section altered with RMO, and the inverted elastic parameters. The thick black, blue and red lines represent the true, prior and inverted elastic parameters respectively. The dotted lines define the 90% confidence interval. The inverted elastic parameters on the altered seismic shows promising results in most part of the gather, but struggles to replicate the large increase in elastic parameters at $t = 2.05$ s. At deeper parts the inverted parameters resemble the true parameters with a decent accuracy. Especially for the density. This is likely due to the prior being so close to the true.
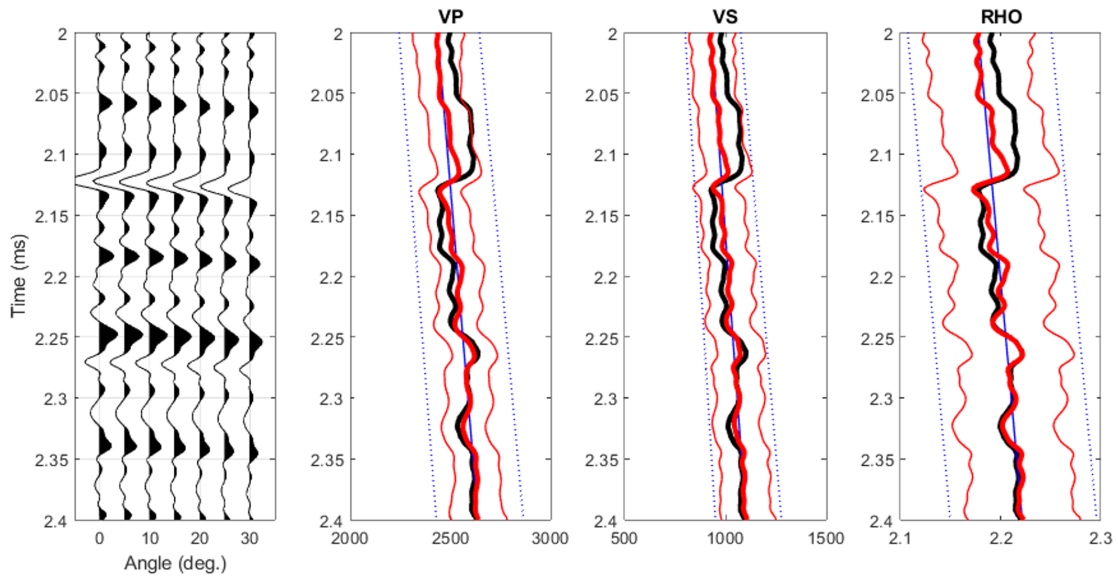

Figure 8.7: *Left: Model 1 noise-free seismic with RMO. Black line: True elastic parameters. Thick red line: Optimal inverted parameters. Thin red line: 90% confidence interval. Thick blue line: Mean prior value. Thin dotted blue line: 90% confidence interval prior.*

Figure 8.8 shows the seismic and elastic parameters acquired using the joint Bayesian AVO and RMO inversion. The inverted parameters becoming nearly identical to the true parameters. In addition, the increase in parameters at $t = 2.05$ s is replicated to perfection in the inverted Vp and density, which it did not with the presence of RMO. Even though it lacks the same accuracy for Vs at that time, it still catches the increasing trend, something it did not in Figure 8.7. The deeper parts of the gather are also improved, as the inverted parameters almost completely overlap the true parameters.
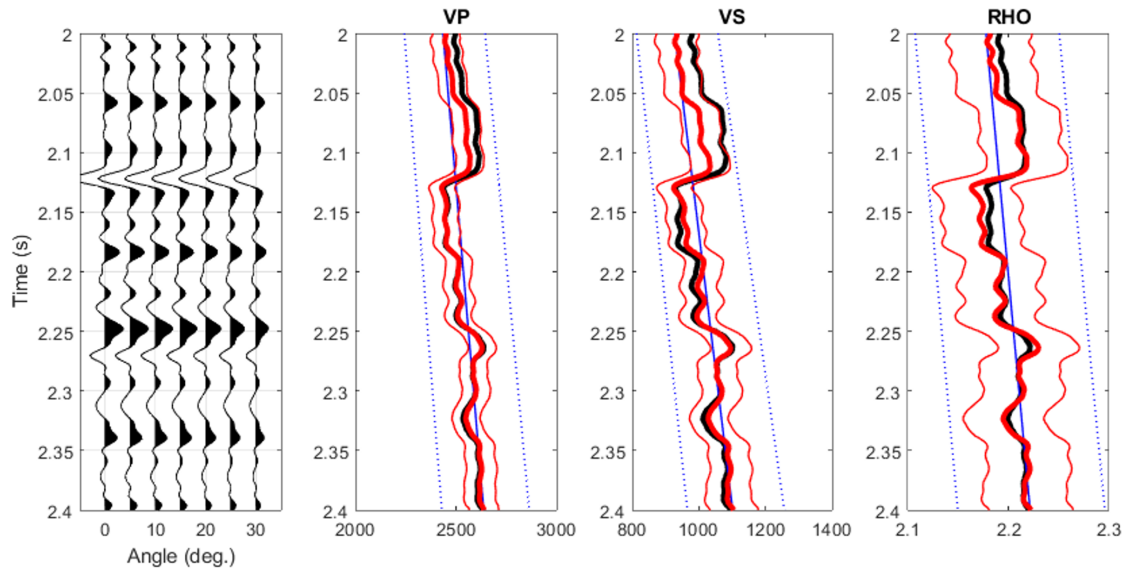
Figure 8.8: *Left: Model 1 noise-free seismic after joint Bayesian AVO and RMO inversion. Black line: True elastic parameters. Thick red line: Optimal inverted parameters. Thin red line: 90% confidence interval. Thick blue line: Mean prior value. Thin dotted blue line: 90% confidence interval prior.*

8.2.3 White Gaussian noise

The joint inversion method was also tested on noisy seismic depicted in Figure 8.9. The left gather represents the original seismic, the middle gather is altered by adding RMO defined by the move-out curve in Figure 8.1. The left gather shows the corrected seismic obtained after inversion.
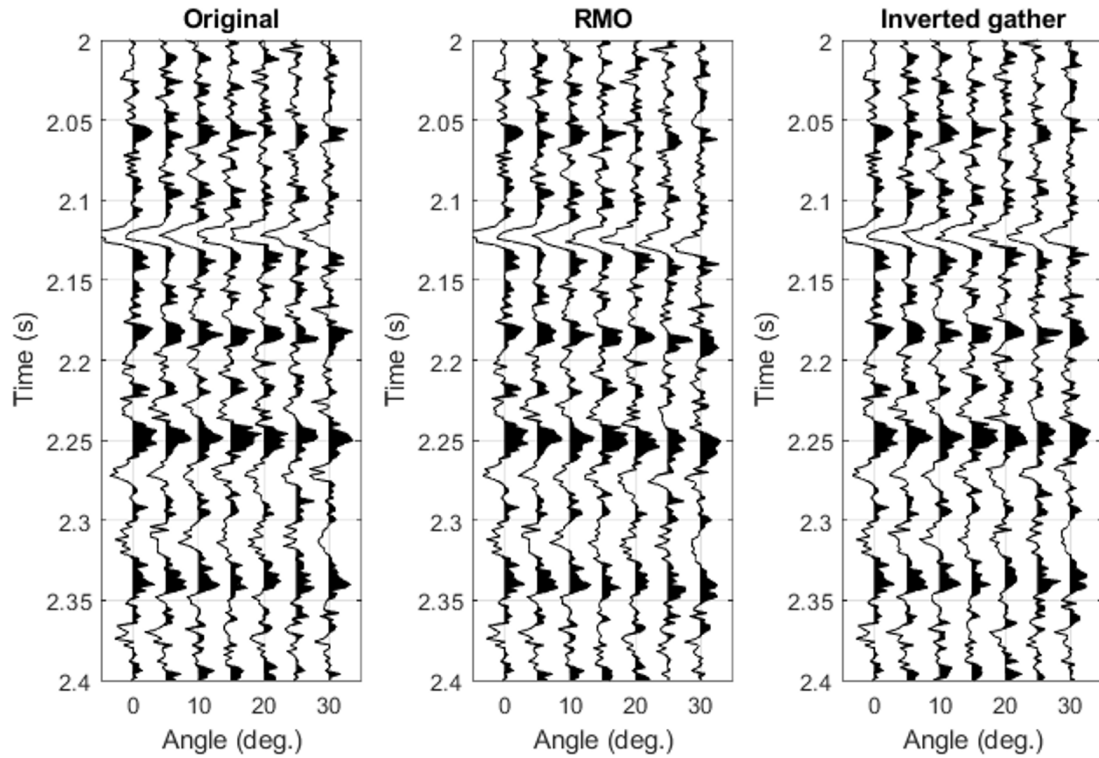
Figure 8.9: *Model 1 with white Gaussian noise. Left: Original gather. Middle: gather with residual move-out. Right: gather obtained from inversion.*

In the presence of noise, the method converged slower and the solution was obtained after 7 iterations as seen in Figure 8.10. Even though the initial guess was close to the final answer, the algorithm seems to overstep massively based on the gradient and Hessian it calculates at the point. Another important observation is the behaviour prior to converging, where it appears to take small steps toward the solution. The increase in computation time is likely related to the presence of noise.
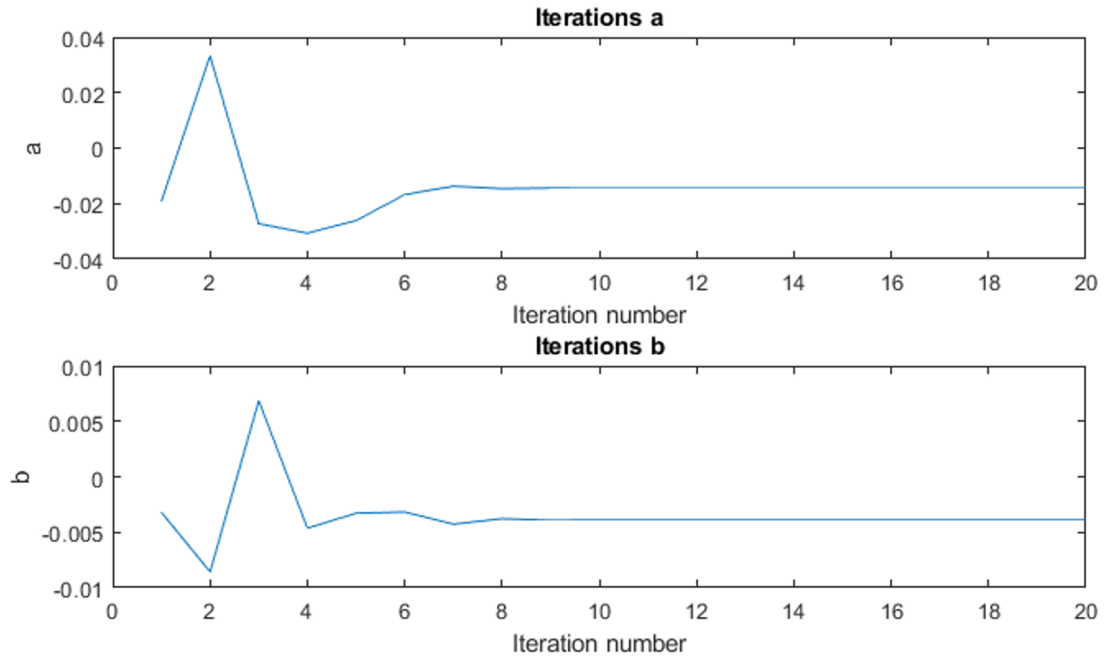
Figure 8.10: *Model 1 with white Gaussian noise iteration process for a and b*

The final answer obtained,

$$\boldsymbol{\zeta}_{post} = \begin{bmatrix} -0.0138 \\ -0.0037 \end{bmatrix}, \tag{8.16}$$

is not exactly similar to $\boldsymbol{\zeta}_{pre}$. In fact, a is lower and b is higher. However, by looking at the absolute value move-out curves in Figure 8.11, they almost completely overlap. This is related to the earlier mention that even though there is only one optimal solution of a and b, there are several desirable solutions.
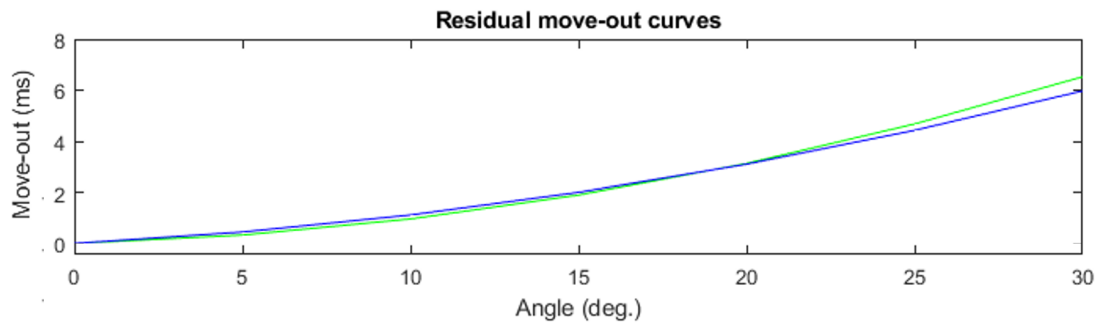

Figure 8.11: *Model 1 with white Gaussian noise move-out curves. Green: true move-out curve added to the seismic. Blue: post-correction move-out curve obtained from inversion.*

Elastic parameters

Figure 8.12 shows the seismic altered with RMO and white Gaussian noise to the left. The corresponding Vp, Vs and density were obtained by only inverting for elastic parameters and not RMO. Even in the presence of RMO, the inverted parameters are decent for most of the seismic. Keep in mind that this is likely due to the prior (blue) following the true (black) so well. That being said, it completely fails in catching the large increase and sudden drop in parameters between $t = 2.0\,\text{s}$ and $t = 2.1\,\text{s}$.
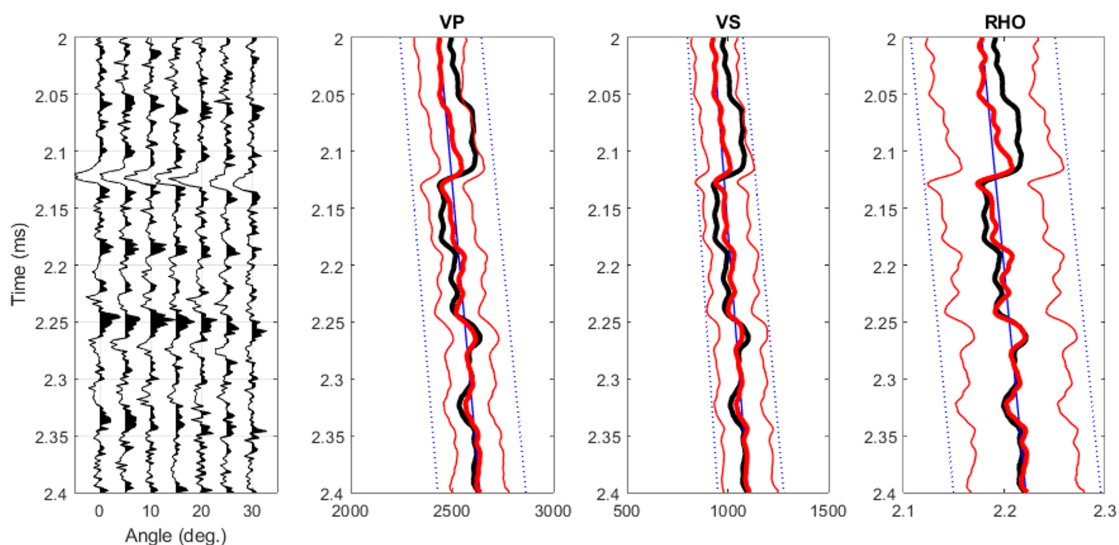

Figure 8.12: *Left: Model 1 with white Gaussian noise and RMO. Black line: True elastic parameters. Thick red line: Optimal inverted parameters. Thin red line: 90% confidence interval. Thick blue line: Mean prior value. Thin dotted blue line: 90% confidence interval prior.*

When inverting for both RMO and elastic parameters, the inverted Vp, Vs and density experience great improvement, as seen in Figure 8.13. In the area between $t = 2.0\,\text{s}$ and $t = 2.1\,\text{s}$ the Vp and density are greatly improved. In fact, the inverted density is completely overlapping the true density. The Vs is also improved in the same interval, but it does not overlap to the same extent as Vp and density. However, it manages to catch the trend of the increase and heavy decrease, which it failed to do when only inverting for elastic parameters.
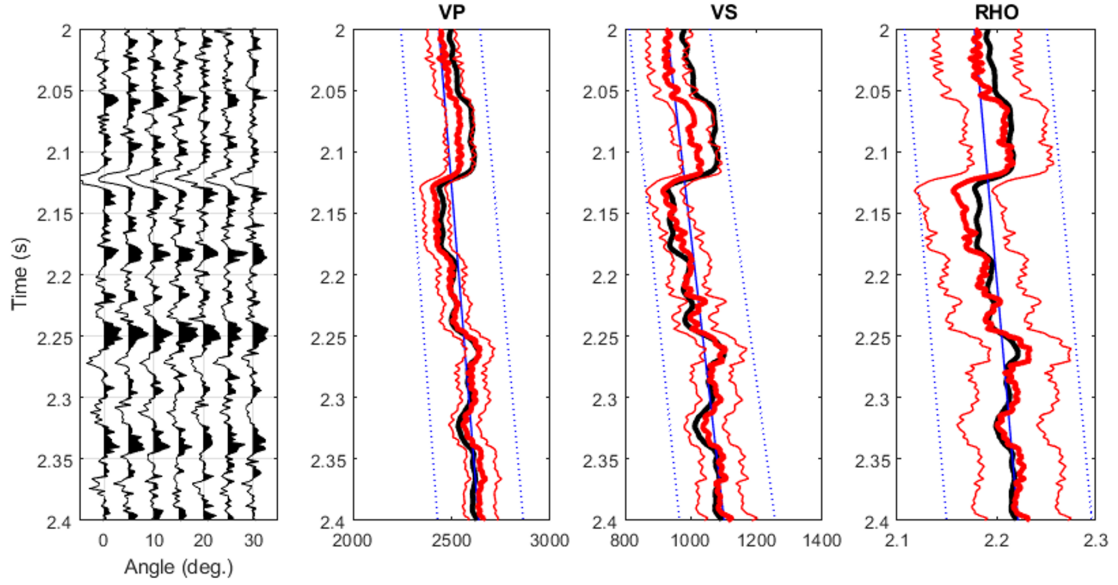
Figure 8.13: *Left: Model 1 with white Gaussian noise after joint Bayesian AVO and RMO inversion. Black line: True elastic parameters. Thick red line: Optimal inverted parameters. Thin red line: 90% confidence interval. Thick blue line: Mean prior value. Thin dotted blue line: 90% confidence interval prior.*

8.3 Model 2: Class 2p anomaly

For the case with the AVO Class 2p anomaly a different approach has been taken compared to the other methods. Instead of keeping the seismic as is to see if the method wrongly flattens it, RMO in the form:

$$\zeta_{pre} = \begin{bmatrix} -0.010 \\ -0.001 \end{bmatrix}, \tag{8.17}$$

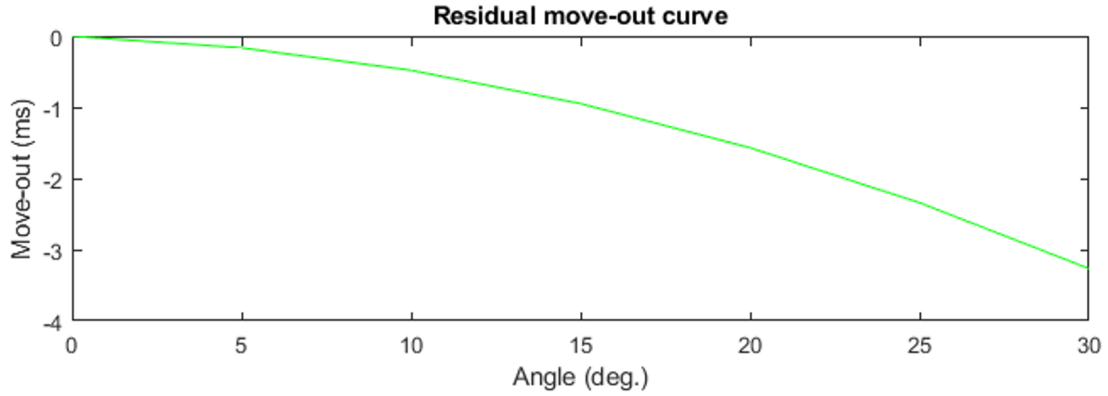was added to the section to see wether it was properly corrected. The move-out curve is depicted in figure 8.14

Figure 8.14: *Move-out curve describing the residual move-out added to the data before testing the inversion.*

8.3.1 Prior information

For Model 2 the prior models for a and b are defined as:

$$\begin{bmatrix} \mathbf{a} \\ \mathbf{b} \end{bmatrix} \sim \mathcal{N}\left(\begin{bmatrix} 0 \\ 0 \end{bmatrix}, \begin{bmatrix} \sigma_a^2 & 0 \\ 0 & \sigma_b^2 \end{bmatrix} \right), \tag{8.18}$$

with $\sigma_a = 0.008$ and $\sigma_b = 0.0008$. Figure 8.2 shows them both. Similarly to Model 1, a and b are assumed independent. The left of the figure shows the resulting distribution for a, while the middle figure shows the distribution for b. The right side of the figure shows 200 random move-out curves for the given distributions, which are clearly covering the range of the RMO applied to the data.
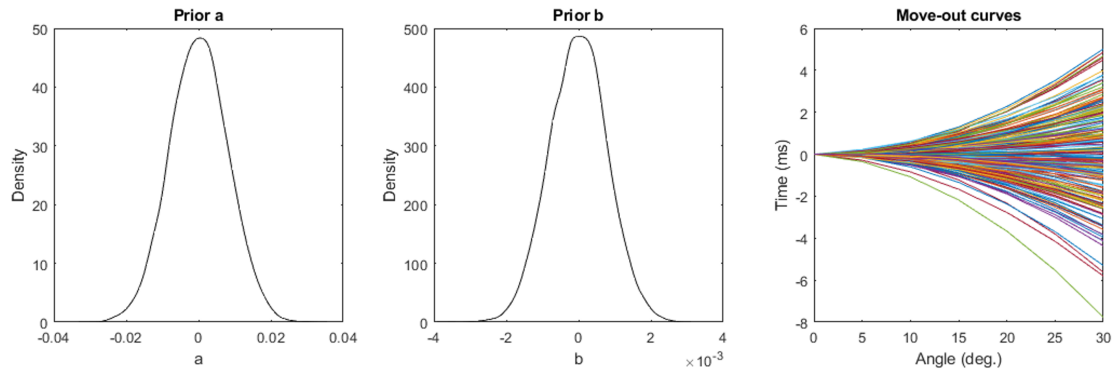

Figure 8.15: *Left: Prior distribution for a. Middle: Prior distribution for b. Right: 200 random move-out curves from distributions.*

A different approach in defining the prior model for the elastic parameters was chosen for Model 2. Considering the small size of the seismic section, it felt appropriate to keep it simple and just use the mean of the true parameters. The different

distributions are seen in Figure 8.3, where the black lines are the real log values, and the red dotted lines represent the 90% confidence interval. Similarly to Model 1, the initial values were randomly drawn from the distributions in Figure 8.15, to investigate the importance of a decent initial guess.
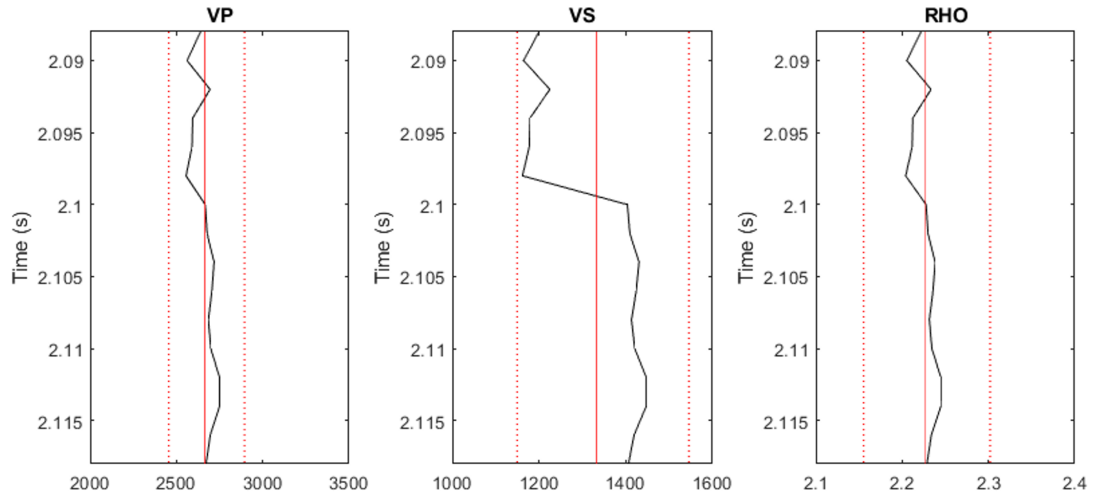

Figure 8.16: *Prior distributions for elastic parameters. Black line: true values. Red line: mean prior values. Red dotted line: prior 90% confidence interval*

8.3.2 Noise free gather

Figure 8.17 shows three seismic sections. The left model shows the true seismic, the middle section is after adding residual move-out described by Figure 8.14. By adding the RMO, the reflections appear to have been flattened. The gather to the right shows the seismic obtained after inversion. As seen, the method un-flattens the section, completely restoring the apparent RMO.

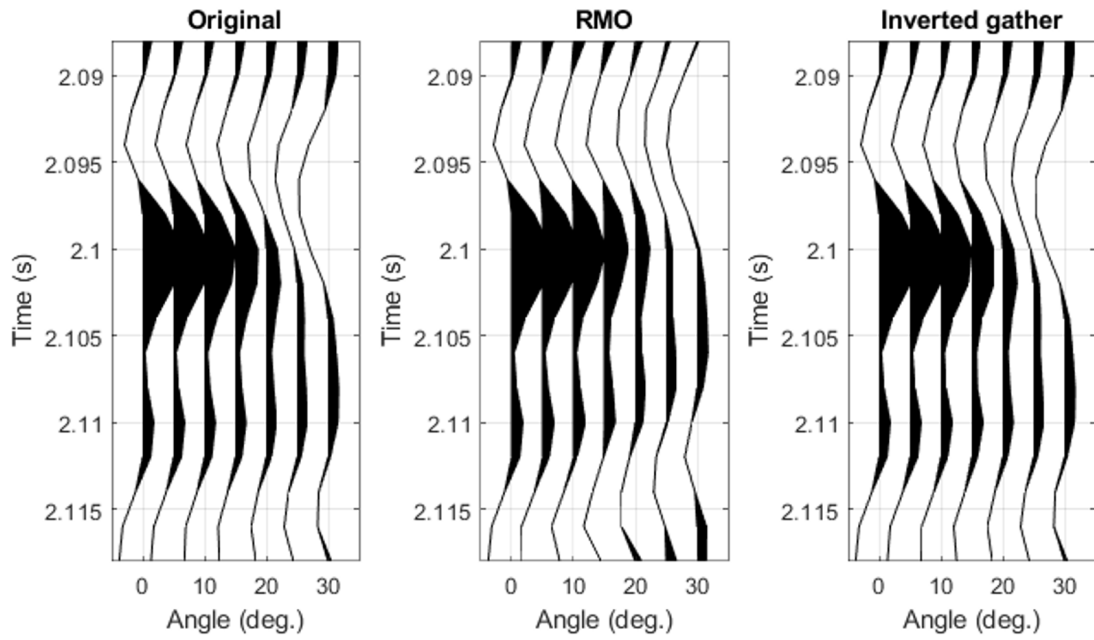**Figure 8.17:** *Model 2 noise-free. Left: Original gather. Middle: gather with RMO. Right: gather obtained from inversion.*

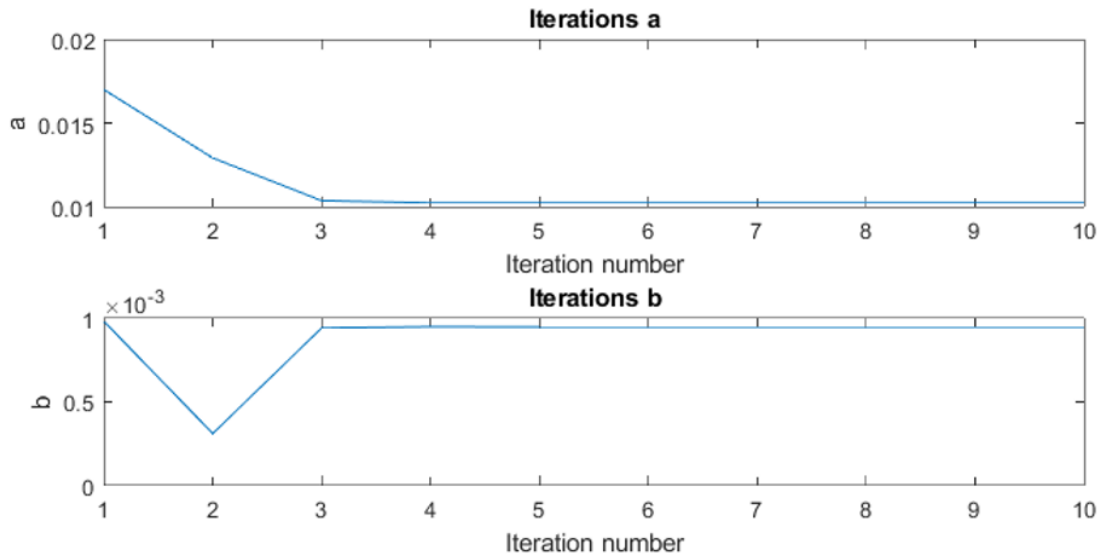Similarly to Model 1, the algorithm converged after only two iterations as seen in Figure 8.18.

Figure 8.18: *Model 2 noise-free iteration process for a and b.*

The answer obtained,

$$\boldsymbol{\zeta}_{pre} = \begin{bmatrix} -0.0099 \\ -0.00091 \end{bmatrix}, \tag{8.19}$$

is near-identical to $\boldsymbol{\zeta}_{pre}$. The move-out curves depicted in Figure 8.19 compares the absolute value move-out curves. As the figure shows, they are similar to almost completely overlapping. However, by looking closely, shades of $\boldsymbol{\zeta}_{pre}$ can be seen by the green color.
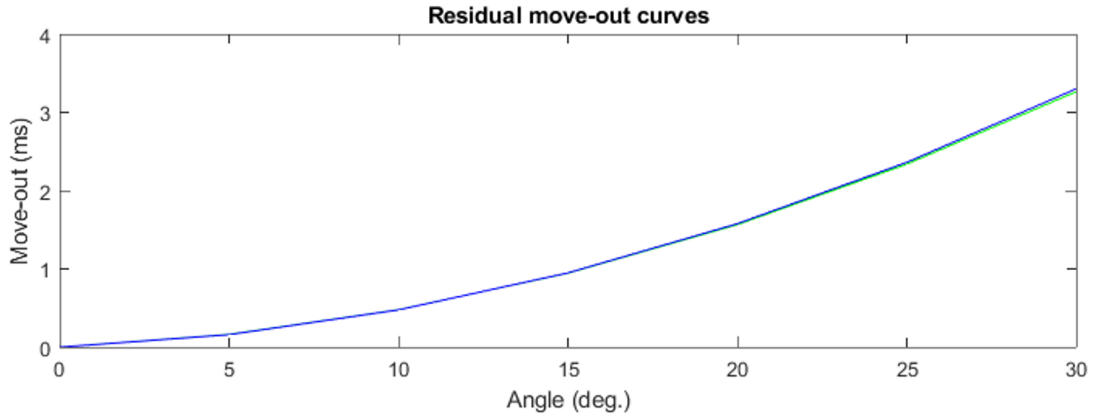

Figure 8.19: *Model 2 noise-free move-out curves. Green: true move-out curve added to the seismic. Blue: move-out curve obtained from inversion.*

Elastic parameters

Model 2 was also inverted for elastic parameters with and without RMO to examine the difference done by inverting for RMO too. The left side of Figure 8.20 shows the model with added RMO. Again, the thick black, blue and red lines represent the true, prior and inverted elastic parameters respectively. The dotted lines represent the 90% confidence interval. The first observation is the lack of accuracy to the inverted Vs at top anomaly ($t = 2.05\,\mathrm{s}$). It does not catch the trend at all, and in fact it seems to just wobble around the prior. The inverted Vp is decent, and follows the true response well. However, this is mostly due to the prior being close to the true. The inverted density also appears to be accurate, but for the same reasons.
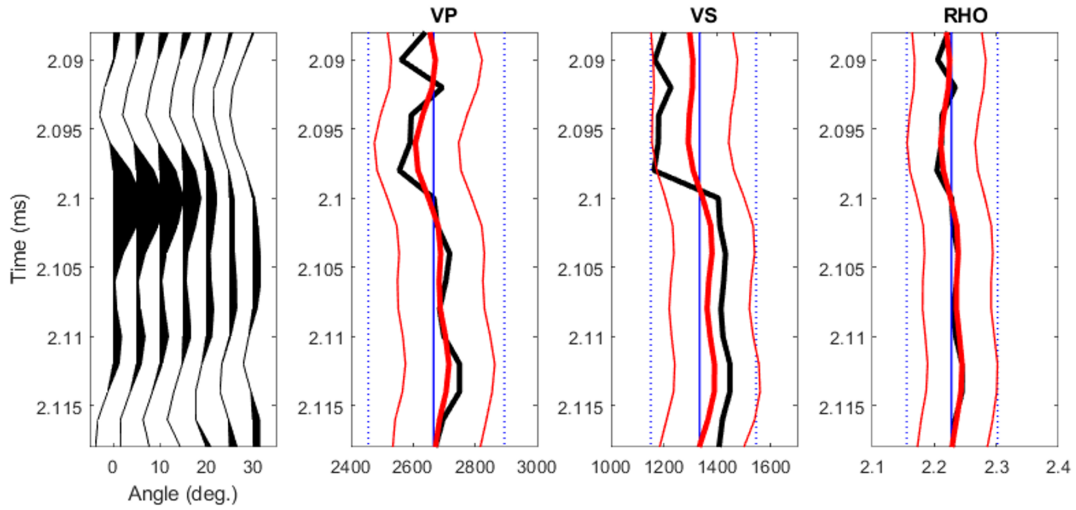
Figure 8.20: *Left: Model 2 noise-free seismic with added RMO. Black line: True elastic parameters. Thick red line: Optimal inverted parameters. Thin red line: 90% confidence interval. Thick blue line: Mean prior value. Thin dotted blue line: 90% confidence interval prior.*

When using the joint inversion to correct the seismic and invert for elastic parameters all together, the result is greatly improved as seen in Figure 8.21. It almost completely overlaps, and does and outstanding job at replicating the trend which causes the anomaly. The inverted density is shifted away from the prior in the shallow part, and manages to catch the increase in density causing the trend. The inverted Vp does not experience much of an improvement, but follows the true values with increased accuracy compared to the results in Figure 8.20. The inverted density becomes slightly smoother, but the accuracy is not improved.
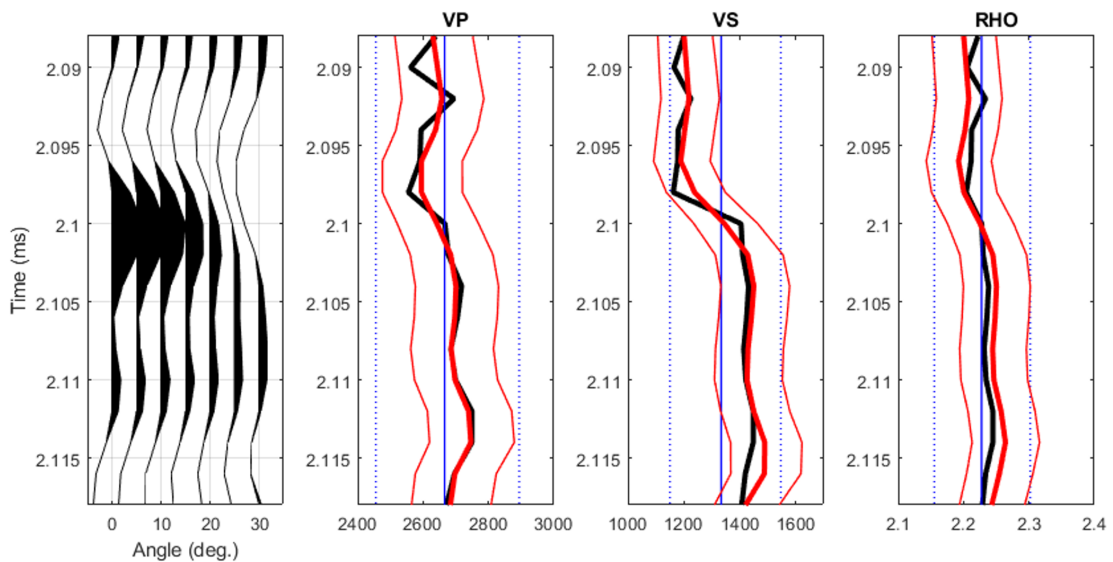

Figure 8.21: *Left: Model 2 noise-free seismic after joint Bayesian AVO and RMO inversion. Black line: True elastic parameters. Thick red line: Optimal inverted parameters. Thin red line: 90% confidence interval. Thick blue line: Mean prior value. Thin dotted blue line: 90% confidence interval prior.*

8.3.3 White Gaussian noise

The left side of Figure 8.22 shows the original gather with added white Gaussian noise. The middle gather is obtained by adding the RMO described by Figure 8.14, while the right gather is the one obtained by inversion.
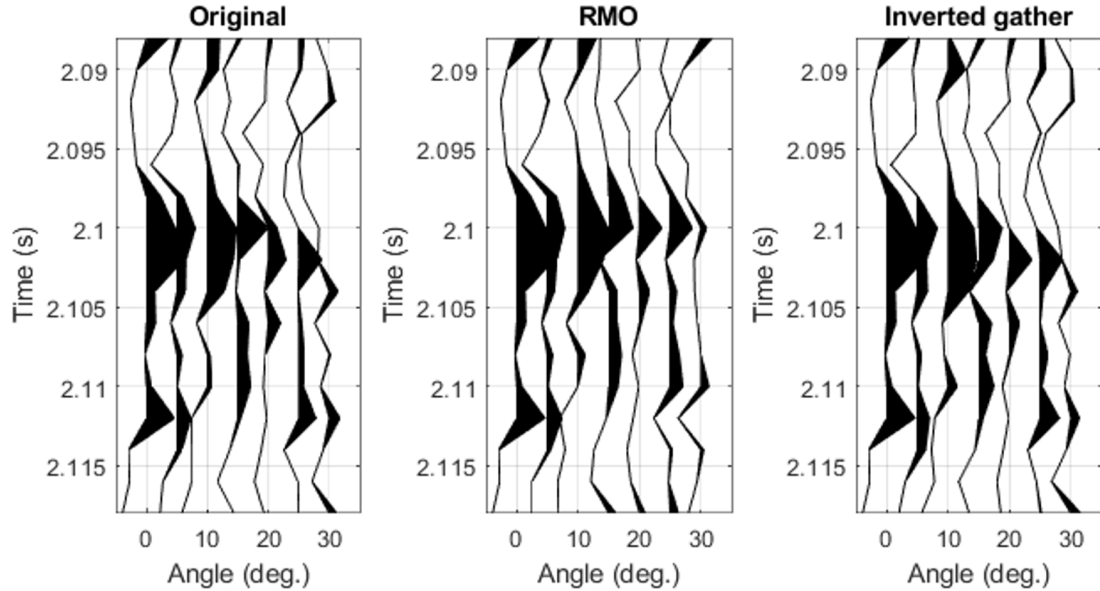
Figure 8.22: *Model 2 with white Gaussian noise. Left: Original gather. Middle: gather with residual move-out. Right: gather obtained from inversion.*

The method converges slower compared to the noise-free model, which was expected. The answer is obtained after 7 iterations as shown in Figure 8.23. By looking closer at the individual iterations, the algorithm appears to take very small steps towards the answer between iteration 3 and 8. This is likely due to the noise, which seems to decrease the algorithms ability to accurately obtain the proper step size to converge quicker.
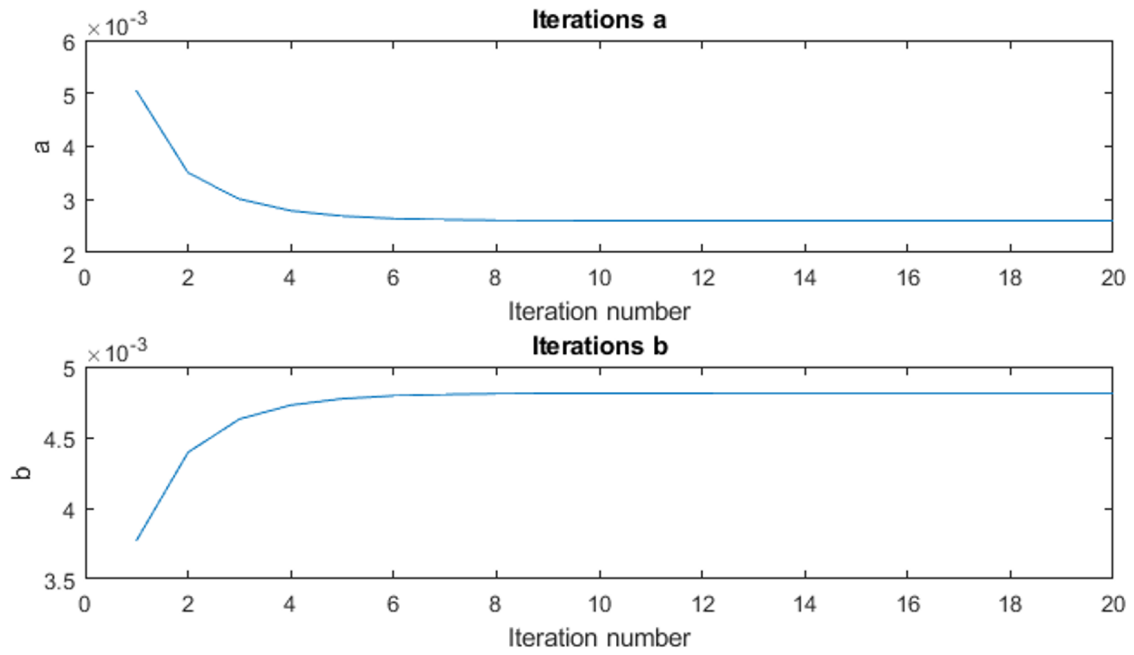
Figure 8.23: *Model 2 with white Gaussian noise iteration process for a and b.*

The answer obtained,

$$\zeta_{pre} = \begin{bmatrix} -0.0026 \\ -0.00831 \end{bmatrix}, \tag{8.20}$$

is very different from ζ_{pre}. By comparing the curves in Figure 8.24, one can observe that the real move-out curve in green and inverted move-out curve in blue are clearly different, but it is still a decent solution. In fact, the post-inversion move-out curve is linear, and fails to obtain the smooth curvature.

Figure 8.24: *Model 2 with white Gaussian noise move-out curves. Green: true move-out curve added to the seismic. Blue: move-out curve obtained from inversion.*

Elastic parameters

In addition to inverting for RMO, the elastic parameters are also obtained. In order to examine the improvement by correcting for RMO, the seismic altered with RMO was inverted for the elastic parameters too. Figure 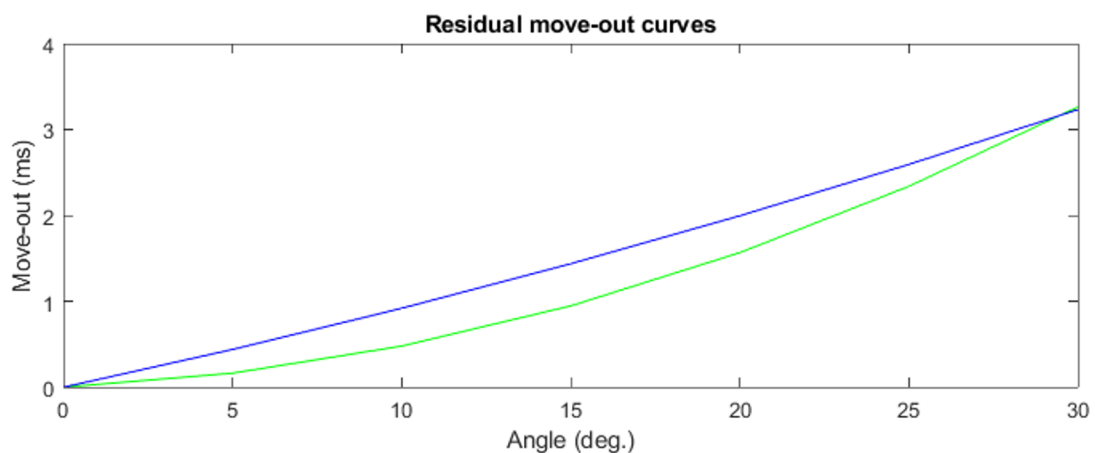8.25 shows the noisy gather containing RMO, along with the true and inverted elastic parameters. The black line represents the true parameters, while the blue and red lines represents the prior and inverted parameters respectively. The dotted lines represent the 90% confidence interval. The case is very much the same as the noise-free seismic, where the inverted Vp is decent but fails to properly catch the increase causing the anomaly. The Vs only wobbles around the prior, and completely fails to resemble the true. The inverted density appears to be accurate, however it is likely due to the prior being so close to the true.
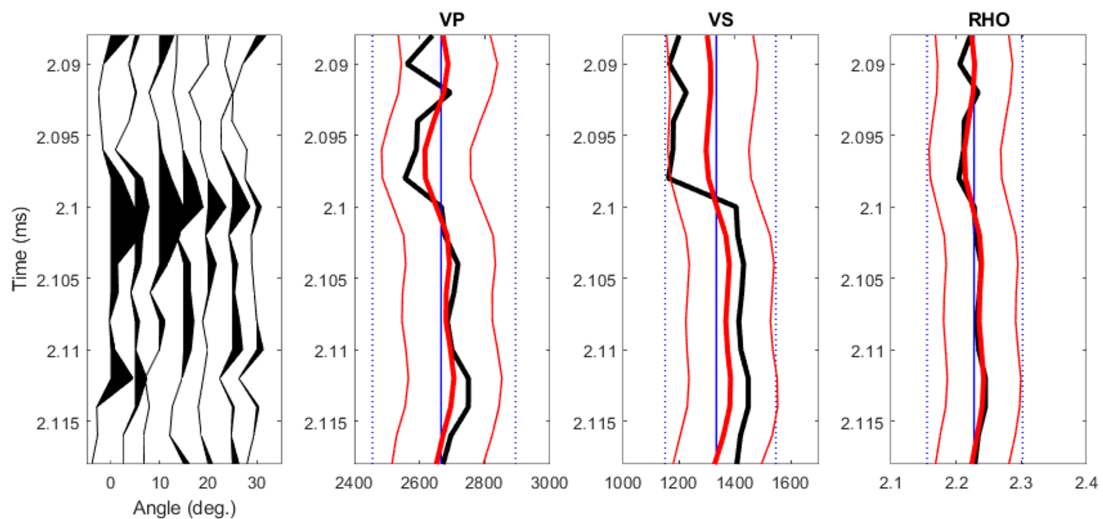
Figure 8.25: *Left: Model 2 white Gaussian noise and RMO. Black line: True elastic parameters. Thick red line: Optimal inverted parameters. Thin red line: 90% confidence interval. Thick blue line: Mean prior value. Thin dotted blue line: 90% confidence interval prior.*

Figure 8.26 shows the seismic and elastic parameters obtained by using the joint Bayesian AVO and RMO inversion. The main observation is the improvement to the inverted Vs, which appears to catch the sudden increase causing the anomaly. In addition, both the Vp and density are also improved in the same interval.
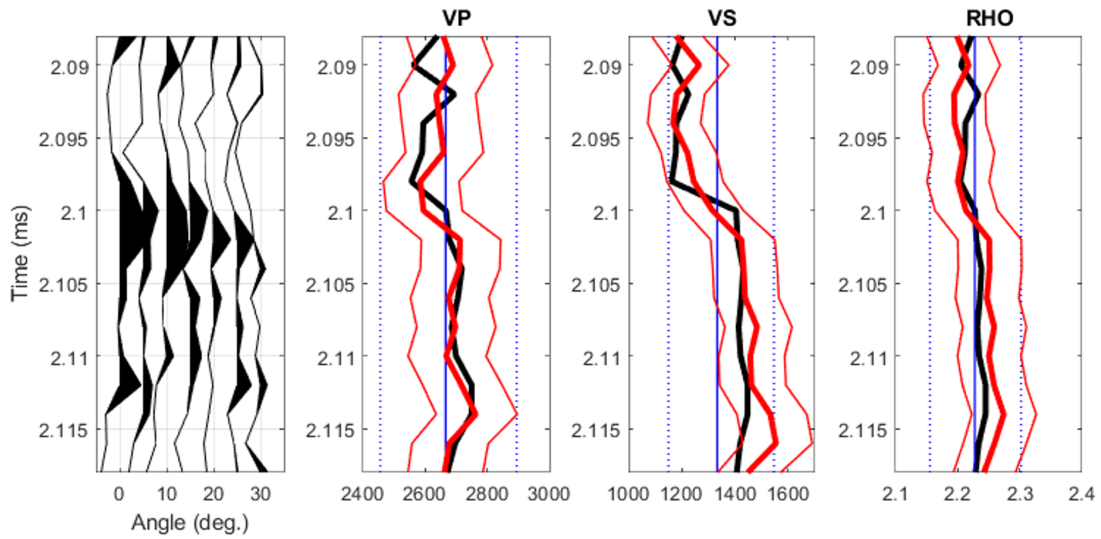
Figure 8.26: *Left: Model 2 white Gaussian noise gather after joint Bayesian AVO and RMO inversion. Black line: True elastic parameters. Thick red line: Optimal inverted parameters. Thin red line: 90% confidence interval. Thick blue line: Mean prior value. Thin dotted blue line: 90% confidence interval prior.*

8.4 Discussion

A Bayesian framework to invert for elastic parameters and RMO was implemented and tested. In addition, to see the difference to the elastic parameters done by also inverting for RMO, the gathers containing RMO were inverted for only the elastic parameters. It shows good results on both the model following the background trend, and the Class 2p anomaly. The algorithm converges quickly, especially for the noise-free seismic, where the optimal answer was obtained after two iterations. For noisy seismic, more iterations were required, due to the small steps taken few iterations prior to converging. This clearly indicates the iteration process was altered by noise.

The elastic parameters were greatly improved when the seismic was corrected for RMO. Especially for Model 2, where the inverted Vs went from wobbling around the prior, to catching the trend causing the anomaly. Improvements to Model 1 were also observed. In fact, when the RMO was removed, the inverted parameters almost completely overlapped with the true. It is important to note that the elastic parameters appeared to be decently inverted in the presence of RMO too. However, this is likely due to the prior resembling the true so well.

Generally, a Bayesian approach requires the formulation of prior knowledge. In this setting it might be considered a strength, because it helps constrain the inversion which is necessary considering the ill-posed problem of seismic inversion. In addition, acquiring prior information is easily solved by acquiring well log-data, and using general geology-based information generally known about the area of inter-

est *a priori.* Nonetheless, the prior knowledge often depends on the user, which in return can make the difference in results quite noticeable. In this chapter two examples of standard prior models for the elastic parameters were used, one of which was following an increasing trend and another that was the mean value over the whole section. When working with noise-free synthetic data one can often define a very vague prior and let the seismic do the work. However, using a vague prior to randomly draw initial values from contradicts the nature of Newton's method, which is dependent on a good initial guess to not get trapped in a local minimum. Keep in mind that this was only done to examine the importance of an initial guess. For Model 1 the need of a decent initial guess was not so important. Even when the algorithm drew two random values far from the solution, it still managed to obtain a decent answer in few iterations. Especially for the noise-free data. For Model 2 the case was different, especially in the presence of noise. If the initial values were two very poor values, it failed to iterate towards the answer. However, this can be easily solved by using a proper initial guess at each run. A natural initial guess would be to just assume zero residual move-out. That way the user also ensures the algorithm is not trapped in a poor local minimum.

8.5   AVO Analysis

As seen by the inverted elastic parameters, the AVO response was greatly improved by the method. To further investigating the changes done to the AVO response, the intercept and gradient traces were examined for both models. For Model 1, background trend, the coordinate system was also rotated to acquire the fluid cube. As Model 2 contains only the anomaly, the purpose of rotating the coordinate system to highlight one feature while minimizing another is lost.

Model 1: Background trend

Figure 8.27 shows the intercept and gradients plotted before and after inversion, both with and without noise (left and right respectively). The red points represent the response after RMO was applied, the blue points represent after inversion, while the green points show the true AVO response. In the noise-free case the intercept and gradient points post-inversion are completely overlapping with the true AVO response, which explains why they are not visible. The spread is dramatically reduced, and the inclination is exactly as it should be. This improvement in inclination suggest the vp/vs ratio post-inversion is exactly the same as the true ratio. The reduction in spread means the gradient will have the correct amplitudes too. When the noise is present the improvement is not as clear, but it is present. The spread is slightly reduced, and the inclination of the trend the green and blue points follow are different from the one followed by the red points. However, the differences in the presence of noise are harder to see.
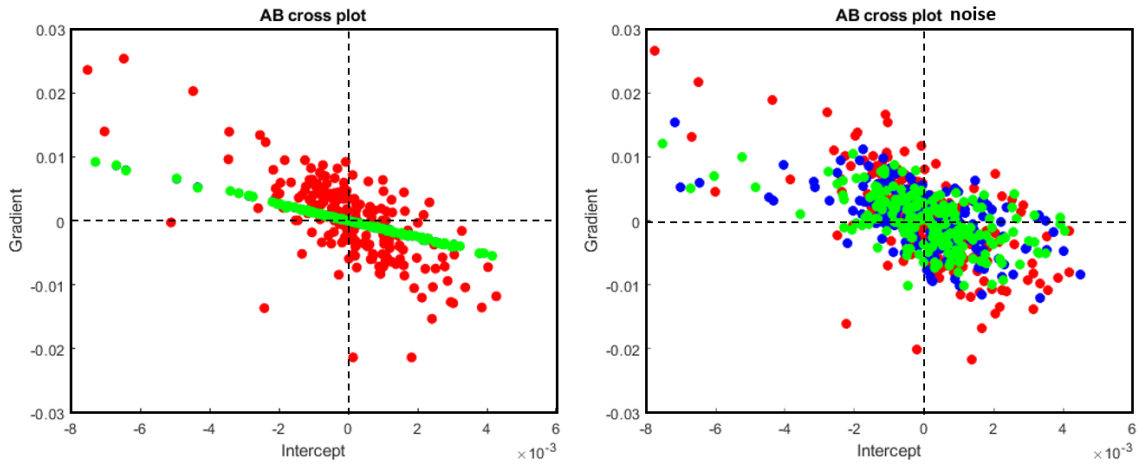
Figure 8.27: *Model 1 intercept and gradient cross plot. Green: true response. Blue: response after inversion. Red: response with RMO. Left: noise-free. Right: white noise.*

Figure 8.28 shows the intercept traces pre- and post-inversion together with the true trace, for seismic with and without noise. The pre-inversion trace is the one obtained when RMO is present in the data. The first observation is that all the traces are very similar, which is expected as small move-out differences does not affect the intercept too much. There are slight amplitude differences, but hardly noticeable.

Figure 8.28: *Model 1 intercept traces. True: original seismic. Pre: after adding RMO. Post: after inversion. Three to the left: noise free. Three to the right: white noise.*

The gradient traces are shown in Figure 8.29. The true gradient is identical to the gradient after inversion for the noise-free seismic. The gradient when RMO is present experiences way too large amplitudes. This large amplitude difference is related to the difference in the spread in the cross plot. There is also a clear improvement in

the presence of noise. When the RMO is added, the gradient experiences too large amplitudes. However after inversion, the corrected seismic has reduced amplitudes. This is further evidence the spread in the cross-plot was slightly reduced for the noisy seismic, even if it was hard to see.
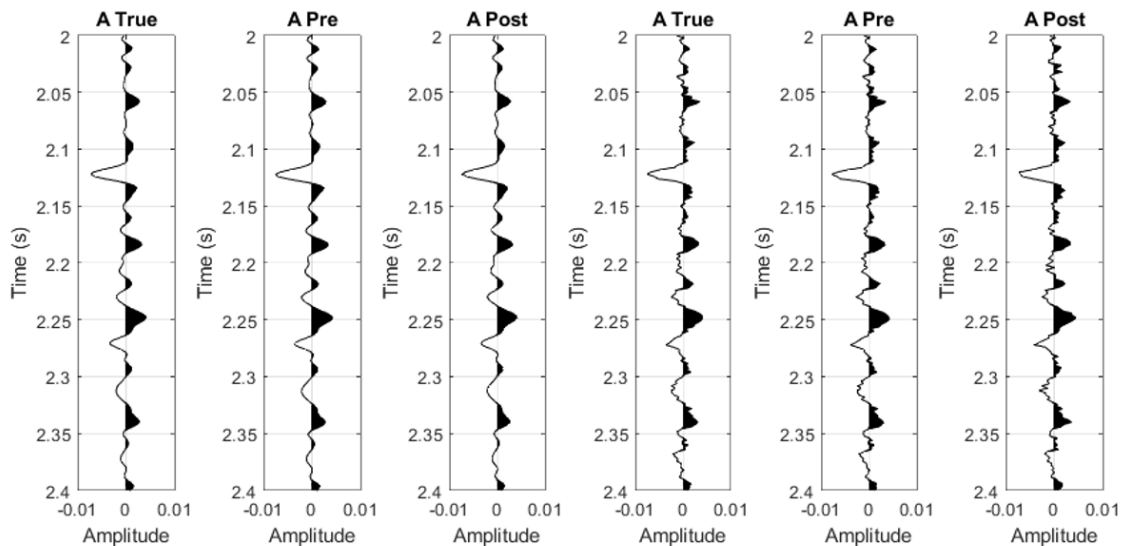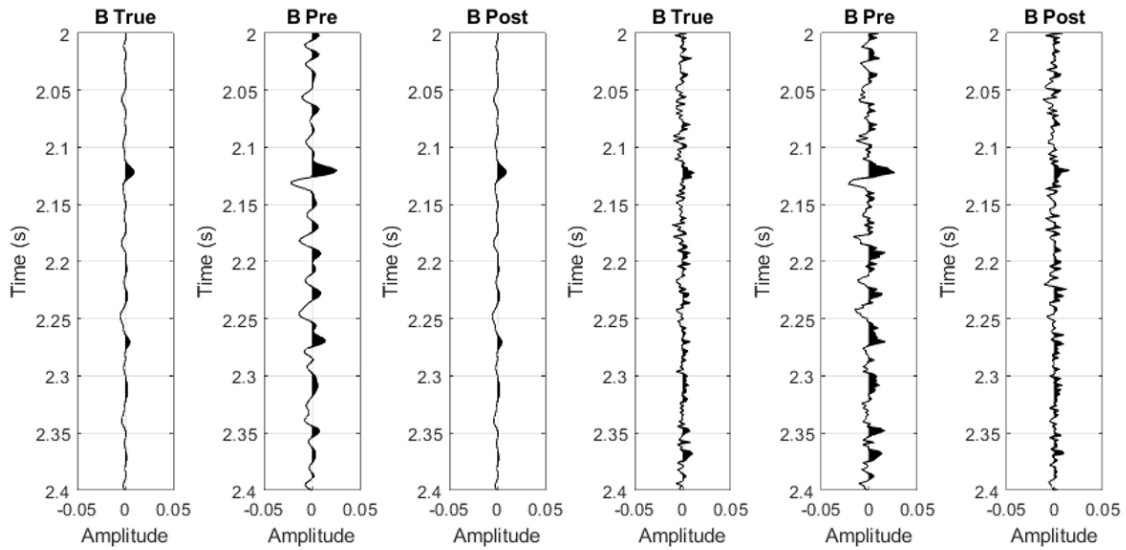

Figure 8.29: *Model 1 gradient traces. True: original seismic. Pre: after adding RMO. Post: after inversion. Three to the left: noise free. Three to the right: white noise.*

In addition, the coordinate system was rotated to see the improvement in the fluid traces pre- and post-inversion as seen in Figure 8.30. The true fluid trace is identical to the fluid trace after inversion for the noise-free model, as the RMO was completely removed for this model. The fluid trace when RMO is present experiences very large amplitudes, and resembles the true gradient trace. The fact that the fluid trace after inversion is zero indicates the inclination was properly corrected. The case is the same in the presence of noise too. The amplitudes when RMO is present are larger than the ones after inversion. This is a further indication the inclination was improved.
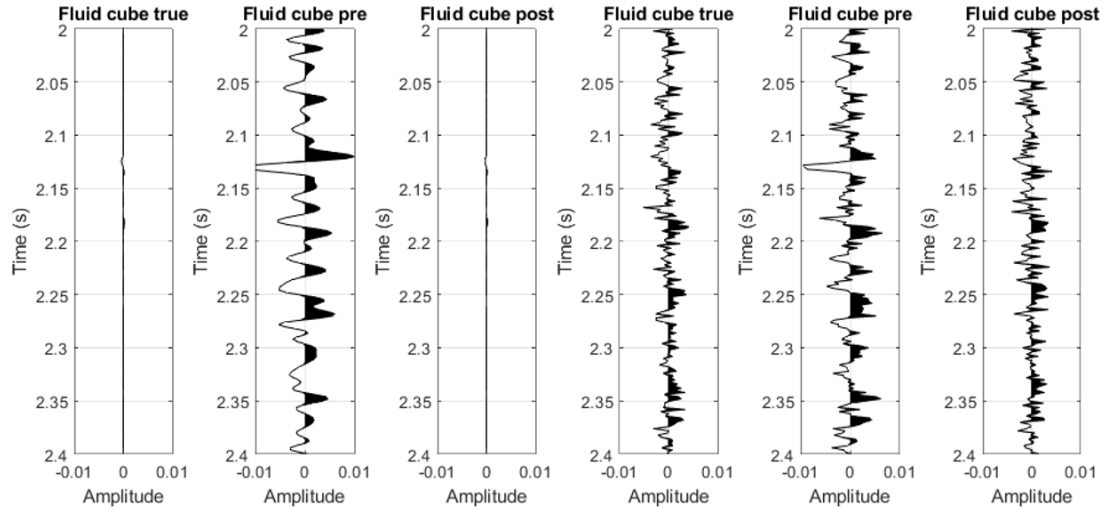
93

Figure 8.30: *Model 1 fluid traces. True: original seismic. Pre: after adding RMO. Post: after inversion. Three to the left: noise free. Three to the right: white noise.*

Model 2: Class 2p anomaly

Figure 8.31 shows the AVO response for the model containing the Class 2p anomaly. The red points represent the response after RMO was added. Green and blue represent the true and post-inversion responses respectively. The noise-free case shows clear improvement, as the AVO response after inversion is nearly completely overlapping with the true response. The points when RMO is added appear to follow a more linear line than the true and post-inversion points. For the noisy seismic, it is difficult to make much of the difference just by looking at the cross-plot. Similarly to the noise-free response, the red points appear to follow a linear line.
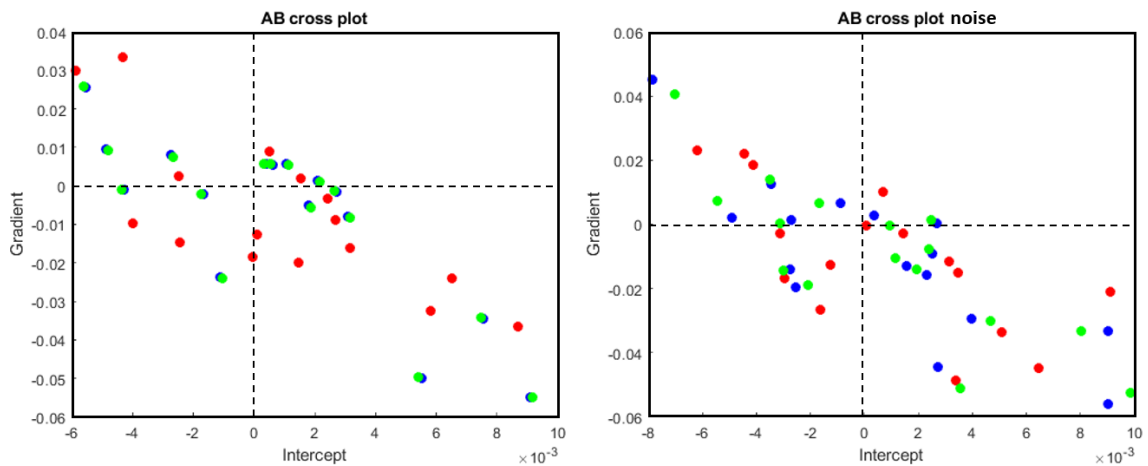

Figure 8.31: *Model 2 intercept and gradient cross plot. Green: True AVO response. Blue: response after inversion. Red: response with RMO. Left: noise free. Right: white noise.*

Figure 8.32 shows all the intercept traces, which are all near-identical as the small

94

move-out applied to the gather is not affecting the intercept much at all.

Figure 8.32: *Model 2 intercept traces. True: original seismic. Pre: after adding RMO. Post: after inversion. Three to the left: noise free. Three to the right: white noise.*

Figure 8.33 show all the gradient traces, and there is clear difference between them. The true and post-inversion gradient traces show positive amplitudes at $t = 2.09$ s, while the gradient trace with the presence of RMO shows negative. It appears that flattening the gather with the move-out applied has drastically changed the gradient at that time. The rest of the trace also show clear difference between pre and post, but these are amplitude related. The case is exactly the same for the noisy gather, which experiences the same change in sign and same amplitude artifacts.
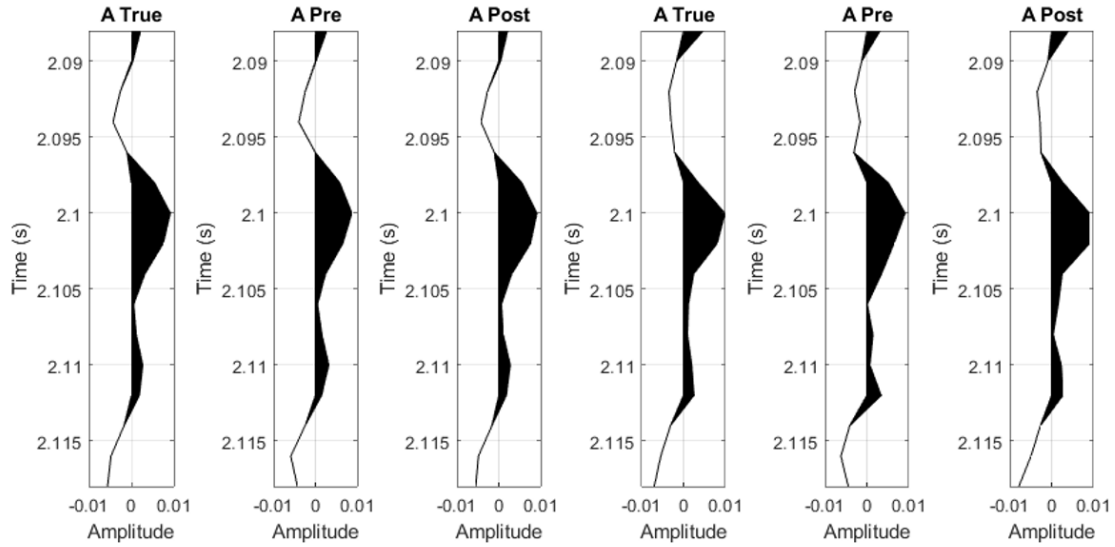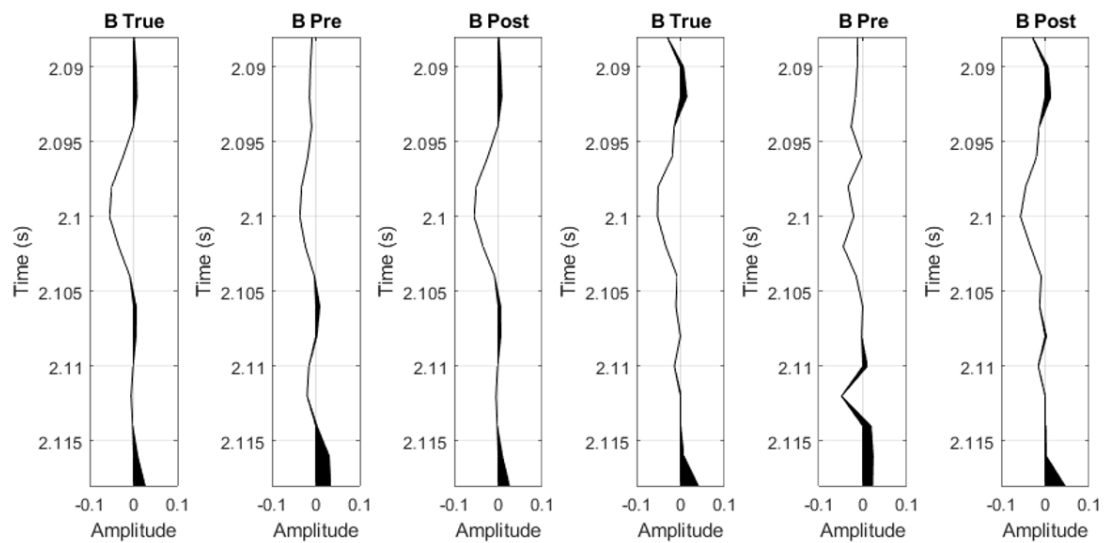

Figure 8.33: *Model 2 gradient traces. True: original seismic. Pre: after adding RMO. Post: after inversion. Three to the left: noise free. Three to the right: white noise.*

8.5.1 Summary

The intercept and gradient were examined for both models. When adding RMO, the amplitudes were greatly increased. However, this increase was removed after inversion. The difference was not as noticeable by looking at the cross plot for the noisy seismic, however the traces showed clear difference. The fact that the amplitudes on the gradient were corrected suggest the spread was reduced, and the amplitude reduction in the fluid trace post-inversion suggests the inclination was corrected too.

Chapter 9

Comparison and discussion

Four approaches were implemented and tested as methods to precondition data for seismic analysis. This chapter will compare the strengths and weaknesses of the methods, and examine the differences in the AVO responses post-correction.

9.1   Methods

As Semblance and Swans RVI both are directly related to velocity, it is natural to compare the two. The differences observed are related to the sensitivity of the methods, and the nature of the output. For Model 1, the normalized stacking amplitude was not maximized for the true trajectory neither when noise was nor was not present. In fact, when noise was present, there were 3-4 trajectories resulting in higher amplitudes. For Swan the case was different, for the noise-free seismic the RVI was clearly minimized for the right trajectory, while in the presence of noise it was minimized for a trajectory with minimum error. Swans RVI is clearly more sensitive to small changes in velocity. The second difference is related to the nature of the output. The normalized stacking amplitude provides no information whether the user is over- or under-correcting the seismic. On the other hand, the trace representing the RVI experiences a phase change depending on whether the user over- or under-corrects the seismic. In other words, Semblance is unimodal, while the RVI is bimodal. It is important to note that even though they are both directly related to velocity, they have different purposes. As mentioned, Semblance is used to maximize the stack energy. Swans approach was developed to precondition data for AVO analysis, where enhanced sensitivity is required. Other differences between the two methods are related to the derivative. The derivative of the RVI with respect to velocity is nonzero at the optimal velocity, while for Semblance it vanishes (Swan (2001)).

Cross correlation proves to be very useful too. It was by far the easiest method to implement and provides decent results with and without noise. Compared to the

other methods it had the lowest accuracy. However, this is directly due to my sub-optimal implementation where RMO below the sampling rate was neglected. This could easily be fixed by either re-sampling the data, or simply interpolating between two samples to obtain the correct values. All in all, cross correlation, Semblance and Swans RVI are very useful for non-anomalous seismic. For Model 2, they all completely failed to handle the apparent RMO correctly.

The joint Bayesian AVO and RMO inversion worked just as well as any other method on Model 1, if not better. The main difference is that it also successfully managed to correct the seismic for the model containing the anomaly. This means that the purpose of implementing a method were anomalies should not be avoided was successful. However, a proper initial guess is important. It is also important to note that even though it follows the Bayesian approach, it is an optimization algorithm that does not provide the user with any uncertainty information about a and b in $\Delta t = a\theta^2 + b\theta^2$. As mentioned, the user only obtains the maximum posterior solution. In order to acquire a complete posterior distribution, a Markov-Chain Monte Carlo simulation was also implemented. However, the lack of time resulted in not being able to properly present it.

An important note is the re-writing of the methods from static to dynamic approaches, which would be a much more realistic approach. As mentioned, RMO tends to be slowly varying across time in addition to offset. It is not unusual for a trace to experience negative RMO some places, and positive elsewhere. In order to correct the traces more accurately, stretching and squeezing has to be implemented. A widely used method is a time-varying approach to cross correlation, where the cross correlation is calculated at each time sample to obtain weighted time shifts. These can be smoothed across time and space, and the data can be interpolated accordingly. Swans RVI can be averaged across windows, meaning the user can correct for different amounts of move-out in each window. For Semblance, several trajectories are needed, and these can be combined with stretching and squeezing the seismic to obtain the best fit (Rickett & Lumley (2001), Wolberg (1990)). Regarding the joint Bayesian AVO and RMO inversion, $\Delta t(\theta)$ could be rewritten to $\Delta t(t, \theta)$, by including terms to ensure a slowly varying curve in both time and space.

9.1.1 Further work

An obvious improvement would be to re-write the optimization algorithm to a joint ζ and $\mathbf{m}$ optimization which would increase the accuracy and decrease the computational cost.

The method can also be improved by extending the term for ζ to more variables, making Δt a function of both time and angle. In other words, implement a dynamic approach to correcting for the residual move-out rather than a static one. This should improve the stability of each iteration.

In addition, the algorithm can be further improved by estimating the noise in the seismic instead of assuming constant noise, by using the inverse gamma distribution for the unknown standard deviation for the noise.

Finally, the method should also be tested on real data.

9.2 AVO Analysis

AVO analysis was performed by cross plotting the intercept and gradient for both models. To examine the difference done to the AVO response by the different methods, the residuals for intercept and gradient were calculated by subtracting the true and post-correction results. This has only been done for the noise-free synthetic gathers to truly capture the difference done by correcting the RMO by the different methods, and not any noise-related distortions.

Figure 9.1 shows the intercept residuals for all four methods used on Model 1. Keep in mind that the amplitude axis contains very small values. Nonetheless, there is quite the difference in the residuals. Swans RVI is the only method which perfectly corrected the seismic, resulting in zero residuals. Semblances lack of sensitivity resulted in small residuals. The Bayesian framework has the second lowest residuals, but they are as close to zero as can be. The main observation lies within cross correlation, where the residuals are large simply due to my implementation.
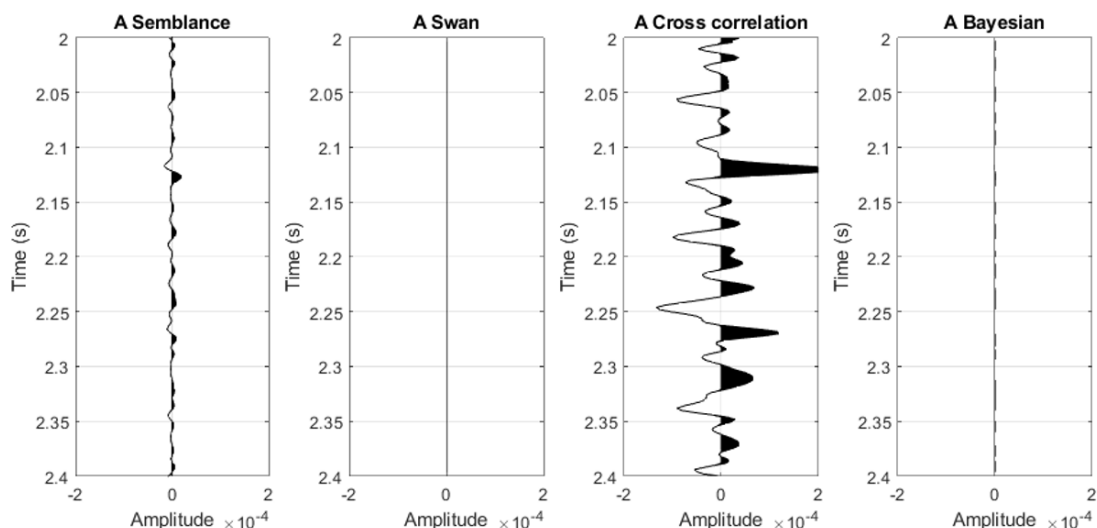

Figure 9.1: *Noise-free Model 1: intercept residuals (true minus after correction) for all methods.*

Figure 9.2 shows the same scenario, but for the gradient. Again, keep in mind the x-axis, the amplitudes are far lager than for the intercept. As the implementation of cross correlation did not allow for sub-sample RMO correction, this method experiences by far the largest gradient residual amplitudes. Swan and Bayesian obtain

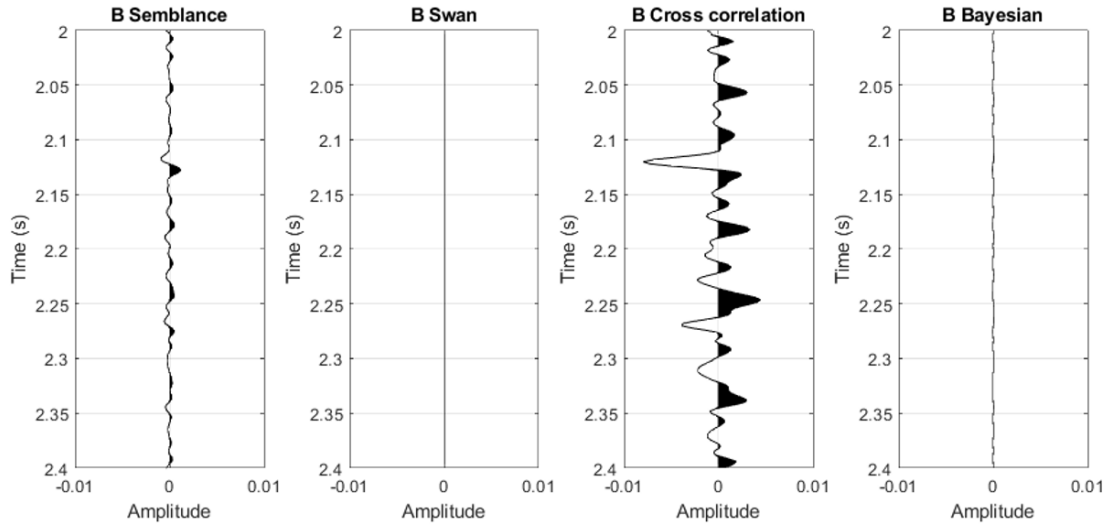zero and near-zero differences respectively, while Semblances lack of sensitivity fails to remove it all.

Figure 9.2: *Noise-free Model 1: gradient residuals (true minus after correction) for all methods.*

Figure 9.3 shows the residuals for the intercept for Model 2. The absolute value of the amplitudes are small, however the relative differences are huge. An important observation is the general shape of the traces. The residuals for Model 1 all shared the same shape, but experienced different amplitudes. For Model 2, there are clear differences in general shape and amplitudes. The residuals from the Bayesian framework are near-zero compared to the other methods. The changes in the shape between the other methods indicates they all reacted differently to apparent RMO. At approximately $t = 2.095\,\mathrm{s}$ the residuals are negative for Semblance, but positive for cross correlation and Swan. The residuals obtained post-cross correlation are the second smallest, and do resemble the ones post-semblance. This indicates they did a fairly similar job, which resulted in flattening the gather. The reason the residuals post-Swan is so different is because of the way the method handled apparent RMO. As shown in Chapter 6, the RVI was minimized for values of a and b that corrected the gather into a co-linear relationship between intercept and gradient. The resulting seismic was quite different from that of Semblance and cross correlation.
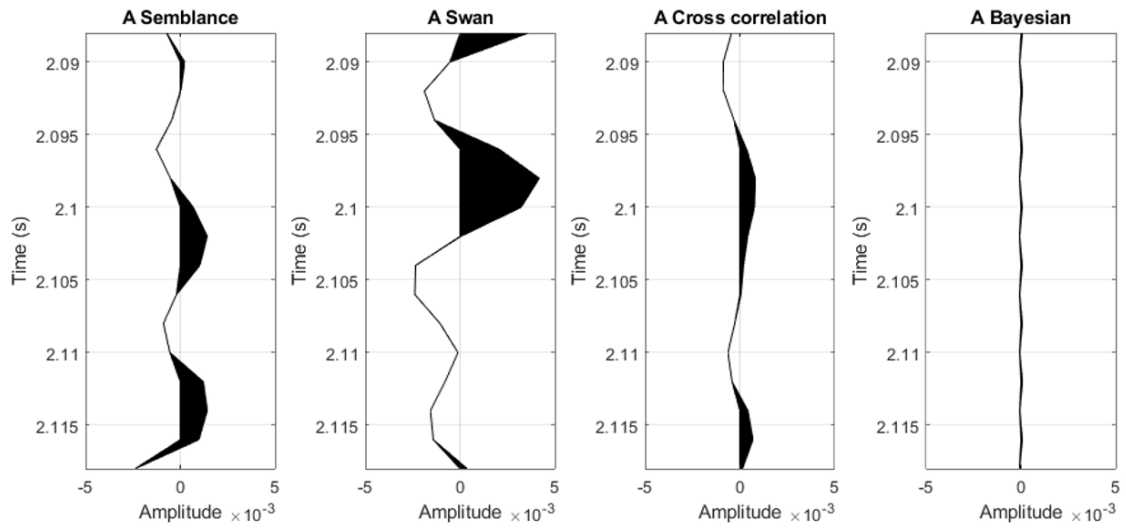
Figure 9.3: *Noise-free Model 2: Intercept residuals (true minus after correction) for all methods.*

Figure 9.4 shows the gradient residuals for model 2. The Bayesian framework did an excellent job correcting for the RMO, resulting in near-zero residuals compared to the other methods. Generally, the changes are related to general shape and amplitude. Residuals post-Semblance and cross correlation are fairly similar with small amplitude differences, while the post-Swan response is different in every way. Again, this is related to the nature of the output seismic. Simply put, Swan moved the seismic down while cross correlation and Semblance moved it up.
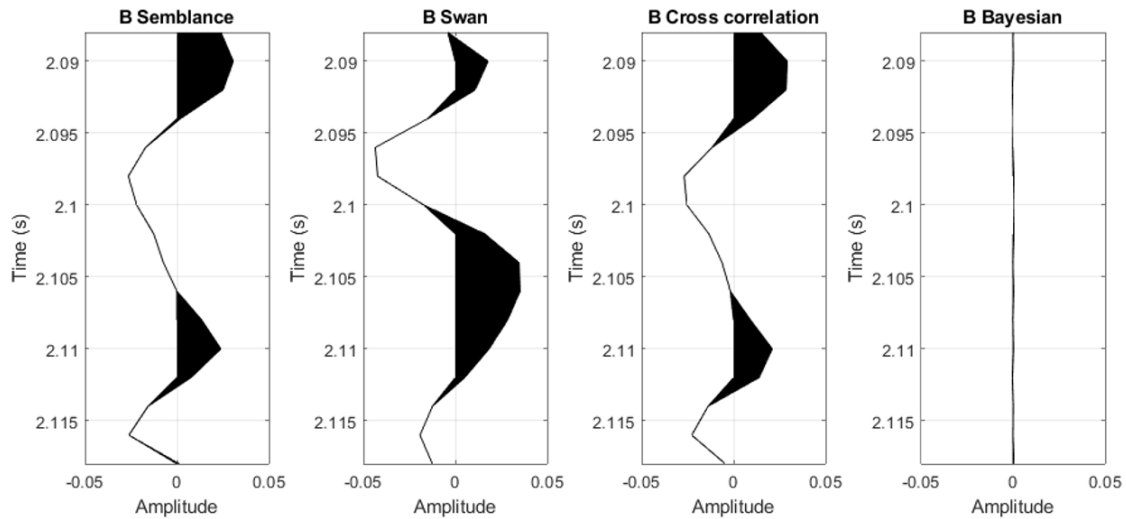
Figure 9.4: *Noise-free Model 2: Gradient residuals (true minus after correction) for all methods.*

Another important observation was made when comparing the chi angles in which resulted in the fluid traces. For Swan, Semblance and Bayesian it was approximately the same (≈ 35 degrees). However, for cross correlation it was 62 degrees, which is a significant increase. This is related to only using the near and far when estimating

the AVO response, which resulted in intercept and gradient points following a very flat trend.

Chapter 10

Conclusion

The main purpose of this thesis was to test existing methods to correct for RMO, and compare them with the new method introduced in Chapter 8. The reason behind the need for correction is to make AVO more robust. The existing methods were cross correlation, Semblance, and Swans RVI. For the model following the background trend they all proved to be very useful, clearly improving the intercept and gradient, which further resulted in the right chi angle to obtain the fluid trace. The main differences between the output of the different methods are generally linked to implementation and sensitivity to small move-out errors. Cross correlation provided un-accurate results due to the implementation neglecting sub-sample RMO. Semblance lacked the sensitivity needed to remove all the RMO, while Swans RVI managed to do so. The new method proposed has the sensitivity needed, in addition to providing inverted elastic parameters with uncertainty in the same time.

For the model containing the anomaly, the difference between the results provided by the existing and the new method were clearly different. Semblance, cross correlation and Swans RVI acted in ways that very clearly altered the gather in the wrong way. This resulted in distorting the intercept and gradient almost to the point of no recognition. Some time-samples even went from positive to negative amplitudes. This clearly suggests the user should avoid known anomalies when using these methods. The joint Bayesian AVO and RMO inversion however, did an outstanding job at correcting for RMO in the presence of an anomaly, given a proper initial guess. The main idea behind this new framework was to develop a method to correct for RMO where the user is not suggested to avoid or neglect anomalies. Keep in mind that they are in fact what we actively look for in oil exploration.

References

Aki, K., & Richards, P. (1980). Quantitive seismology: Theory and methods. 1a. ed. San Francisco (EEUU): Freeman and Company, 1, 557.

Avseth, P., Dvorkin, J., Mavko, G., & Rykkje, J. (2000). Rock physics diagnostic of north sea sands: Link between microstructure and seismic properties. Geophysical Research Letters, 27(17), 2761–2764.

Buland, A., & Omre, H. (2003). Bayesian linearized avo inversion. Geophysics, 68(1), 185–198.

Castagna, J. P., Batzle, M. L., & Eastwood, R. L. (1985). Relationships between compressional-wave and shear-wave velocities in clastic silicate rocks. Geophysics, 50(4), 571–581.

Downton, J. E. (2005). Seismic parameter estimation from avo inversion. University of Calgary, Department of Geology and Geophysics.

Dunkin, J., & Levin, F. (1973). Effect of normal moveout on a seismic pulse. Geophysics, 38(4), 635–642.

Faccipieri, J. H., Coimbra, T. A., & Bloot, R. (2019). Stretch-free generalized normal moveout correction. Geophysical Prospecting, 67(1), 52–68.

Fatti, J. L., Smith, G. C., Vail, P. J., Strauss, P. J., & Levitt, P. R. (1994). Detection of gas in sandstone reservoirs using avo analysis: A 3-d seismic case history using the geostack technique. Geophysics, 59(9), 1362–1376.

Foster, D., Smith, S., Dey-Sarkar, S., & Swan, H. (1993). A closer look at hydrocarbon indicators. In Seg technical program expanded abstracts 1993 (pp. 731–733). Society of Exploration Geophysicists.

Gardner, G., Gardner, L., & Gregory, A. (1974). Formation velocity and density—the diagnostic basics for stratigraphic traps. Geophysics, 39(6), 770–780.

Landrø, M. (2001). Discrimination between pressure and fluid saturation changes from time-lapse seismic data. Geophysics, 66(3), 836–844.

Li, J., & Symes, W. W. (2007). Interval velocity estimation via nmo-based differential semblance. Geophysics, 72(6), U75–U88.

Neidell, N. S., & Taner, M. T. (1971). Semblance and other coherency measures for multichannel data. Geophysics, 36(3), 482–497.

Ostrander, W. (1984). Plane-wave reflection coefficients for gas sands at nonnormal angles of incidence. Geophysics, 49(10), 1637–1648.

Perroud, H., & Tygel, M. (2004). Nonstretch nmo. Geophysics, 69(2), 599–607.

Ratcliffe, A., & Roberts, G. (2003). Robust, automatic, continuous velocity analysis. In Seg technical program expanded abstracts 2003 (pp. 2080–2083). Society of Exploration Geophysicists.

Rickett, J., & Lumley, D. (2001). Cross-equalization data processing for time-lapse seismic reservoir monitoring: A case study from the gulf of mexico. Geophysics, 66(4), 1015–1025.

Rupert, G., & Chun, J. (1975). The block move sum normal moveout correction. Geophysics, 40(1), 17–24.

Rutherford, S. R., & Williams, R. H. (1989). Amplitude-versus-offset variations in gas sands. Geophysics, 54(6), 680–688.

Sheriff, R. E., & Geldart, L. P. (1995). Exploration seismology. Cambridge university press.

Shuey, R. (1985). A simplification of the zoeppritz equations. Geophysics, 50(4), 609–614.

Smith, G., & Gidlow, P. (1987). Weighted stacking for rock property estimation and detection of gas. Geophysical Prospecting, 35(9), 993–1014.

Spagnolini, U. (1994). Compound events decomposition and the interaction between avo and velocity information 1. Geophysical prospecting, 42(3), 241–259.

Spratt, S. (1987). Effect of normal moveout errors on amplitude versus offset-derived shear reflectivity. In Seg technical program expanded abstracts 1987 (pp. 634–637). Society of Exploration Geophysicists.

Swan, H. W. (2001). Velocities from amplitude variations with offset. Geophysics, 66(6), 1735–1743.

Walden, A. (1991). Making avo sections more robust 1. Geophysical Prospecting, 39(7), 915–942.

Wolberg, G. (1990). Digital image warping (Vol. 10662). IEEE computer society press Los Alamitos, CA.

Yilmaz, Ö. (2001). Seismic data analysis: Processing, inversion, and interpretation of seismic data. Society of exploration geophysicists.